Investigation of Non-Covalent Interactions in the Solid-State and in Solution Phase

by

Taylor A. Bramlett

A dissertation submitted in partial fulfillment
of the requirements for the degree of
Doctor of Philosophy
(Chemistry)
in the University of Michigan
2022

Doctoral Committee:

Professor Adam J. Matzger, Chair
Professor Anne J. McNeil
Professor Corinna Schindler
Professor Veera Sundararaghavan

Taylor A. Bramlett

tabram@umich.edu

ORCID iD: 0000-0002-7964-2211

© Taylor A. Bramlett 2022

Dedication

To the Bramlett, Bulloch, Wells, and Gibbs Families

To Marcus and Madison

Acknowledgements

First, I want to give thanks to my Lord and Savior Jesus Christ who is the head of my life for without him I would not be here today. I give thanks to my mom, Pamela Bramlett who has continuously loved, supported, and encouraged me throughout this journey. I give flowers on this side of the river Jordan to my brother-from-another-mother, Monquez Ford, whose presence in my life has helped me to weather the storms and rains. I also give flowers to my dearests Gabrielle Anderson and Antonia Jetts, both of whom have given me great solace during a time of sorrow. I am thankful for the support I have received from my family as a whole, but a special shoutout to my extended family members, my great aunt and uncle Barbara Gibbs and Nathaniel Gibbs. They welcomed me into their family (much love to my brothers/cousins Brandon and Tedric Gibbs). They gave me a safe haven that felt just like home (Memphis, TN) and they showed me what it is like to love unconditionally. I give special thanks to Dr. Rosalyn Kent, Dr. Wesley Pein, Dr. Angelar Muthike, Dr. James Collins III, Dr. Michael Bellas, Maribel Okiye, Yves Nazon II, Phoenix Williams, Alex Franklin, and Elizabeth Michalski for extending kindness, friendship, and support to me. I thank my research advisor Professor Adam Matzger for his guidance and support during my time as a Matzger lab member. He has offered a great deal of encouragement during times where I was giving up on myself which motivated me to persevere. I would also like to thank my committee members, Professor Corinna Schindler, Professor Anne McNeil, and Professor Veera Sundararaghavan, for their support throughout my graduate career. I would like to give a

big shout out to the Matzger lab members because they have made these last few years memorable. I am truly grateful for every experience we have shared together!

Table of Contents

Dedication ii

Acknowledgements iii

List of Tables viii

List of Figures xi

Abstract xv

Chapter 1 Introduction 18

1.1 Non-covalent Interactions 18

1.2 Predictions of Supramolecular Assemblies 21

1.3 Cocrystallization in Energetic and Non-Energetic Materials 23

1.4 Outline of Thesis 28

1.5 References 29

Chapter 2 Leveraging Existing Structural Data for the Discovery of Novel Hydrogen Peroxide Solvates 35

2.1 Introduction 35

2.2 Results and Discussion 38

2.3 Conclusion 48

2.4 Methods 49

2.4.1 Materials and Reagents 49

2.4.2 General Methods: Peroxosolvate Crystallization of Compounds (1-8) 50

2.4.3 Raman Spectroscopy 50

2.4.4 ^{31}P NMR 50

2.4.5 Single-Crystal X-ray Diffraction (SC-XRD) 51
2.4.6 Powder X-ray Diffraction (PXRD) 51
2.4.7 Experimental Setup 52
2.5 Additional Figures 52
2.6 Additional Tables 68
2.7 References 72
Chapter 3 Halogen Bonding Propensity in Solution: Direct Observation and Computational Prediction 76
3.1 Introduction 76
3.2 Results and Discussion 79
3.2.1 Electronic effects on XB strength 79
3.2.2 Observation of halogen bonding in solution 89
3.3 Conclusion 95
3.4 Methods 96
3.4.1 Experimental Setup 96
3.4.2 Computations 97
3.5 Additional Tables 98
3.6 References 106
Chapter 4 Synthesis and Characterization of Strongly Polarized Haloarenes for Multicomponent Crystal Design 110
4.1 Introduction 110
4.2 Results and Discussion 114
4.2.1 ESP predictions 114
4.2.2 Synthesis of IPNB 116
4.2.3 Cocrystallization of IPNB 124
4.2.4 Halogen bonding in solution for IPNB 126

4.3 Conclusion....128
4.4 Methods....128
4.4.1 Materials and Reagents....128
4.4.2 General Methods: Reaction Conditions for IPNB Synthesis....129
4.4.3 General Methods: Cocrystallization Conditions for IPNB Complexes....131
4.4.4 Raman Spectroscopy....131
4.4.5 Fourier Transform Infrared Spectroscopy (FT-IR)....132
4.4.6 Single-Crystal X-ray Diffraction (SC-XRD)....132
4.4.7 Differential Scanning Calorimetry....133
4.4.8 Experimental Setup....133
4.4.9 Computations....133
4.5 Additional Figures....134
4.6 Additional Tables....137
4.7 References....141
Chapter 5 Conclusion....143
5.1 Summary of Work....143
5.2 References....146

List of Tables

Table 2.1. Crystallization conditions for compounds **1-8**.....40

Table 2.2. Major H_2O_2 (O-O) stretching vibrational frequency in cm^{-1} of each newly formed peroxosolvate and 98% H_2O_2. 41

Table 2.3. Hydrogen bond (HB) interaction distances (O···N or O···O-N) in the hydrate and peroxosolvate structures of compounds **4a-b**, **5**, and **7a-b**. 46

Table 2.4. Crystallographic data for peroxosolvates and previously published (relevant) hydrates of compound **2**. 68

Table 2.5. Crystallographic data for peroxosolvates and previously published (relevant) hydrates of compounds **4a** and **b**. 69

Table 2.6. Crystallographic data for peroxosolvates and previously published (relevant) hydrates of compound **5**. 70

Table 2.7. Crystallographic data for peroxosolvates and previously published (relevant) hydrates of compounds **7a** and **b**. 71

Table 3.1. Electrostatic potential values for the XB donors and acceptors in kcal mol^{-1} calculated at B3LYP/6-311G** level. 80

Table 3.2. ΔV_s values of all 20-halogen bond donor/acceptor complexes in kcal mol^{-1} calculated at B3LYP/6-311G** level. 81

Table 3.3. Listing of total energies (hartrees) for all XB bond donors, acceptors, and complexes at B3LYP/6-311G** level of theory using Spartan '16. 82

Table 3.4. Theoretical binding energies (ΔE_{bind}) of all XB donor/acceptor complexes in kcal mol^{-1} calculated at B3LYP/6-311G** level. 83

Table 3.5. Calculated theoretical binding energies (ΔE_{bind}) of all XB donor/acceptor complexes (kcal mol^{-1}) at B3LYP-D3/6-311G** level of theory using Spartan '18. 85

Table 3.6. Calculated C-I bond lengths (Å) for all XB donors and donor/acceptor complexes with interaction distances (Å) and bond angles (°) at B3LYP and B3LYP-D3/6-311G** level of theory using Spartan '16 and '18. 85

Table 3.7. Calculated theoretical binding energies (ΔE_{bind}) for the solvent model (DCM) of all the XB donor/acceptor complexes (kcal mol^{-1}) at B3LYP/6-311G** level of theory using Spartan '18. 86

Table 3.8. Deconvoluted frozen (FRZ) term ($\Delta E_{FRZ} = (\Delta E_{ELEC} + \Delta E_{PAULI}) + \Delta E_{DISP}$) in kcal mol^{-1} as dispersion (DISP), electrostatics (ELEC), and Pauli repulsion (PAULI) energies in ALMO-EDA for IPFB/acceptor complexes and IDNB/acceptor complexes. 88

Table 3.9. Summary of interaction energies ($\Delta E = \Delta E_{FRZ} + \Delta E_{POL} + \Delta E_{CT}$) in kcal mol^{-1} deconvoluted into 3 energy terms (frozen (FRZ), polarization (POL), and charge transfer (CT)) in ALMO-EDA from Q-Chem 5.3.2 for IPFB/acceptor complexes and IDNB/acceptor complexes. 89

Table 3.10. C-I stretching vibrational frequency (ν) in cm^{-1} of each unbound XB donor and each complex observed in CH_2Cl_2. 90

Table 3.11. ΔG values (kcal mol^{-1}) of observed XB donor/acceptor complexes were derived from the relative areas of the bound and unbound donors to determine relative concentration of bound and unbound states. These free energy values assume equal Raman scattering. 95

Table 3.12. Cartesian coordinates of the computed IPFB/3-NPy complex at the B3LYP/6-311G** level of theory in Q-Chem 5.3.2 for ALMO-EDA. 98

Table 3.13. Cartesian coordinates of the computed IPFB/3-FPy complex at the B3LYP/6-311G** level of theory in Q-Chem 5.3.2 for ALMO-EDA. 99

Table 3.14. Cartesian coordinates of the computed IPFB/3-PY complex at the B3LYP/6-311G** level of theory in Q-Chem 5.3.2 for ALMO-EDA. 100

Table 3.15. Cartesian coordinates of the computed IPFB/DMAP complex at the B3LYP/6-311G** level of theory in Q-Chem 5.3.2 for ALMO-EDA. 101

Table 3.16. Cartesian coordinates of the computed IDNB/3-NPy complex at the B3LYP/6-311G** level of theory in Q-Chem 5.3.2 for ALMO-EDA. 102

Table 3.17. Cartesian coordinates of the computed IDNB/3-FPy complex at the B3LYP/6-311G** level of theory in Q-Chem 5.3.2 for ALMO-EDA. 103

Table 3.18. Cartesian coordinates of the computed IDNB/PY complex at the B3LYP/6-311G** level of theory in Q-Chem 5.3.2 for ALMO-EDA. 104

Table 3.19. Cartesian coordinates of the computed IDNB/DMAP complex at the B3LYP/6-311G** level of theory in Q-Chem 5.3.2 for ALMO-EDA. 105

Table 4.1 ESP values for the XB donors ($V_{,max}$) and acceptors ($V_{s,min}$) in kcal mol^{-1} calculated at B3LYP/6-311G** level. 115

Table 4.2. ΔV_s values of halogen bond donor/acceptor complexes for TITNB and IPNB in kcal mol^{-1} calculated at B3LYP/6-311G** level. 116

Table 4.3 Crystallographic data for compounds **5**/4-PICO and DMAP.....126

Table 4.4. C-I stretching vibrational frequency (ν) in cm^{-1} of unbound IPNB and the complex observed with THF in DCE. 127

Table 4.5. Crystallographic data for pentanitroaniline (PNA).....137

Table 4.6. Crystallographic data for previously published and newly characterized hexanitrobenzene (HNB).....138

Table 4.7. Crystallographic data for previously published and newly characterized chloro-pentanitrobenzene (CPNB).....139

Table 4.8. Crystallographic data for newly characterized iodo-pentanitrobenzene (IPNB).....140

List of Figures

Figure 1.1. Simple representation of hydrogen and halogen bonding interactions.....18

Figure 1.2. Illustration of increasing polarizability based on the halogen atom.....19

Figure 1.3a-b. Traditional and non-traditional hydrogen bonding interactions. 20

Figure 1.4. Halogen bonding interactions with halogen atoms and arbitrary Lewis bases. 21

Figure 1.5. Electrostatic potential (ESP) maps that depict $V_{s,max}$, $V_{s,min}$, and ΔV_s calculations using the density functional method B3LYP/6-311G**. 22

Figure 1.6. Theoretical binding energy (ΔE_{bind}) calculated using the density functional method B3LYP/6-311G**. 22

Figure 1.7. Breakdown of the categories of energetic materials.....24

Figure 1.8. Illustration of the cocrystallization technique. 25

Figure 1.9. Chemical structures of TNT and CL-20. 26

Figure 1.10. CL-20/TNT cocrystal (IZUZUZ02). 26

Figure 2.1. Illustration of the CSD search geometry.....38

Figure 2.2. Structures of target compounds **1-8**.....39

Figure 2.3. Structures of compounds **4b** and **7b**. 40

Figure 2.4. Powder pattern of the hydrates of compound **8** (BPU-purple, green, and blue) and peroxosolvate **8** (black). 42

Figure 2.5. ^{31}P NMR spectra of hydrate/peroxosolvate mixture of compound **2** with triphenylphosphine oxidized to triphenylphosphine oxide, recorded at 25 °C. 43

Figure 2.6. Powder patterns of two hydrates of compound **2** (gold and green) and peroxosolvate **2** (black).....43

Figure 2.7. Histogram of the hydrogen bond interaction distances between water or H_2O_2 O to sp^2 N-pyridyl group or O-N (N-oxide) color coded as pyridyl hydrate (blue), pyridyl peroxosolvate (orange**)**, N-oxide hydrate (green), and N-oxide peroxosolvate (red). 45

Figure 2.8. Illustration of the interactions of water in the hydrate (pyridyl or **4a**-H_2O) and hydrogen peroxide in the peroxosolvate (**4a**-H_2O_2) of compound **4a.** 46

Figure 2.9. Illustration of the interactions that occur between both the pyridyl-group and sulfonyl-group with H_2O_2 in **5**-H_2O_2 (one conformer shown). 47

Figure 2.10. Illustration of the interactions of water in the hydrate (**7a**-H_2O, HUGMEB), hydrogen peroxide in the peroxosolvate (**7a**-H_2O_2, one conformer shown), and hydrogen peroxide in the N-oxide peroxosolvate (**7b**-H_2O_2) of compound **7a**. 48

Figure 2.11. Full range (100-2000 cm^{-1}). Stacked Raman spectra of compound **1** (TPTT-blue), 98% hydrogen peroxide (black), and peroxosolvate **1** (red). 52

Figure 2.12. Zoomed in, stacked Raman spectra (795-935 cm^{-1}) of compound **1** (TPTT-blue), 98% hydrogen peroxide (black), and peroxosolvate **1** (red). 53

Figure 2.13. Full range (100-1800 cm^{-1}). Stacked Raman spectra of compound **2** (dmpa-blue), 98% hydrogen peroxide (green), and peroxosolvate **2** (red). 54

Figure 2.14. Zoomed in, stacked Raman spectra (790-990 cm^{-1}) of compound **2** (dmpa-blue), 98% hydrogen peroxide (green), and peroxosolvate **2** (red). 55

Figure 2.15. Full range (100-2000 cm^{-1}). Stacked Raman spectra of compound **4a** (VDP-green), 98% hydrogen peroxide (purple), and peroxosolvate **4a** (red). 56

Figure 2.16. Zoomed in, stacked Raman spectra (750-1500 cm^{-1}) of compound **4a** (VDP-green), 98% hydrogen peroxide (black), and peroxosolvate **4a** (red). 57

Figure 2.17. Full range (100-1900 cm^{-1}). Stacked Raman spectra of compound **4a** (VDP-blue), 98% hydrogen peroxide (red), and peroxosolvate **4b** (green). 58

Figure 2.18. Zoomed in, stacked Raman spectra (790-930 cm^{-1}) of compound **4a** (VDP-blue), 98% hydrogen peroxide (red), and peroxosolvate **4b** (green). 59

Figure 2.19. Full range (100-1940 cm^{-1}). Stacked Raman spectra of compound **5** (ETORICOXIB-blue), 98% hydrogen peroxide (green), and peroxosolvate **5** (red). 60

Figure 2.20. Zoomed in, stacked Raman spectra (750-1200 cm^{-1}) of compound **5** (ETORICOXIB-blue), 98% hydrogen peroxide (green), and peroxosolvate **5** (red).....61

Figure 2.21. Full range (100-1760 cm^{-1}). Stacked Raman spectra of compound **7a** (TSAMP-blue), 98% hydrogen peroxide (black), and peroxosolvate **7a** (red).....62

Figure 2.22. Zoomed in, stacked Raman spectra (750-1040 cm^{-1}) of compound **7a** (TSAMP-blue), 98% hydrogen peroxide (black), and peroxosolvate **7a** (red).....63

Figure 2.23. Full range (100-2000 cm^{-1}). Stacked Raman spectra of compound **7a** (TSAMP-blue), 98% hydrogen peroxide (red), and peroxosolvate **7b** (green). 64

Figure 2.24. Zoomed in, stacked Raman spectra (750-920 cm^{-1}) of compound **7a** (TSAMP, blue), 98% hydrogen peroxide (red), and peroxosolvate **7b** (green). 65

Figure 2.25. Full range (100-2000 cm^{-1}). Stacked Raman spectra of compound **8** (BPU-blue), 98% hydrogen peroxide (green), and peroxosolvate **8** (red). 66

Figure 2.26. Zoomed in, stacked Raman spectra (720-960 cm^{-1}) of compound **8** (BPU-blue), 98% hydrogen peroxide (green), and peroxosolvate **8** (red). 67

Figure 3.1. Illustration of halogen bonding interactions between a halogenated compound and a Lewis base. 76

Figure 3.2. (**a**) 1-iodo-3,5-dinitrobenzene strucuture. (**b**) Electrostatic potential map of 1-iodo-3,5-dinitrobenzene with positive ($V_{s,max}$) to negative ($V_{s,min}$) regions (blue +55 to red -55 kcal mol^{-1}), respectively.....78

Figure 3.3. ESP maps of iodinated halogen bond donors and pyridine derived acceptors to visualize $V_{s,max}$ (blue) and $V_{s,min}$ (red) regions (kcal mol^{-1}) at the B3LPY/6-311G** level of theory.....79

Figure 3.4. Graph representing the correlation between theoretical ΔE_{bind} and XB acceptor strength ($V_{s,min}$, kcal mol^{-1}). 83

Figure 3.5. Graph representing the correlation between ΔE_{bind} and XB donor strengths ($V_{s,max}$, kcal mol^{-1}).....84

Figure 3.6. Graph representing the correlation between ΔE_{bind} and ΔV_s in kcal mol^{-1}. 87

Figure 3.7. Raman spectra of unbound DFIB and 2:3, 1:1, and 2:1 molar ratios of DFIB/DMAP solutions.....91

Figure 3.8a-c. Raman spectra of unbound IPFB and 2:3, 1:1, and 2:1 molar ratios of (**a**) IPFB/3-FPy solutions, (**b**) IPFB/PY, and (**c**) IPFB/DMAP solutions. 92

Figure 3.9. Raman spectra of unbound IDNB and 2:3, 1:1, and 2:1 molar ratios of IDNB/DMAP solutions.....93

Figure 3.10. Graph representing the correlation between observed red shifted ΔC-I stretch (cm^{-1}) and ΔE_{bind} (kcal mol^{-1}). The purple line represents the fit for observed IPFB/acceptor complexes. 94

Figure 3.11. Graph representing the correlation between C-I···N interaction distances (Å) and ΔE_{bind} (kcal mol^{-1}). 95

Figure 4.1. Illustration of halogen bonding interactions between chlorinated, brominated, and iodinated complexes (Cl-R, Br-R, and I-R, respectively) and a halogen bond acceptor denoted as Y.....111

Figure 4.2. Halogen and hydrogen bonding interactions within TITNB/TNB cocrystal.....112

Figure 4.3. ESP maps of TITNB and IPNB calculated at B3LYP/6-311G** level of theory Spartan '18 software along with their corresponding $V_{s,max}$ values.....113

Figure 4.4. Three TITNB coformers and their $V_{s,min}$ values in kcal mol^{-1} calculated at B3LYP/6-311G** level.....114

Figure 4.5. Four target XB acceptors. 115

Figure 4.6a-c. Optimized synthetic approach to access halopentanitrobenzene derivatives (chloro or iodo). (**a**) Nitration of 3,5-dinitroaniline to pentanitroaniline, (**b**) oxidation of pentanitroaniline to hexanitrobenzene, and (**c**) halogenation of hexanitrobenzene to halopentanitrobenzenes (X=Cl or I).....117

Figure 4.7. First reported non-solvated structure of PNA with intra-and intermolecular interactions.....118

Figure 4.8. Illustration of a HNB molecule with a view of the benzene ring that is perpendicular to the a- and c-axes. The sterically hindered nitro-groups are denoted as rotated around the C-N bonds. 120

Figure 4.9. Illustration of the similarities in the crystal structures of HNOBEN (blue) and compound **2** (colored by element) with cell axes shown. 121

Figure 4.10. Experimental structure of compound **4** (CPNB) from crystallography.....122

Figure 4.11. Experimental structure of compound **5** (IPNB) from crystallography without and with disorder highlighted by a red box.....122

Figure 4.12. Comparison of halogen bonding interactions between TCTNB and CPNB dimers. 123

Figure 4.13. Salt of compound **5**/4-PICO (one conformer shown).....125

Figure 4.14. Salt of compound **5**/DMAP (one conformer shown). 125

Figure 4.15. Stacked Raman spectra of unbound IPNB (blue), unbound THF (red), and IPNB/THF mixture (green)with zoomed in stacked Raman spectra in DCE.....127

Figure 4.16. Stacked FT-IR spectra of compound **2** (PNA, black) and compound **3** (HNB, blue) with amine and nitro-group peaks highlighted with red arrows. 134

Figure 4.17. Stacked Raman spectra of HNB (green) and IPNB (red) with zoomed range (100-400 cm^{-1}) for observed C-I stretch of IPNB. 135

Figure 4.18. DSC trace of pentanitroaniline. 136

Figure 4.19. DSC trace of hexanitrobenzene. 136

Abstract

Non-covalent interactions are critical components in the synthetic toolbox to modulate self-assembly processes and molecular recognition. One of the major goals in supramolecular chemistry is to understand how the properties of non-covalently bound structures correlate to interaction propensity in different states (i.e. gas phase, solution, and solid-state). Various computational methods involving electrostatic properties (i.e. electrostatic potentials) and theoretical binding energies (ΔE_{bind}) have been explored in order to establish prediction criteria to aid the development of new compounds within the field of active pharmaceutical ingredients (APIs) and energetic materials. Methodologies that support the formation of strong and directional hydrogen bonding and halogen bonding interactions, a directional non-covalent interaction between a halogen atom and an electron rich donor, most commonly feature the concept of cocrystallization which combines two or more neutral compounds in a defined ratio to produce crystalline complexes. A few ways to modify the properties of existing compounds are through changes in crystallization conditions which result in various forms (polymorph, hydrate, solvate, or cocrystal).

The work presented here in this thesis is geared toward the expansion of current understanding of how complementary synthon selection parameters can be translated into powerful, predictive tools toward the development of novel supramolecular assemblies. The utility of prediction methods toward the pursuit of new, strongly bound, energetic and non-energetic hydrogen and halogen bonded complexes are highlighted. Moreover, emphasis on how a structural

library-based approach can be used to understand the role structural modifications (i.e. changes in intramolecular bonding patterns and substituents) have on substrate scope could lead to the development of more efficient synthon screening techniques. In Chapter 2, a method is implemented to identify hydrogen peroxide solvate (peroxosolvate) formation within N-heterocyclic compounds having known hydrates to improve physical and chemical properties relative to the anhydrous form. This approach relies on the rich structural information within the Cambridge Structural Database (CSD) and understanding the reactivity of pyridyl-groups in the presence of concentrated hydrogen peroxide. In Chapter 3, a discrepancy between predictions based on electrostatic potential energy difference (ΔV_s) and computed ΔE_{bind} is presented then assessed through experimental determination of the relative strength of halogen bonding interactions in solution by the direct observation of halogen bonded complexes (iodine interacting with pyridyl nitrogen: C-I⋯N) by Raman spectroscopy. Experimental observations are rationalized using absolutely-localized molecular orbital energy decomposition analysis (ALMO-EDA) which points to the dominant contribution charge transfer (CT) has in the ranking of binding strengths. Chapter 4 details a proof of concept toward capitalizing on the unique nature of halogen bonds to form predictable and strong interactions in the solid-state. Previous studies on 1,3,5-trihalo-2,4,6-trinitrobenzenes (TXTNB, where X=Cl, Br, and I) and solution phase halogen bonding are utilized as springboards toward the synthesis, cocrystallization, and halogen bonding interaction strength determination of strongly bound poly-nitrated benzene derivatives. The utilization of cocrystallization strategies that translate prediction models between different phases display limitations that could be addressed when considering the affects stability and donor/acceptor pair compatibility have on halogen bonding interactions. To close, Chapter 5 is a

conclusion to the work presented in this thesis that provides groundwork for the development and stabilization of new supramolecular assemblies.

Chapter 1

Introduction

The work presented in this thesis provides insight into methodologies that have been developed to aid in the understanding of non-covalent interaction formation in the solid state and solution phases. This introductory chapter sets the framework for studies regarding the development of energetic and non-energetic materials through non-covalent interactions, specifically using hydrogen and halogen bonding to direct the formation of predictable self-assemblies.

1.1 Non-covalent Interactions

Non-covalent interactions are a class of intermolecular interactions with significant impact on the fields of crystal engineering,[1] molecular recognition,[2] and supramolecular chemistry.[3] Two types of analogous non-covalent interactions are hydrogen and halogen bonding interactions and commonly feature an electron donor moiety (i.e. electronegative atoms or substituents with lone pairs) and an electron acceptor moiety (i.e. hydrogen and halogen atoms) as shown in **Figure 1.1**. [4,5]

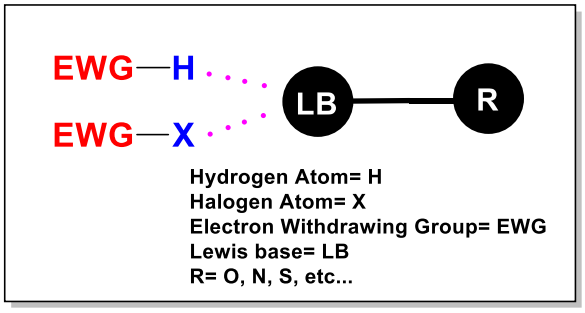


Figure 1.1. Simple representation of hydrogen and halogen bonding interactions.

More specifically, the electron acceptor moiety for a hydrogen bond (HB) is a hydrogen bond donor and for a halogen bond (XB) it is a halogen bond donor. While hydrogen bonding is the most prevalent and well-studied of the two non-covalent interactions,[6] halogen bonding is reported to be more tunable and directional than hydrogen bonding.[5,7,8] In halogen bonding interactions, the σ-hole,[9] a region of positive electrostatic potential along the axis of the covalently bound halogen, is characterized by a myriad of attractive electronic factors[10] that allows for interactions to occur with Lewis bases (LBs).

Studies have shown that because hydrogen and halogen bonding interactions are fairly similar,[11–13] competition can occur between them within crystalline materials and in solution.[14] Often times this competition favors hydrogen bonding which tends to be more prevalent because of the ubiquity of moieties that feature hydrogen atoms based on knowledge acquired from known crystal structures found in the Cambridge Structural Database (CSD).[15] However, halogen bonding strength can be modulated depending on the polarizability of the halogen atom (F << Cl < Br < I, **Figure 1.2**)[7] and the addition of electron withdrawing groups (EWGs) to activate the σ-hole can lead to it becoming the more dominant force that facilitates complex formation.[16] Note that the σ-hole magnitude is relative to the polarizability of the halogen atom and thus larger atoms form halogen bonds more readily than smaller ones.[7,17,18] Moreover, in cases where hydrogen bonding moieties are absent or are not tolerated within reaction media, halogen bonding can be utilized as a hydrogen bonding alternative.[19,20]

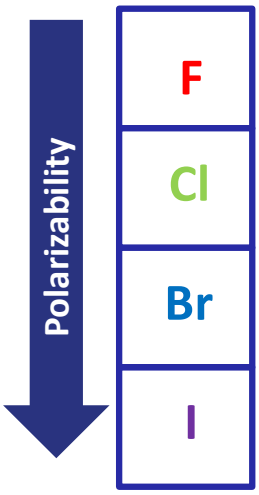


Figure 1.2. Illustration of increasing polarizability based on the halogen atom.

In recent years, experimental and theoretical evidence have emerged that support the design of strong hydrogen[1,21,22] and halogen bonded complexes[23,24] based on the nature of the bonded motifs within each interaction. Traditional hydrogen bonding motifs have a hydrogen atom covalently bound to an electronegative atom or molecule (i.e. hydrogen bond acceptor) as shown in **Figure 1.3a**,[4] though non-classical HB interactions do occur (**Figure 1.3b**).[25,26] The stronger of the two types of hydrogen bonding interactions is the traditional given the impact that of the electronegative atoms (N, O, S, etc…) have on the hydrogen atom by enhancing its attractive nature. Halogen bonding interactions,[27] though, feature a covalently bound halogen atom interacting with an electronegative atom or molecule (i.e. halogen bond acceptor) at ~180º along the axis of the covalent bond (**Figure 1.4**).[7] Large halogens like bromine (Br) and iodine (I) are more prone to halogen bond with a LB than chlorine (Cl) and much more likely than fluorine (F), which rarely forms halogen bonding interactions though there are special cases where it does.[28–31] The advantage of implementing hydrogen and halogen bonding interactions into supramolecular design strategies lies within the availability of the donors and the ability to modulate the properties of the donors and acceptors by influencing the electronic environment of the components and the surrounding environment.[32]

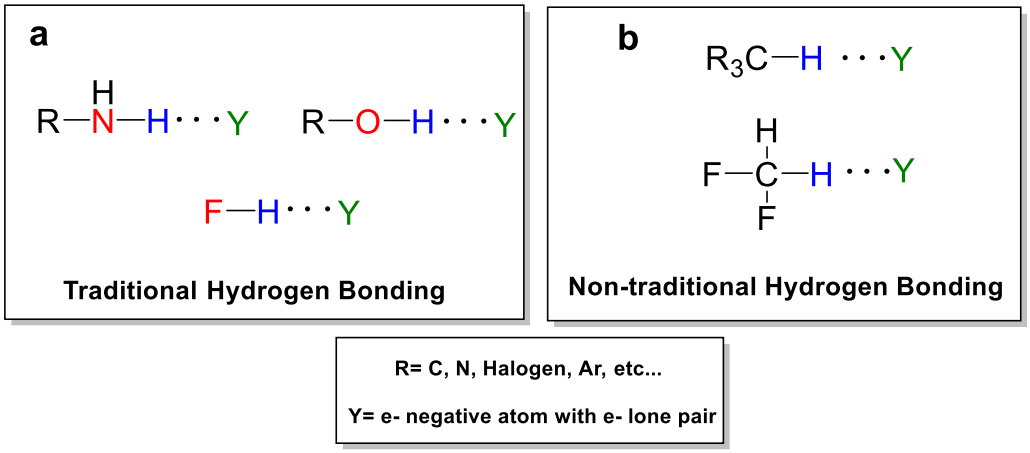


Figure 1.3a-b. Traditional and non-traditional hydrogen bonding interactions.

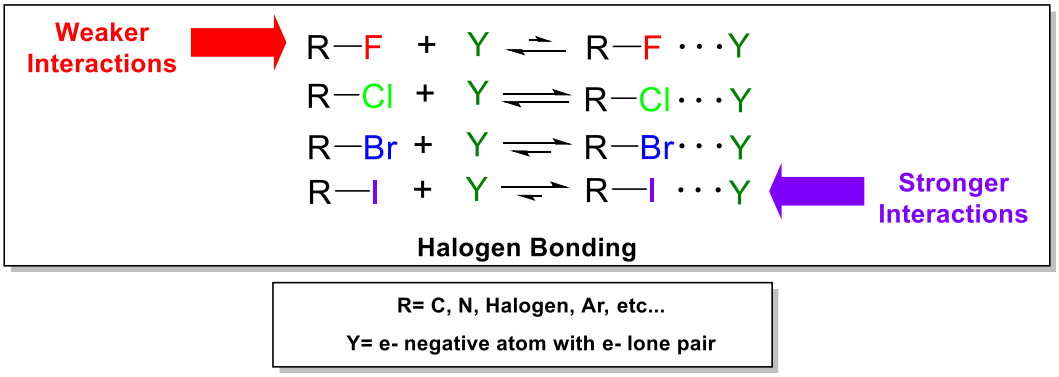


Figure 1.4. Halogen bonding interactions with halogen atoms and arbitrary Lewis bases.

1.2 Predictions of Supramolecular Assemblies

Experimental observations and computational models have been used to distinguish between the nature and strength of hydrogen[33,34] and halogen [35–37]bonding interactions and predict their formation within various states (i.e. solid and solution phases).[38] A common method used to predict interaction propensity is through electrostatic potential (ESP) maps,[39–41] a quantitative representations of charge distribution characterized by maximum electrostatic potential ($V_{s,max}$) which is relevant to the hydrogen atom/σ-hole and minimum electrostatic potential ($V_{s,min}$) values which apply to the lone pairs of a HB/XB acceptor, respectively. Notably, in regard to halogen bonding, the $V_{s,max}$ value, which correlates to the magnitude of the σ-hole, is used to quantify the strength of the XB donor while the $V_{s,min}$ value is used to quantify the strength of the XB acceptor. Predictions based on the energy difference between $V_{s,max}$ and $V_{s,min}$ values (denoted as ΔV_s, as shown in **Figure 1.5**) constitute one way theoretical methodologies are applied to experimental systems. If the ΔV_s value is large, then the donor/acceptor pair is suggested to interact strongly with one another. ΔV_s values provide insight to the possibilities of a donor and acceptor pair interacting favorably. [39]

Another theoretical method utilized evaluates theoretical binding energy or ΔE_{bind},[42] which is associated with the energy of the complex (denoted as donor/acceptor, DA complex) as

well as its individual parts (XB donor and XB acceptor) as shown in **Figure 1.6**. If the ΔE_{bind} value is large and negative, then the formation of the complex is favorable. ΔE_{bind} can be further broken down into meaningful energy terms (electrostatics, dispersion, polarization, and charge transfer) using absolutely-localized molecular orbital energy decomposition analysis (ALMO-EDA).[43]

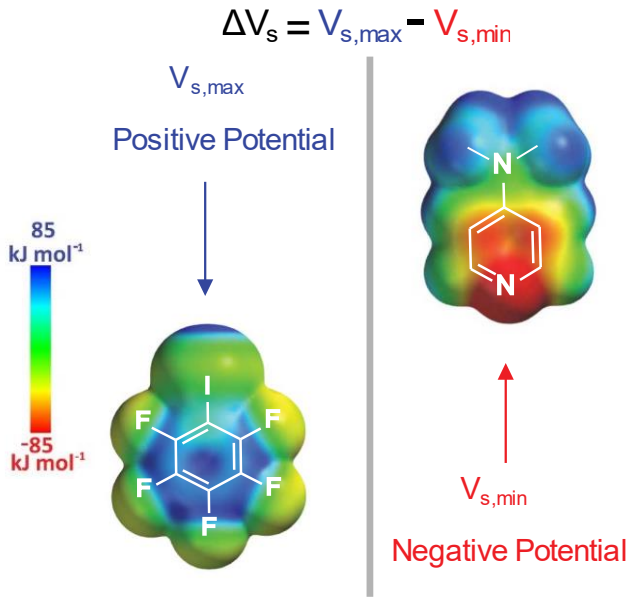


Figure 1.5. Electrostatic potential (ESP) maps that depict $V_{s,max}$, $V_{s,min}$, and ΔV_s calculations using the density functional method B3LYP/6-311G**.

$$\Delta E_{bind} = E_{DA\ Complex} - (E_{XB\ Donor} + E_{XB\ Acceptor})$$

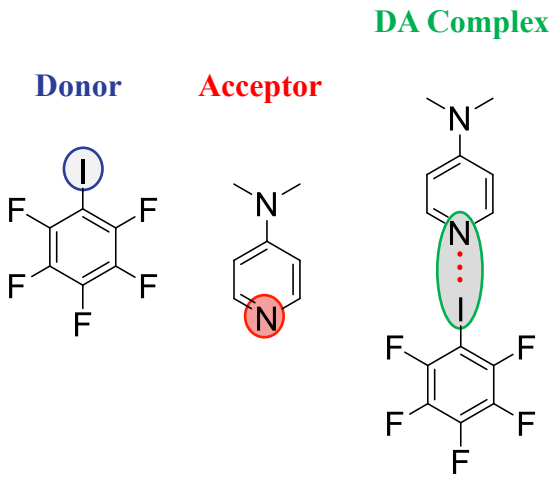


Figure 1.6. Theoretical binding energy (ΔE_{bind}) calculated using the density functional method B3LYP/6-311G**.

Over the years, a series of debates have taken place with regard to the relative contributions that polarization, charge-transfer, dispersion, and electrostatic attraction have on non-covalently bound complexes.[24] While hydrogen bonding can be considered an electrostatic attraction, reports have characterized the interaction by the covalent character of the bond and thus many different energy contributions are incorporated into the overall description profile.[44] Similarly to hydrogen bonding, in halogen bonding, the nature of the interactions was thought to be strictly due to electrostatic attraction,[7,8,45] but others[24,46–48] have come to a different conclusion which suggests that the characteristics of a halogen bond are the product of a mixture of contributions (i.e. polarization, charge-transfer, dispersion, and electrostatic attraction). Computational modeling provides guidelines for the design of favorable complexes; the methodologies allow for the theoretical determination of dominant forces that facilitate the assembly of complexes that could form under different environmental conditions.

1.3 Cocrystallization in Energetic and Non-Energetic Materials

The design of new energetic materials,[49,50] compounds that upon decomposition release energy in the form of heat and neutral molecular components at a high rate, with improved physical and chemical properties is a central goal in the field of aerospace and to the military. These materials can be further broken down into subcategories known as explosives (primary and secondary), pyrotechnics, and propellants (**Figure 1.7**).[51]

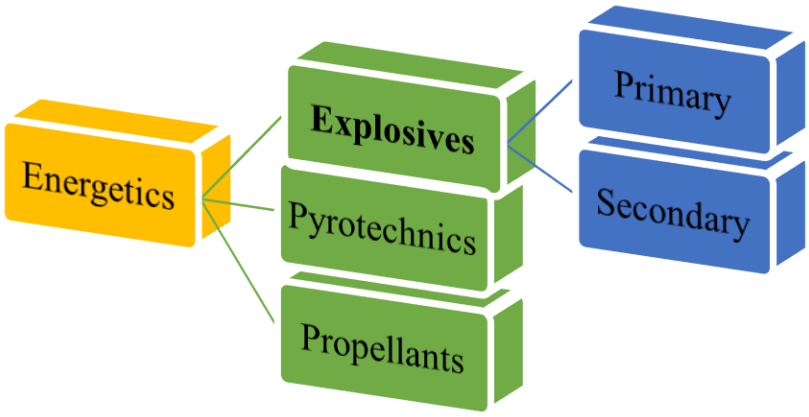


Figure 1.7. Breakdown of the categories of energetic materials.

When trying to develop new energetics using solid state crystal engineering, there are a few things to consider which include 1) oxygen balance of the energetic and 2) possible changes in the physical form that a compound can take considering they can have dramatic impact on its physiochemical properties. Oxygen balance (OB) describes the amount of oxidant present relative to the amount required to completely convert all fuel atoms.[52] The oxygen balance for organic materials can be calculated using the following equation:

Equation 1.1: $OB = -1600/MW(2a + b - 2 - d)$

where *a*, *b*, *c*, and *d* are the number of carbon (C), hydrogen (H), oxygen (O), halogen (X= Cl, Br, I, etc…), and sulfur (S) atoms, respectively, and MW is the molecular weight.[53] A positive OB denotes that there is excess oxygen in the system after full conversion, whereas a negative OB refers to an insufficient amount of oxygen and typically results in the generation of carbon soot and lower-oxidized, toxic gases (CO and NO). As an example, the energetic 2,4,6-trinitrotoluene (TNT) is a commonly used secondary explosive (i.e. low sensitivity) for mining purposes. TNT has a calculated oxygen balance of -74%[54] which means it does not have enough oxidant to convert its atoms into fuel and thus produces harmful byproducts like toxic gases that are left in the environment after detonation.

In regard to different forms, there is a lot of diversity in solid-state forms that can change depending on the crystallization conditions and as a result, different arrangements of the same molecule (polymorphs)[55–57] can form. On the other hand, different states of matter can result from diverse methods used to crystallize the molecules (hydrates, solvates, or cocrystals)[58]. Crystal engineering strategies support the development of new energetic materials through cocrystal synthesis which result in molecular structures stabilized via non-covalent interactions. Cocrystallization,[59,60] a technique that combines two or more neutral molecular species in a defined ratio to produce a solid material containing both species, is a proven method used to modify the properties (i.e. improve the performance parameters) of existing energetic materials (**Figure 1.8**).[61,62] One of the most powerful energetics, 2,4,6,8,10,12-hexanitro-2,4,6,8,10,12-hexaazaisowurtzitane or CL-20, has benefited from cocrystallization with TNT which led to the cocrystal[63] of CL-20 (Ref code IZUZUZ02, **Figures 1.9** and **1.10**) with increased stability than anhydrous CL-20. Hydrogen bonding interactions aid in the stabilization of the crystal lattice of the CL-20/TNT cocrystal.

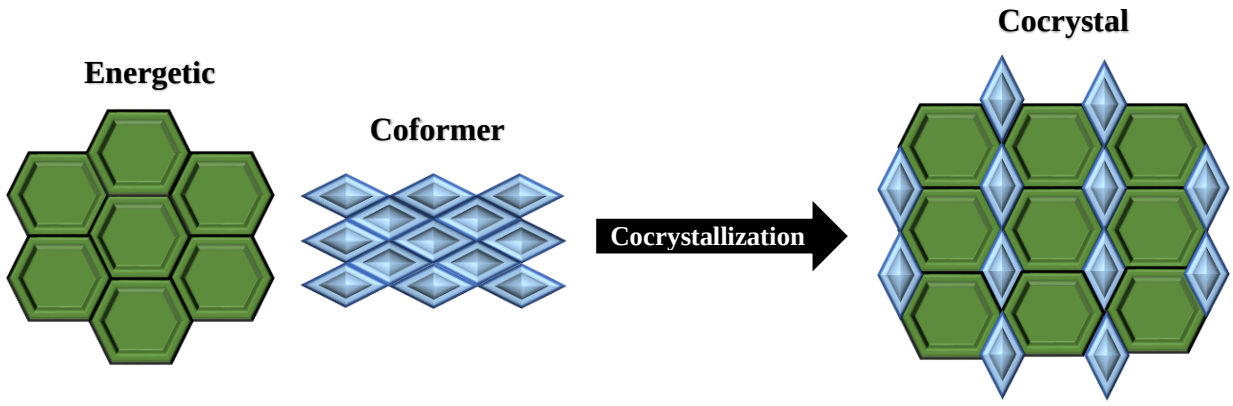
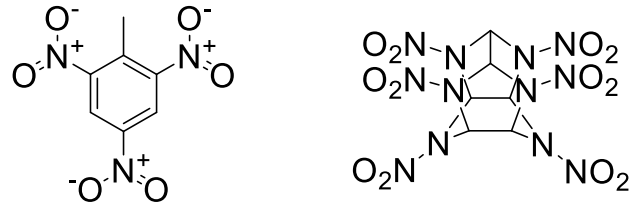


Figure 1.8. Illustration of the cocrystallization technique.



2,4,6-trinitrotoluene
(TNT)

2,4,6,8,10,12-hexanitro-
2,4,6,8,10,12-hexaazaisowurtzitane
(CL-20)

Figure 1.9. Chemical structures of TNT and CL-20.

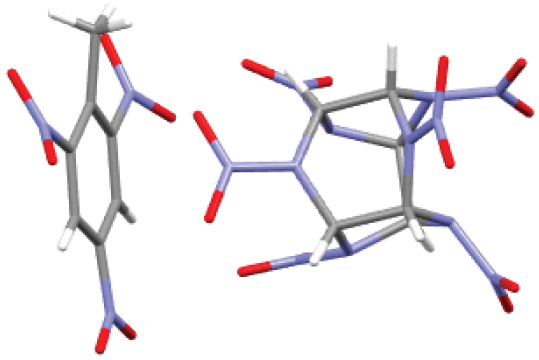


Figure 1.10. CL-20/TNT cocrystal (IZUZUZ02).

The 1,3,5-trihalo-2,4,6-trinitrobenzene (TXTNB, X= Cl, Br, or I) series of polynitrobenzene derivatives have been explored as coformers toward the design of energetic cocrystals stabilized via halogen bonding interactions. Two prime examples of energetic halogen bonded complexes are the 1:1 diacetone diperoxide and 1,3,5-triiodo-2,4,6-trinitrobenzene (DADP/TITNB)[64] and 2:1 1,3,5-trinitrobenzene (TNB)/TITNB cocrystals. In the 1:1 DADP/TITNB cocrystal, the impact sensitivity is reduced compared to the pure starting components due to the halogen-peroxide (I···O) interactions displayed in the crystal structure. Furthermore, the 2:1 TNB/TITNB cocrystal[65] capitalized on not only the halogen bond donation ability of iodine atoms but could also be utilized for its biocidal properties.

Modification of cocrystallization conditions have led to the development of new forms of energetic materials and active pharmaceutical ingredients (APIs). It is common for energetics and APIs to form hydrates, a class of multicomponent crystals containing water, within synthesis, cocrystallization, storage, and shipment.[66–69] As a result, hydrate formation can lead to performance issues as favorable properties decrease (e.g. stability and negative OB, respectively). In place of hydrate formation, interest has been shown toward incorporating hydrogen peroxide (HP), a well-known antimicrobial and oxidizing agent, into molecular design strategies to improve physical and chemical properties. Kersten et. al.[70] introduced a new pharmaceutical solvate of HP (peroxosolvate), produced using cocrystallization. It was reported that the incorporation of HP lead to an increase in the antimicrobial properties of the antifungal cream Miconazole in addition to improvements in its solubility. Another case of HP incorporation within the crystal lattice of a compound is with the energetic CL-20. What is notable about this case is that CL-20 has four commonly encounter forms[71] and one of which is a hydrate (specifically a quarter hydrate)[72]: this form showed positive implications toward increasing oxygen balance and thus overall performance of CL-20 due to the inclusion of water. Thus HP, having structural similarities to water, was thought to be a good replacement for water. The detailed investigations of Bennion et al.[52] explored using HP as a coformer for CL-20. These investigations lead to the successful synthesis of two novel peroxosolvates of α-CL-20.

Miconazole and CL-20 are well known coformers that have benefited from HP incorporation which increased stability and improved the performance properties over neat CL-20, respectively. These compounds served as suitable HP coformers given that structurally, neither have better hydrogen bond donor moieties than HP. When comparing both the hydrates and solvates of Miconazole and CL-20, hydrogen peroxide acts as a stronger hydrogen bond donor

than water and always donates at least two hydrogen bonds unlike with water, which has been reported by Chernyshov et al. and Medvedev et al.[73,74] Recently, Foroughi et al. successfully demonstrated that by using the CSD as a tool to apply HP coformer criteria, peroxosolvate formation could be predicted based on the hydrate forms of commercially available cyclic *N*-oxides.[75] Collectively, the successes that literature precedence have shown toward the formation of novel energetic and non-energetic materials through cocrystal engineering provide fundamental frameworks in relation to future endeavors.

Hydrogen and halogen bonding interactions have been applied in a multitude of design strategies to produced strong, directional, tunable, and predictable assemblies. These interactions have been assessed for their strength and overall propensity of formation through both theoretical calculations and experimental evaluations. Altogether, the collection of novel energetic and non-energetic materials (e.g. APIs) has steadily increased from the incorporation of hydrogen and halogen bonding interactions coupled with advancements made with cocrystallization techniques.

1.4 Outline of Thesis

This thesis describes experimental observations and theoretical prediction models used to understand the fundamental properties of hydrogen and halogen bonding interactions. Chapter 2 contains the application of a database approach to select N-heterocyclic coformers for hydrogen peroxide, based on their hydrate forms, to produce new hydrogen peroxide solvates. Chapter 3 involves the experimental observation of halogen bonding interactions in solution with interaction propensity predicted by computational modeling. Chapter 4 entails the formation of multicomponent crystals of polynitrobenzene derivatives facilitated by halogen bonding interactions. Finally, Chapter 5 summarizes the connection between the experimental and computational evaluations for the non-covalent interactions of the prior mentioned Chapters.

1.5 References

[1] A. Priimagi, G. Cavallo, P. Metrangolo, G. Resnati, *Acc. Chem. Res.* **2013**, *46*, 2686–2695.

[2] L. Escobar, P. Ballester, *Chem. Rev.* **2021**, *121*, 2445–2514.

[3] S. K. Seth, D. Sarkar, A. Roy, T. Kar, *CrystEngComm.* **2011**, *13*, 6728.

[4] E. Arunan, G. R. Desiraju, R. A. Klein, J. Sadlej, S. Scheiner, I. Alkorta, D. C. Clary, R. H. Crabtree, J. J. Dannenberg, P. Hobza, H. G. Kjaergaard, A. C. Legon, B. Mennucci, D. J. Nesbitt, *Pure Appl. Chem.* **2011**, *83*, 1637–1641.

[5] G. R. Desiraju, P. S. Ho, L. Kloo, A. C. Legon, R. Marquardt, P. Metrangolo, P. Politzer, G. Resnati, K. Rissanen, *Pure Appl. Chem.* **2013**, *85*, 1711–1713.

[6] T. Steiner, *Angew. Chem. Int. Ed.* **2002**, *41*, 48–76.

[7] P. Politzer, J. S. Murray, T. Clark, *Phys. Chem. Chem. Phys.* **2010**, *12*, 7748.

[8] Z. P. Shields, J. S. Murray, P. Politzer, *Int. J. Quantum Chem.* **2010**, *110*, 2823–2832.

[9] P. Politzer, J. S. Murray, T. Clark, *Phys. Chem. Chem. Phys.* **2013**, *15*, 11178–11189.

[10] E. Engelage, D. Reinhard, S. M. Huber, *Chem. Eur. J.* **2020**, *26*, 3843–3861.

[11] P. Metrangolo, G. Resnati, *Science.* **2008**, *321*, 918–919.

[12] P. Metrangolo, H. Neukirch, T. Pilati, G. Resnati, *Acc. Chem. Res.* **2005**, *38*, 386–395.

[13] P. Metrangolo, T. Pilati, G. Terraneo, S. Biella, G. Resnati, *CrystEngComm.* **2009**, *11*, 1187.

[14] C. B. Aakeröy, C. L. Spartz, S. Dembowski, S. Dwyre, J. Desper, *IUCrJ.* **2015**, *2*, 498–510.

[15] C. R. Groom, I. J. Bruno, M. P. Lightfoot, S. C. Ward, *Acta Crystallogr., Sect. B: Struct. Sci. Cryst. Eng. Mater.* **2016**, *72*, 171–179.

[16] B. Zha, J. Li, J. Wu, X. Miao, M. Zhang, *New J. Chem.* **2019**, *43*, 17182–17187.

[17] H. Fan, J. K. Eliason, C. D. Moliva A., J. L. Olson, S. M. Flancher, M. W. Gealy, D. J. Ulness, *J. Phys. Chem. A* **2009**, *113*, 14052–14059.

[18] B. Hawthorne, H. Fan-Hagenstein, E. Wood, J. Smith, T. Hanks, *Int. J. Spectrosc.* **2013**, *2013*, 1-10.

[19] C. B. Aakeröy, M. Fasulo, N. Schultheiss, J. Desper, C. Moore, *J. Am. Chem. Soc.* **2007**, *129*, 13772–13773.

[20] A. Wasilewska, M. Gdaniec, T. Połoński, *CrystEngComm.* **2007**, *9*, 203–206.

[21] K. B. Moore, K. Sadeghian, C. D. Sherrill, C. Ochsenfeld, H. F. Schaefer, *J. Chem. Theory Comput.* **2017**, *13*, 5379–5395.

[22] A. C. Legon, *Phys. Chem. Chem. Phys.* **2010**, *12*, 7736.

[23] G. Cavallo, P. Metrangolo, R. Milani, T. Pilati, A. Priimagi, G. Resnati, G. Terraneo, *Chem. Rev.* **2016**, *116*, 2478–2601.

[24] L. P. Wolters, P. Schyman, M. J. Pavan, W. L. Jorgensen, F. M. Bickelhaupt, S. Kozuch, *WIREs Comput Mol Sci.* **2014**, *4*, 523–540.

[25] R. C. Johnston, P. H.-Y. Cheong, *Org. Biomol. Chem.* **2013**, *11*, 5057.

[26] X. Zhang, H. Dai, H. Yan, W. Zou, D. Cremer, *J. Am. Chem. Soc.* **2016**, *138*, 4334–4337.

[27] T. Clark, M. Hennemann, J. S. Murray, P. Politzer, *J. Mol. Model.* **2007**, *13*, 291–296.

[28] P. Cardillo, E. Corradi, A. Lunghi, S. Valdo Meille, M. Teresa Messina, P. Metrangolo, G. Resnati, *Tetrahedron.* **2000**, *56*, 5535–5550.

[29] P. Metrangolo, J. S. Murray, T. Pilati, P. Politzer, G. Resnati, G. Terraneo, *Cryst. Growth Des.* **2011**, *11*, 4238–4246.

[30] M. Cametti, B. Crousse, P. Metrangolo, R. Milani, G. Resnati, *Chem. Soc. Rev.* **2012**, *41*, 31–42.

[31] M. S. Pavan, K. Durga Prasad, T. N. Guru Row, *Chem. Commun.* **2013**, *49*, 7558.

[32] D. P. Devore, T. L. Ellington, K. L. Shuford, *J. Phys. Chem. A.* **2020**, *124*, 10817–10825.

[33] S. Emamian, T. Lu, H. Kruse, H. Emamian, *J. Comput. Chem*. **2019**, *40*, 2868–2881.

[34] G. R. Desiraju, *Acc. Chem. Res.* **1996**, *29*, 441–449.

[35] A. Mukherjee, S. Tothadi, G. R. Desiraju, *Acc. Chem. Res.* **2014**, *47*, 2514–2524.

[36] S. T. Nguyen, T. L. Ellington, K. E. Allen, J. D. Gorden, A. L. Rheingold, G. S. Tschumper, N. I. Hammer, D. L. Watkins, *Cryst. Growth Des.* **2018**, *18*, 3244–3254.

[37] L. P. Wolters, F. M. Bickelhaupt, *ChemistryOpen.* **2012**, *1*, 96–105.

[38] S. A. C. McDowell, *J. Chem. Phys.* **2010**, *132*, 044312.

[39] D. Musumeci, C. A. Hunter, R. Prohens, S. Scuderi, J. F. McCabe, *Chem. Sci.* **2011**, *2*, 883.

[40] J. S. Murray, P. Politzer, *WIREs Comput Mol Sci.* **2011**, *1*, 153–163.

[41] J. S. Murray, P. Politzer, *J. Mol. Struct: THEOCHEM*. **1998**, *425*, 107–114.

[42] J. Yang, B. Hong, N. Wang, X. Li, X. Huang, Y. Bao, C. Xie, H. Hao, *CrystEngComm.* **2019**, *21*, 6374–6381.

[43] T. A. Bramlett, A. J. Matzger, *Chem. Eur. J.* **2021**, *27*, 15472–15478.

[44] G. R. Desiraju, *Acc. Chem. Res.* **2002**, *35*, 565–573.

[45] K. E. Riley, J. S. Murray, P. Politzer, M. C. Concha, P. Hobza, *J. Chem. Theory Comput.* **2009**, *5*, 155–163.

[46] A. J. Stone, *J. Am. Chem. Soc.* **2013**, *135*, 7005–7009.

[47] S. M. Huber, J. D. Scanlon, E. Jimenez-Izal, J. M. Ugalde, I. Infante, *Phys. Chem. Chem. Phys.* **2013**, *15*, 10350.

[48] S. V. Rosokha, C. L. Stern, J. T. Ritzert, *Chem. Eur. J.* **2013**, *19*, 8774–8788.

[49] W. Pang, L. T. DeLuca, A. A. Gromov, A. S. Cumming, Eds., *Innovative Energetic Materials: Properties, Combustion Performance and Application*, Springer Singapore, Singapore, **2020**.

[50] M. K. Shukla, V. M. Boddu, J. A. Steevens, R. Damavarapu, J. Leszczynski, Eds., *Energetic Materials: From Cradle to Grave*, Springer International Publishing, Cham, **2017**.

[51] U. Teipel, Ed., *Energetic Materials: Particle Processing and Characterization*, Wiley, **2004**.

[52] J. C. Bennion, N. Chowdhury, J. W. Kampf, A. J. Matzger, *Angew. Chem. Int. Ed.* **2016**, *55*, 13118–13121.

[53] J. C. Bennion, A. J. Matzger, *Acc. Chem. Res.* **2021**, *54*, 1699–1710.

[54] I. Sochet, D. Gardebas, S. Calderara, Y. Marchal, B. Longuet, *OJSST*. **2011**, *01*, 31–42.

[55] J. Bernstein, *Polymorphism in Molecular Crystals.*, International Union Of Crystallography, Oxford University Press Inc, New York, **2002**.

[56] S. Y. Qi, Y. Tian, W. B. Zou, C. Q. Hu, *Front. Chem.* **2018**, *6*, 506.

[57] A. Nangia, *Acc. Chem. Res.* **2008**, *41*, 595–604.

[58] E. Grothe, H. Meekes, E. Vlieg, J. H. ter Horst, R. de Gelder, *Cryst. Growth Des*. **2016**, *16*, 3237–3243.

[59] R. A. Wiscons, N. R. Goud, J. T. Damron, A. J. Matzger, *Angew. Chem. Int. Ed.* **2018**, *57*, 9044–9047.

[60] D. Yan, A. Delori, G. O. Lloyd, T. Friščić, G. M. Day, W. Jones, J. Lu, M. Wei, D. G. Evans, X. Duan, *Angew. Chem. Int. Ed.* **2011**, *50*, 12483–12486.

[61] J. Zhang, J. M. Shreeve, *CrystEngComm* **2016**, *18*, 6124–6133.

[62] L. M. Foroughi, R. A. Wiscons, D. R. Du Bois, A. J. Matzger, *Chem. Commun.* **2020**, *56*, 2111–2114.

[63] Y. Liu, C. An, J. Luo, J. Wang, *Acta Crystallogr., Sect. B: Struct. Sci. Cryst. Eng. Mater.* **2018**, *74*, 385–393.

[64] K. B. Landenberger, O. Bolton, A. J. Matzger, *J. Am. Chem. Soc.* **2015**, *137*, 5074–5079.

[65] J. C. Bennion, L. Vogt, M. E. Tuckerman, A. J. Matzger, *Cryst. Growth Des*. **2016**, *16*, 4688–4693.

[66] H. D. Clarke, K. K. Arora, H. Bass, P. Kavuru, T. T. Ong, T. Pujari, L. Wojtas, M. J. Zaworotko, *Cryst. Growth Des*. **2010**, *10*, 2152–2167.

[67] A. M. Healy, Z. A. Worku, D. Kumar, A. M. Madi, *Adv. Drug Deliv. Rev.* **2017**, *117*, 25–46.

[68] M. Ghosh, V. Venkatesan, S. Mandave, S. Banerjee, N. Sikder, A. K. Sikder, B. Bhattacharya, *Cryst. Growth Des*. **2014**, *14*, 5053–5063.

[69] A. T. Nielsen, A. P. Chafin, S. L. Christian, D. W. Moore, M. P. Nadler, R. A. Nissan, D. J. Vanderah, R. D. Gilardi, C. F. George, J. L. Flippen-Anderson, *Tetrahedron* **1998**, *54*, 11793–11812.

[70] K. M. Kersten, M. E. Breen, A. K. Mapp, A. J. Matzger, *Chem. Commun.* **2018**, *54*, 9286–9289.

[71] X. J. Xu, W.-H. Zhu, H.-M. Xiao, *J. Phys. Chem. B* **2007**, *111*, 2090–2097.

[72] Y. Yu, S. Jin, J. Zhu, L. Li, S. Chen, Q. Shu, *Zeitschrift für Kristallographie - New Crystal Structures.* **2016**, *231*, 491–492.

[73] I. Yu. Chernyshov, M. V. Vener, P. V. Prikhodchenko, A. G. Medvedev, O. Lev, A. V. Churakov, *Cryst. Growth Des.* **2017**, *17*, 214–220.

[74] A. G. Medvedev, A. V. Churakov, P. V. Prikhodchenko, O. Lev, M. V. Vener, *Molecules.* **2020**, *26*, 26.

[75] L. M. Foroughi, A. J. Matzger, *Cryst. Growth Des.* **2021**, *21*, 5873–5879.

Chapter 2

Leveraging Existing Structural Data for the Discovery of Novel Hydrogen Peroxide Solvates

2.1 Introduction

The formation of solid forms containing solvent (solvates) as an integral component is often viewed as a nuisance. Solvates may require further processing to reduce undesirable carryover of reactive or toxic solvents, and in some cases, solvent removal leads to loss of crystallinity.[1] In the case of hydrates, which represent the largest class of solvates in the Cambridge Structural Database (CSD)[2,3], the ubiquity of water means that hydrated forms can appear unintentionally during synthesis, purification, and storage.[4–6] Although of little consequence for understanding molecular structure, in the case of pharmaceuticals[2,7] or energetic materials[8], performance is generally degraded by the inclusion of water. Recently, we have investigated how propensity towards solvent inclusion can be leveraged to provide new functionality to solid forms.[8,9] This was accomplished by the inclusion of hydrogen peroxide (H_2O_2), in place of water, to improve energetic performance or add functionality to a pharmaceutical.

Although certain functional groups can increase the propensity towards solvate formation, the interplay of these interactions, with other intermolecular interactions that contribute to crystal packing, makes prediction of solvate formers uncertain from the crystal structure of a pure component.[10,11] However, if a hydrated form is already known then understanding the similarities

and differences between the solvate, here H_2O_2, and water can substantially improve the odds of success.[12] While water can act as either a hydrogen bond (HB) acceptor or donor during hydrate formation, studies of all of the H_2O_2 solvate (peroxosolvate) structures in the CSD have shown that H_2O_2 consistently donates two hydrogen bonds (while HB accepting interactions do not always occur).[12,13] Notably, H_2O_2 is a better HB donor than water and thus better facilitates the formation of peroxosolvates over hydrates in the presence of good HB acceptors. We have recently demonstrated this approach for cyclic *N*-oxides by utilizing the CSD to identify crystalline hydrates where water serves as a HB donor.[14] Compounds that met our search criteria and were commercially available were crystallized in the presence of H_2O_2 and all six compounds studied formed peroxosolvates.

Here the problem of peroxosolvate formation is addressed for molecules with sp^2-hybridized nitrogen atoms. This is a class of compounds very poorly represented in the CSD with only eight peroxosolvate structures with peroxide O-H···N (sp^2 nitrogen) interactions (compared to thousands of hydrate entries with close contacts between an sp^2 nitrogen and water), yet extremely important in energetic materials, where nitrogen-rich molecules are commonly used.[15,16] We hypothesized that this dearth resulted not from a poor propensity for solvate formation, but rather due to competing modes of reactivity, including the oxidation to an *N*-oxide group.[17] In fact, a recent review has listed an absence of a possible redox reaction with H_2O_2 as a necessary property for identifying coformers for peroxosolvate formation.[13] We demonstrate here that even reactive compounds (pyridines) can, in many cases, successfully yield peroxide solvates. A primary motivator for the peroxosolvate formation of energetic materials is to increase the oxygen content of the material without requiring synthesis. Most energetics suffer from a lack of

oxidizing power reflected in a negative oxygen balance[18,19], which we have demonstrated can be improved through the addition of oxygen-rich H_2O_2 (OB +47%) into the crystal lattice.[8,20]

Common sp^2 nitrogen containing moieties in energetic compounds include five and six membered heterocycles with one or more nitrogen on the ring (including triazoles, tetrazoles, pyrazines, and triazines).[21–24] Pyridine was selected as a test case for an sp^2 nitrogen containing aromatic ring that would likely yield coformers due to the large number of pyridine containing hydrates in the CSD (over a thousand) and its predicted strong interactions with hydrogen peroxide.[25] Additionally, despite the large number of hydrates, there are only two examples of organic peroxosolvates with a pyridine containing coformer (SEMXIU[26] and UKEFEV[27]) and in only one case, 2,3,5,6-tetrakis(pyridin-2-yl)pyrazine, do close contacts exist between the pyridine sp^2 nitrogen and H_2O_2 (the four pyridyl-groups accept hydrogen bonds from H_2O_2). To focus on a tractable set of molecules, the results of the CSD search were further evaluated to identify commercially available compounds that will likely form peroxosolvates based on the hydrogen bonding in their hydrate structure. This led to the identification of eight compounds that include an sp^2 nitrogen (the pyridine N) that accepts HBs from water. Upon treatment with H_2O_2/organic solvent mixtures, the eight compounds yielded eight new hydrogen peroxide solvates (pyridyl or *N*-oxide) and serve as model systems in design strategies that support peroxosolvate formation.

2.2 Results and Discussion

ConQuest[28] 2021.2.0 software was used to identify and compile a list of compounds from the CSD containing pyridyl-groups that act as hydrogen bond accepting moieties to water and could thus serve as coformers for H_2O_2. Contacts were made between each hydrogen in water to the nitrogen of a pyridyl-group (contact distance within the sum of the van der Waals radii, **Figure 2.1**), and filters were applied to create a tractable list of high-quality organic crystal structures (organics-only, non-disordered structures, and a R< = 0.075).

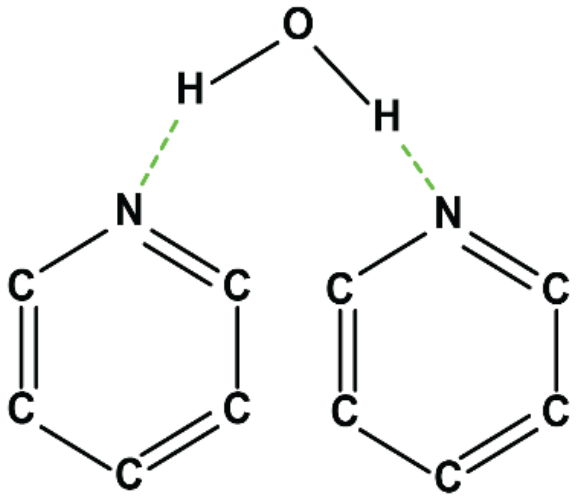


Figure 2.1. Illustration of the CSD search geometry.

The resulting CSD search yielded 224 entries that fit the search criteria and were further evaluated for commercial availability using SciFinder through the "get commercial sources" function, yielding eight compounds. All eight compounds were purchased through major vendors: 2,4,6-tris(2-pyridyl)-*s*-triazine (**1**), 2,9-dimethyl-1,10-phenanthroline (**2**)**,** 9-aminoacridine (**3**), 1,2-di(4-pyridyl)ethylene (**4a**), 5-chloro-3- [4-(methylsulfonyl)phenyl]-2-(2-methyl-5-pyridinyl)pyridine (**5**), 2-amino-7,7-dimethyl-5-oxo-4-pyridin-4-yl-5,6,7,8-4h-4h-chromene-3-carbonitrile (**6**), 4-methyl-N-(2-pyridinylmethyl)-benzenesulfonamide (**7a**), and N,N'-bis(3-pyridyl)urea (**8**) in **Figure 2.2**.

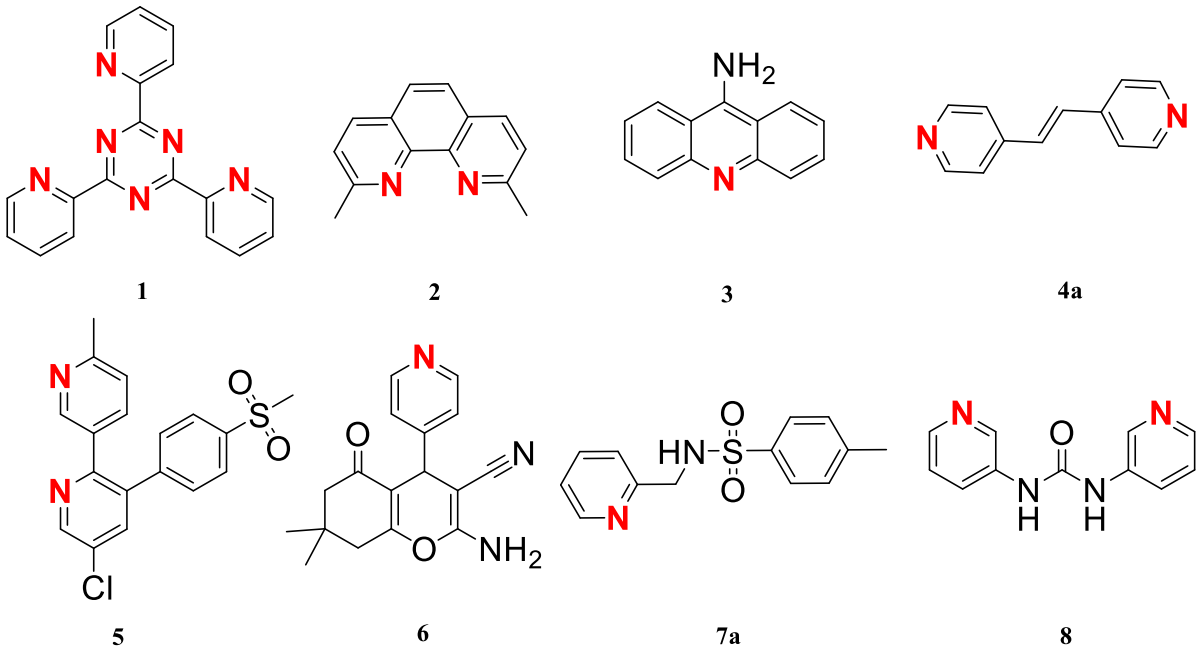
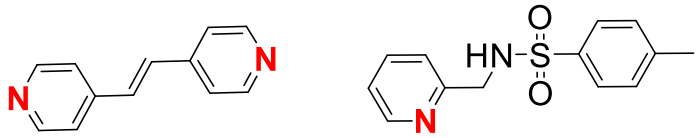


Figure 2.2. Structures of target compounds **1-8**.

Peroxosolvates were formed for six of the eight target compounds (**1**, **2**, **4a**, **5**, **7a**, and **8**) in either 98% H_2O_2, or a mixture of 98% H_2O_2 and an organic solvent (ACN or EtOAc) through slurry conversion. Two additional peroxosolvates were formed, from an *in situ* oxidation of compounds **4a** and **7a**, and denoted as compounds **4b** and **7b** (**Figure 2.3**). These findings demonstrate that a one-pot synthesis of *N*-oxide peroxosolvates using slurry conversion crystallization is viable and is competitive with peroxosolvate formation of the pyridine. Additionally, peroxosolvate formation was unsuccessful with compounds **3** and **6** due to challenges regarding instability and solubility in the presence of H_2O_2, respectively: see **2.4.2 General Methods: Peroxosolvate Crystallization of Compounds (1-8)** and **Table 2.1** for full details on crystallization conditions for compounds **1-8**.



4b **7b**

Figure 2.3. Structures of compounds **4b** and **7b**.

Table 2.1. Crystallization conditions for compounds **1-8**.

Compound	Peroxosolvate	Pyridyl Peroxosolvate Conditions	*N*-oxide Peroxosolvate Conditions
1	yes	9:1 by volume acetonitrile:98% hydrogen peroxide	
2	yes	1:1 by volume acetonitrile:98% hydrogen peroxide[a]	
3	no		
4a-b	yes	**4a-** 1:1 by volume acetonitrile:98% hydrogen peroxide	**4b-** 1:1 by volume acetonitrile:98% hydrogen peroxide
5	yes	1:1 by volume ethyl acetate:98% hydrogen peroxide	
6	no		
7a-b	yes	**7a-** 1:1 by volume ethyl acetate:98% hydrogen peroxide	**7b-** Pure 98% hydrogen peroxide
8	yes	1:1 by volume ethyl acetate:98% hydrogen peroxide	

[a]Mixture of hydrate and peroxosolvate.

Raman spectroscopy was used to identify peroxosolvate crystal phases (see **Figures 2.11-2.26** in the **Additional Figures** section for full Raman spectra). The peroxide O-O stretching vibrational frequency was used to indicate the presence H_2O_2 in the crystals grown. The O-O stretch for 98% H_2O_2 is observed at 877 cm^{-1} and it is expected that this peak will be shifted in formed peroxosolvates due to interactions between peroxide and the coformer. Observation of major peroxide O–O stretches (between 863 and 874 cm^{-1} as shown in **Table 2.2**) in the Raman spectra for compounds **1**, **2**, **4a-b, 5**, **7a-b** and **8** compared to the commercially available anhydrous forms provide evidence for peroxosolvate formation. All newly formed peroxosolvates (pyridyl and *N*-oxide) have red shifted peroxide O-O stretches compared to 98% H_2O_2. Shifts to lower

frequencies are reflected in the intermolecular interactions observed within the crystal structures obtained (vide infra).

Table 2.2. Major H_2O_2 (O-O) stretching vibrational frequency in cm^{-1} of each newly formed peroxosolvate and 98% H_2O_2.

Peroxosolvates and 98% H_2O_2	Peroxide O−O Stretch (cm^{-1})
1	871
2	874
4a	863
4b	867
5	864
7a	874
7b	868
8	872
H_2O_2	877

Crystal phases suspected to be peroxosolvates based on their Raman spectra were structurally characterized using SC-XRD (**Tables 2.4-2.7** in the **Additional Tables** section) with the exception of compounds **1** and **8**. The results from Raman spectra for the formation of peroxosolvate **1** were promising, though high-quality diffraction data were not obtained, and thus structural information was not evaluated. Similarly, a peroxosolvate of compound **8** was unable to be grown as single crystals; however, Raman spectra (**Figure 2.26** in the **Additional Figures** section) and PXRD patterns (**Figure 2.4**) suggest a new form distinct from that of the known hydrates (JEDKUZ[29], JEDKIN[29], and GASNIY[30]). In the case of compound **2**, a crystal structure of a mixed hydrate/peroxosolvate was obtained.

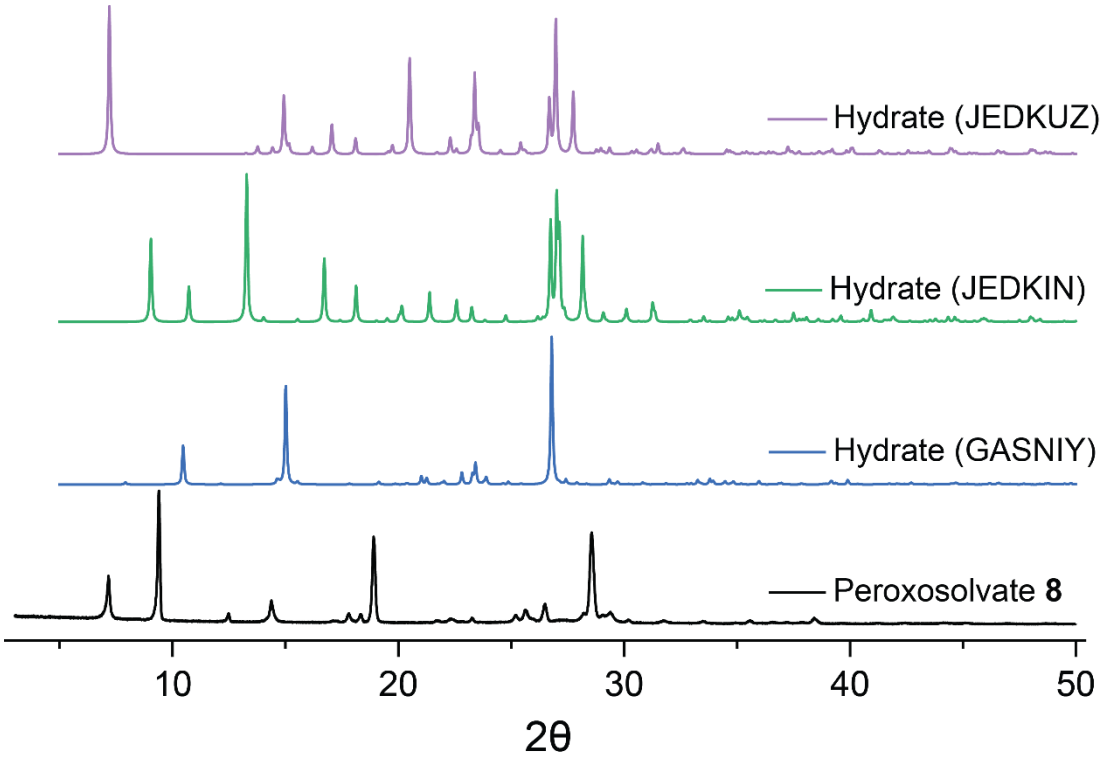


Figure 2.4. Powder pattern of the hydrates of compound **8** (BPU-purple, green, and blue) and peroxosolvate **8** (black).

^{31}P NMR spectroscopy was used to determine the H_2O_2/H_2O ratio in the material using the oxidation of triphenylphosphine to triphenylphosphine oxide (**Figure 2.5**).[31] These experiments show that the relative ratio of H_2O_2/H_2O is 1.76/1; a representative experiment found 5.69×10^{-5} mol H_2O_2 in the analysis of an 8.92×10^{-5} mol sample, calculated using the molecular weight of one formula unit of the peroxosolvate. Raman spectroscopy (**Figure 2.13** in the **Additional Figures** section) shows the peroxide O-O stretch of peroxosolvate **2** at 874 cm^{-1} with characteristic red shifting in comparison to 98% H_2O_2 and shifting in peaks that are unique to the commercially available compound; when compared to the powder patterns (**Figure 2.6**) of known hydrates (SAZXAS[32] and TAJRAX[33]), the pattern for peroxosolvate **2** show distinct differences in packing motif that suggest a new form has been obtained.

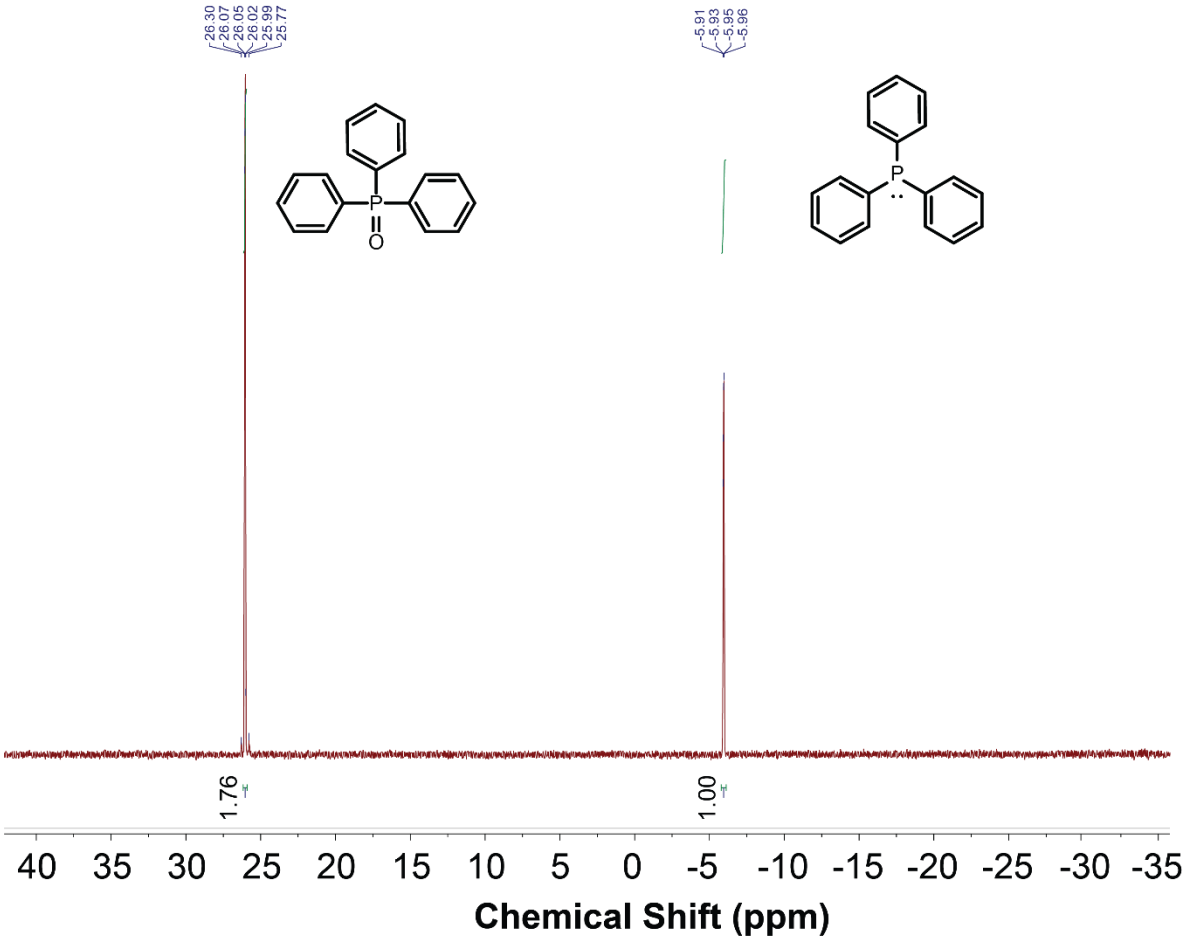


Figure 2.5. ^{31}P NMR spectra of hydrate/peroxosolvate mixture of compound **2** with triphenylphosphine oxidized to triphenylphosphine oxide, recorded at 25 °C.

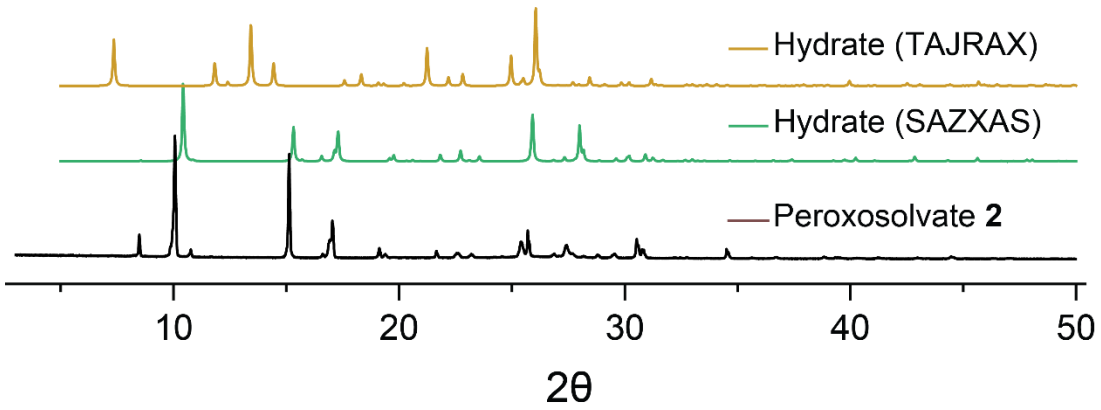


Figure 2.6. Powder patterns of two hydrates of compound **2** (gold and green) and peroxosolvate **2** (black).

Crystal structures of peroxosolvates were successfully obtained for compounds **2**, **4a-b**, **5**, and **7a-b**. Within each peroxosolvate structure, two hydrogen bonds are donated from H_2O_2 to the coformer. As shown by the histogram in **Figure 2.7**, the peroxosolvates (in structures without disorder) have hydrogen bond interaction distances that are shorter than the crystalline hydrates[34–41] (calculated as the distance between oxygen of water or H_2O_2 to the closest heteroatom of the pyridyl-group or *N*-oxide). Specifically, peroxosolvate structures **4a**-H_2O_2, **4b**-H_2O_2, and **5**-H_2O_2 exhibited shorter hydrogen bond interaction distances (between 2.662 and 2.785 Å) than what is found in the hydrates (between 2.727 and 2.883 Å) of compounds **4a**, **4b**, and **5**. See **Table 2.3** for full list of hydrogen bond interaction distances of hydrates and peroxosolvates. These findings are consistent with the stronger HB donation ability of H_2O_2 compared to water. The mixed hydrate/peroxosolvate of compound **2**, though disordered in the crystal structure, is isostructural to the hydrate with Ref code SAZXAS[32]. Another example of an isostructural hydrate and peroxosolvate pair is **4a**-H_2O (RAPRUW[34]) and **4a**-H_2O_2 (**Figure 2.8**).

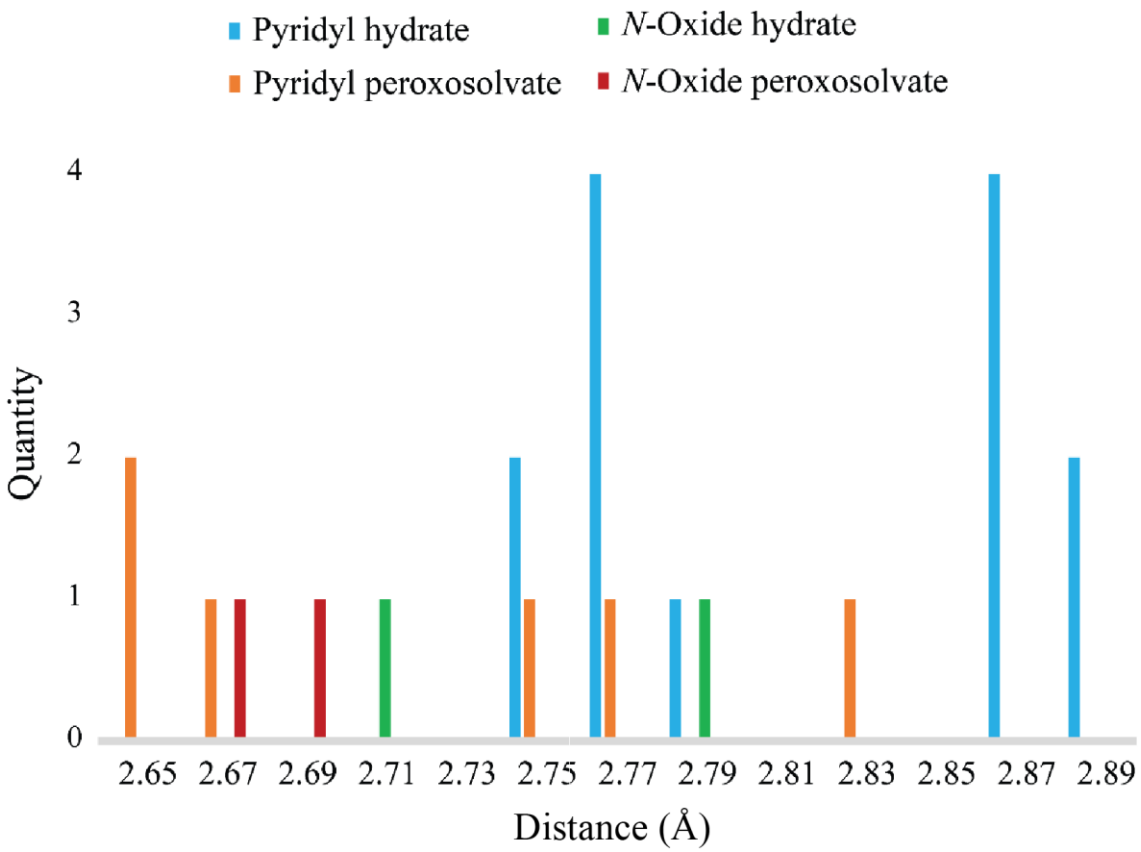
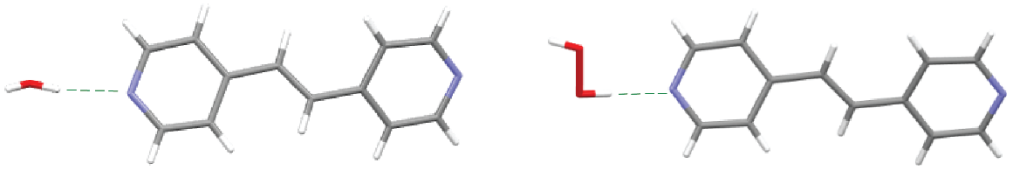


Figure 2.7. Histogram of the hydrogen bond interaction distances between water or H_2O_2 O to sp^2 N-pyridyl group or O-N (N-oxide) color coded as pyridyl hydrate (blue), pyridyl peroxosolvate (orange**)**, N-oxide hydrate (green), and N-oxide peroxosolvate (red).

Table 2.3. Hydrogen bond (HB) interaction distances (O···N or O···O-N) in the hydrate and peroxosolvate structures of compounds **4a-b**, **5**, and **7a-b**.

O···N hydrate HB interaction distance (Å)[a]	O···N peroxosolvate HB interaction distance (Å)[a]	O···O-N hydrate peroxosolvate HB interaction distance (Å)[b]	O···O-N peroxosolvate HB distance interaction(Å)[b]
(RAPRUW)[34] **4a**-H_2O monohydrate: 2.875, 2.898 (RAPRUW01)[35] **4a**-H_2O monohydrate: 2.876, 2.895	**4a**-H_2O_2 1:1: 2.765, 2.785	(ITEWOT)[40] **4b**-H_2O pentahydrate**:** 2.727, 2.800 (ITEWOT01)[41] **4b**-H_2O pentahydrate**:** 2.759, 2.824	**4b**-H_2O_2 1:1: 2.686, 2.686
(WECGUI)[36] **5**-H_2O hemihydrate: 2.883, 2.883 (WECHAP)[36] **5**-H_2O hydrate: 2.793	**5**-H_2O_2 1:1.5: (2.662, 2.662;)[c]		
(HUGMEB)[37] **7a**-H_2O hemihydrate: 2.775, 2.775 (HUGMEB01)[38] **7a**-H_2O hemihydrate: 2.769, 2.769 (HUGMEB02)[39] **7a**-H_2O hemihydrate: 2.774, 2.774	**7a**-H_2O_2 (2.673, 2.845)[c]		**7b**-H_2O_2 1:1: 2.696

[a]HB interaction distance between water or H_2O_2 and the pyridyl-group or [b]*N*-oxide-group containing compounds (O···N or O···O-N) are shown in bold. Each (relevant) known hydrate (along with the Ref code associated) and new peroxosolvate are named #-H_2O or #-H_2O_2, respectively. [c] Some disorder in the structure, and the listed HB interactions distances are for ordered perosoxolvate molecules in the structure.



4a-H_2O **4a**-H_2O_2

Figure 2.8. Illustration of the interactions of water in the hydrate (pyridyl or **4a**-H_2O) and hydrogen peroxide in the peroxosolvate (**4a**-H_2O_2) of compound **4a.**

Crystal packing modes within most of the formed peroxosolvates are similar given that hydrogen bond donation is only observed with H_2O_2 to a pyridyl or *N*-oxide-group. The exceptions are with **5**-H_2O_2, **7a**-H_2O_2, and **7b**-H_2O_2 (**Figures 2.9** and **2.10**, respectively), which have sulfonyl-groups, that also act as HB acceptors to H_2O_2; specifically, for **7a**-H_2O_2, this differs from the hydrate structures[37–39] where the sulfonyl-group does not HB with water in the crystal lattice. **7b**-H_2O_2 forms one unique type of hydrogen bonding interaction where a H_2O_2 molecule bridges one *N*-oxide-group to a sulfonyl-group of an adjacent molecule. In the one 1:1.5 pyridyl-H_2O_2 crystal structure, **5**-H_2O_2 forms two unique types of hydrogen bonding interactions: 1) H_2O_2 molecule bridging two methylated pyridyl-groups of adjacent molecules and 2) H_2O_2 to a sulfonyl-group. Similar to **5**-H_2O_2, in hydrate **5**-H_2O (WECHAP[36]), one H_2O molecule bridges one methylated pyridyl-group to a sulfonyl-group of an adjacent molecule. In contrast, hemihydrate **5**-H_2O (WECGUI[36]) does not form the sulfonyl-group interaction found in the **5**-H_2O_2. This difference in sulfonyl-group interactions between the hydrates, pyridyl and/or *N*-oxide peroxosolvates of compounds **5** and **6** can be observed under these conditions: 1) molecule contains more than one type of strong HB acceptor and 2) stoichiometric ratio of coformer to solvent (i.e. water or H_2O_2) is less than 2:1. In the two 1:1 pyridyl peroxosolvate and hydrate structures, **4a**-H_2O_2 and **4a**-H_2O both form linear chains in a herringbone packing motif without π-π overlap of the faces between the adjacent molecules. For

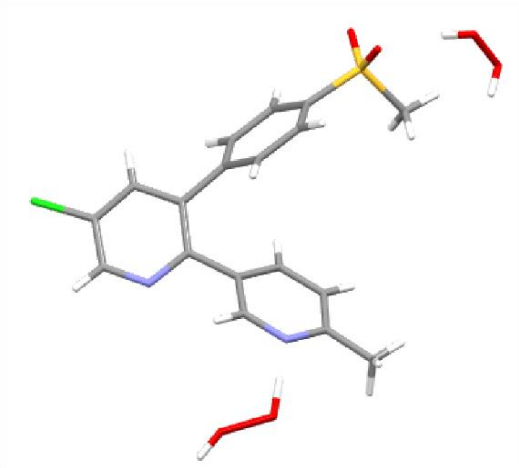


Figure 2.9. Illustration of the interactions that occur between both the pyridyl-group and sulfonyl-group with H_2O_2 in **5**-H_2O_2 (one conformer shown).

4a-H_2O_2 there are closer edge-to-face interactions of adjacent molecules that contribute to crystal packing than in **4a**-H_2O.

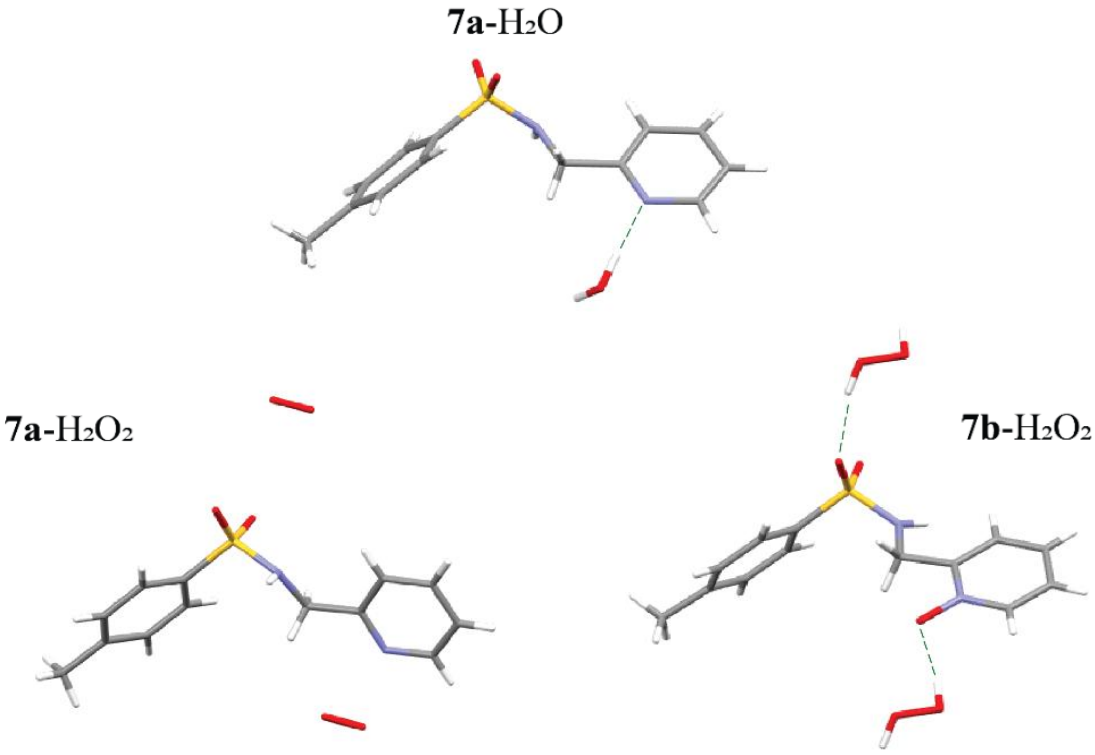


Figure 2.10. Illustration of the interactions of water in the hydrate (**7a**-H_2O, HUGMEB), hydrogen peroxide in the peroxosolvate (**7a**-H_2O_2, one conformer shown), and hydrogen peroxide in the N-oxide peroxosolvate (**7b**-H_2O_2) of compound **7a**.

2.3 Conclusion

Eight newly synthesized peroxosolvates are presented in this work. The new peroxosolvates that were structurally characterized (without disorder) have significantly shorter hydrogen bonding interaction distances than their corresponding hydrates. The cases where both pyridyl and *N*-oxide peroxosolvates were formed represent a critical aspect of donor and acceptor synthon compatibility given that the reactivity of the pyridyl-group and HB donor strength as well as oxidizing ability of H_2O_2, together, play a major role in interaction propensity. Moreover, evaluation of the kinetics behind the reactivity of pyridine derivatives with various degrees of

electronic activation in the presence of highly concentrated H_2O_2 could provide more detailed parameters for coformer selection criteria when using the CSD to identify potential peroxosolvate formers. Given the need to improve oxygen balance of energetic materials and solubility of pharmaceuticals, a major contribution of this work includes successfully demonstrating how peroxosolvates of sp^2-hybridized pyridyl-group containing compound can be obtained through careful consideration of coformer criteria applied to the existing structural data.

2.4 Methods

Caution! H_2O_2 is a strong oxidizing reagent. Proper personal protective equipment was utilized to prevent personnel exposure. Be advised that health hazards due to exposure that may occur include eyes, nose, throat, and skin irritation (e.g., burns).

2.4.1 Materials and Reagents.

2,4,6-Tris(2-pyridyl)-*s*-triazine (**1**, MilliporeSigma, ≥99%), 2,9-dimethyl-1,10-phenanthroline (**2**, Alfa Aesar, ≥98%), 9-aminoacridine (**3**, MilliporeSigma, ≥97%), 1,2-di(4-pyridyl)ethylene (**4a**, MilliporeSimga, ≥97%), 5-chloro-3-[4-(methylsulfonyl)phenyl]-2-(2-methyl-5-pyridinyl)pyridine (**5**, ASTATECH, 99% Pure), 2-amino-7,7-dimethyl-5-oxo-4-pyridin-4-yl-5,6,7,8-4h-4h-chromene-3-carbonitrile (**6**, MilliporeSigma), 4-methyl-N-(2-pyridinylmethyl)benzenesulfonamide (**7a**, MilliporeSigma), N,N'-bis(3-pyridyl)urea (**8**, Toronto Research Chemicals) were purchased and used as received. 98% H_2O_2 w/w in water was obtained from Peroxychem and used as received. Acetonitrile (ACN), methylene chloride (DCM), and ethyl acetate (EtOAc) were obtained from Fisher Scientific and dried over 0.3 nm molecular sieves.

2.4.2 General Methods: Peroxosolvate Crystallization of Compounds (1-8)

A small amount of solvent (2-100 μL 98% H_2O_2, 1:1 by volume ACN/98% H_2O_2, 1:1 by volume DCM/ 98% H_2O_2, or 1:1 by volume EtOAc/98% H_2O_2) were added to the compound to form a slurry in a glass 2 mL vial with a polypropylene lid and PTFE gasket or 8 mm round bottom crimp vial (6 × 32mm) with crimp top seal (8 mm). Samples were shaken on an IKA® VIBRAX VXR basic shaker at 100 rpm from several minutes to several days and monitored via optical microscopy for visual confirmation of new crystal growth. The instrumentation tools used to characterize the new crystalline materials are provided in the **Experimental Setup** section.

2.4.3 Raman Spectroscopy

Raman spectra were collected using a Renishaw inVia Raman spectrophotometer featuring a Leica microscope, a 785 nm laser, 1200 lines/mm grating, a RenCam CCD area detector, and 65 μm slit size. Spectra were collected in extended scan mode from 100-2500 cm^{-1} and analyzed using the WiRE 5.3.2 software package (Renishaw).

2.4.4 ^{31}P NMR

^{31}P NMR measurements were performed using a Varian vnmrs 500 MHz spectrometer using 128 scans and a 25 s relaxation delay. Acetonitrile-d_3 was used for locking and shimming. Mixed hydrate/peroxosolvate of compound **2** (7.20 mg, 2.97 × 10^{-5} mol) and triphenylphosphine (23.40 mg, 8.92 × 10^{-5} mol) were dissolved in 2.00 mL dry acetonitrile then placed on a shaker for 1 hour to react. A standard triphenylphosphine solution (23.40 mg, 8.92 x 10^{-5} mol) in dry acetonitrile (2.00 mL) was prepared, using the same conditions as previously mentioned, and analyzed as a reference peak to confirm the absence of oxidized material in the reagent. The ratio

of triphenylphosphine-to-triphenylphosphine oxide for each spectrum (**Figure 2.5**) was calculated by the integration of the peaks using the software MestReNova v12.0.0-20080, Mestrelab Research, 2017.

2.4.5 Single-Crystal X-ray Diffraction (SC-XRD)

SC-XRD data were collected using a Rigaku XtaLAB Synergy-S X-ray diffractometer in a κ goniometer geometry configuration. The diffractometer was equipped with a low temperature device and a PhotonJet-S microfocus Cu source (λ = 1.54187 Å) operated at 50 kV and 1 mA. The X-ray intensities were measured at room temperature (see **Tables 2.4-2.7**) with a HyPix-6000HE detector which was held 34.00 mm from the sample. The data were processed with CrysAlisPro v38.46 (Rigaku Oxford Diffraction) and were corrected for absorption. The structures were solved in OLEX2[42] using SHELXT[43] and refined using SHELXL[44]. More details on crystal structures can be found in **Tables 2.4-2.7** in the **Additional Tables** section and in the files deposited within the CSD (2175873-2175878).

2.4.6 Powder X-ray Diffraction (PXRD)

PXRD data were collected using a Panalytical Empyrean system utilizing Cu Kα radiation (λ = 1.54187 Å) and operating at 45 kV and 40 mA. The Panalytical Empyrean system uses a Bragg–Brentano HD X-ray optic and an X'Celerator Scientific detector operating in a continuous 1D scan mode. Scans were conducted according to the following parameters: 2θ = 3–50°, step size 0.008°, and step speed 19.685 s. The data were worked up using Origin 2020b. Powder patterns are illustrated in **Figures 2.4** and **2.6**.

2.4.7 Experimental Setup

Experimental crystallization conditions used to obtain the crystals characterized via Raman spectroscopy, SC-XRD, ^{31}P NMR, and PXRD are described in **2.4.2 General Methods: Peroxosolvate Crystallization of Compounds (1-8)**. Mercury 2020.2.0 software was used to compare the previously reported crystalline hydrates of the 8 target compounds to newly synthesized peroxosolvates, as applicable.

2.5 Additional Figures

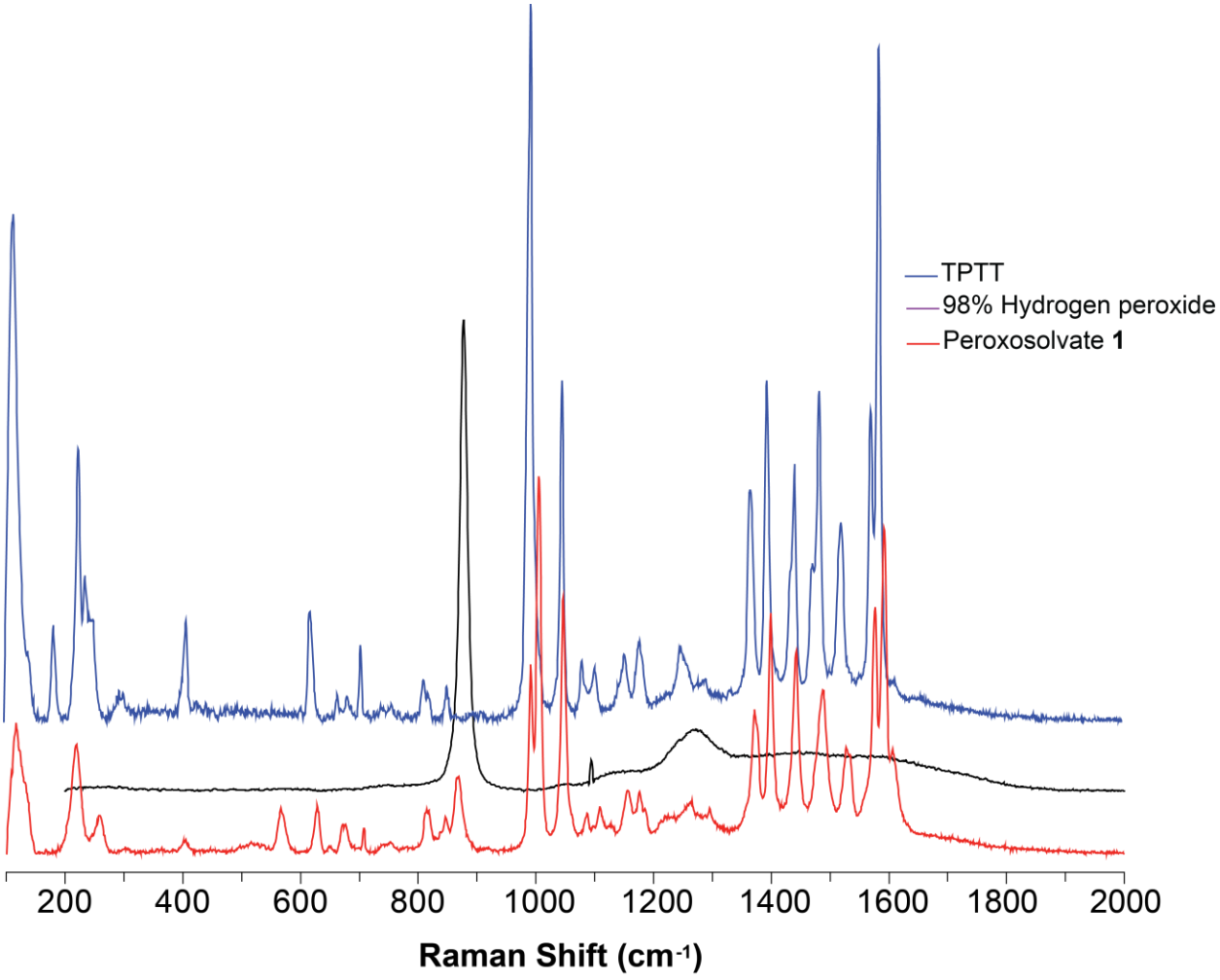


Figure 2.11. Full range (100-2000 cm^{-1}). Stacked Raman spectra of compound **1** (TPTT-blue), 98% hydrogen peroxide (black), and peroxosolvate **1** (red).

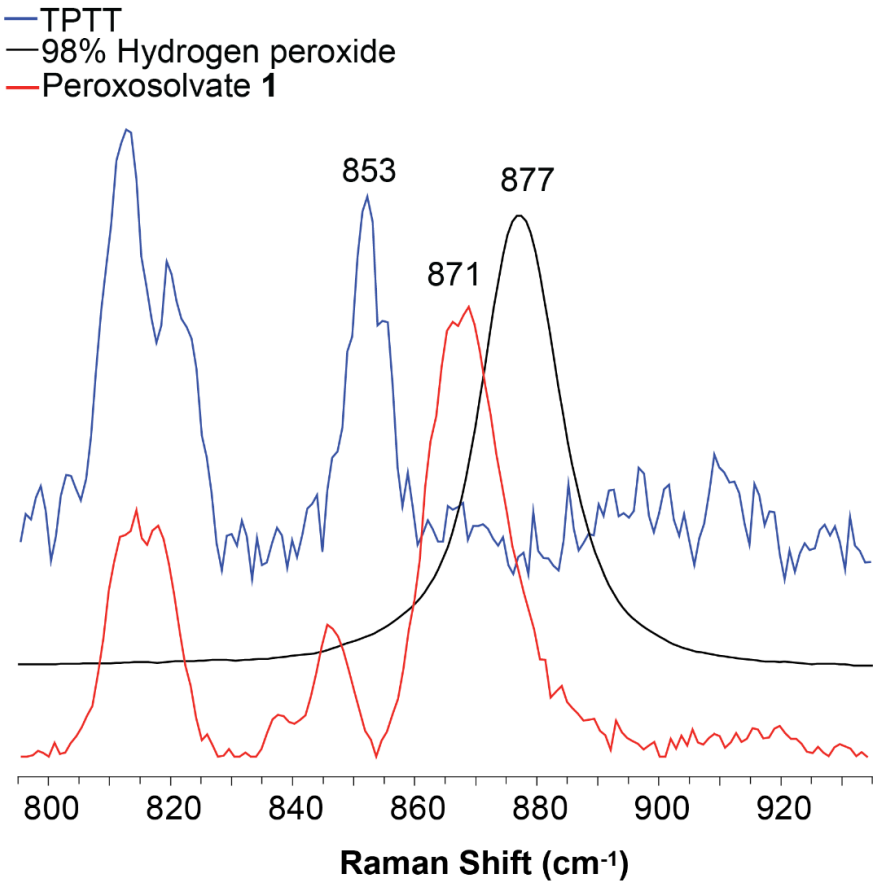


Figure 2.12. Zoomed in, stacked Raman spectra (795-935 cm^{-1}) of compound **1** (TPTT-blue), 98% hydrogen peroxide (black), and peroxosolvate **1** (red).

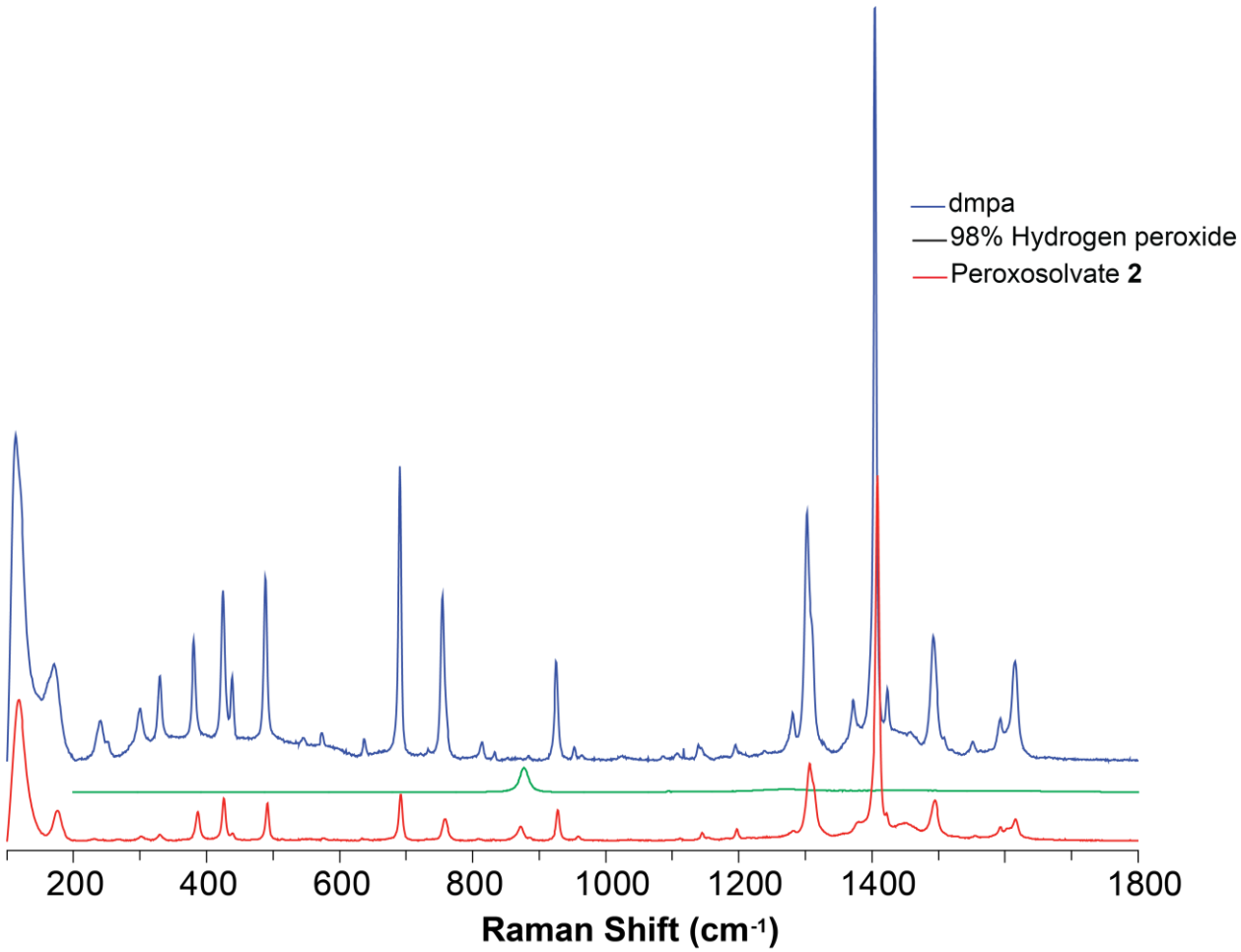


Figure 2.13. Full range (100-1800 cm^{-1}). Stacked Raman spectra of compound **2** (dmpa-blue), 98% hydrogen peroxide (green), and peroxosolvate **2** (red).

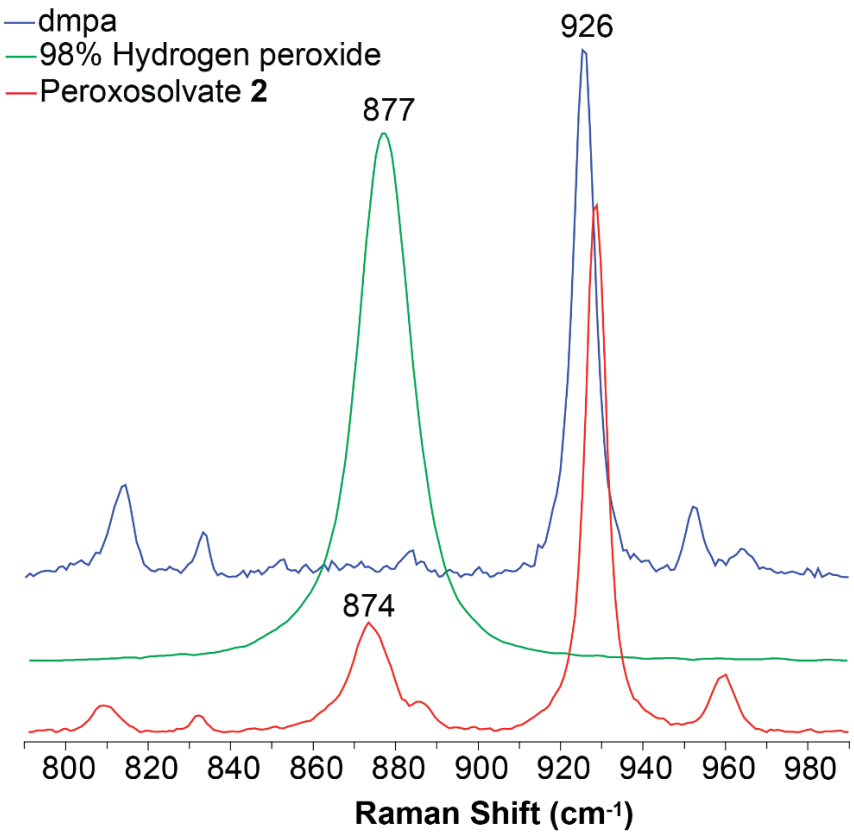


Figure 2.14. Zoomed in, stacked Raman spectra (790-990 cm^{-1}) of compound **2** (dmpa-blue), 98% hydrogen peroxide (green), and peroxosolvate **2** (red).

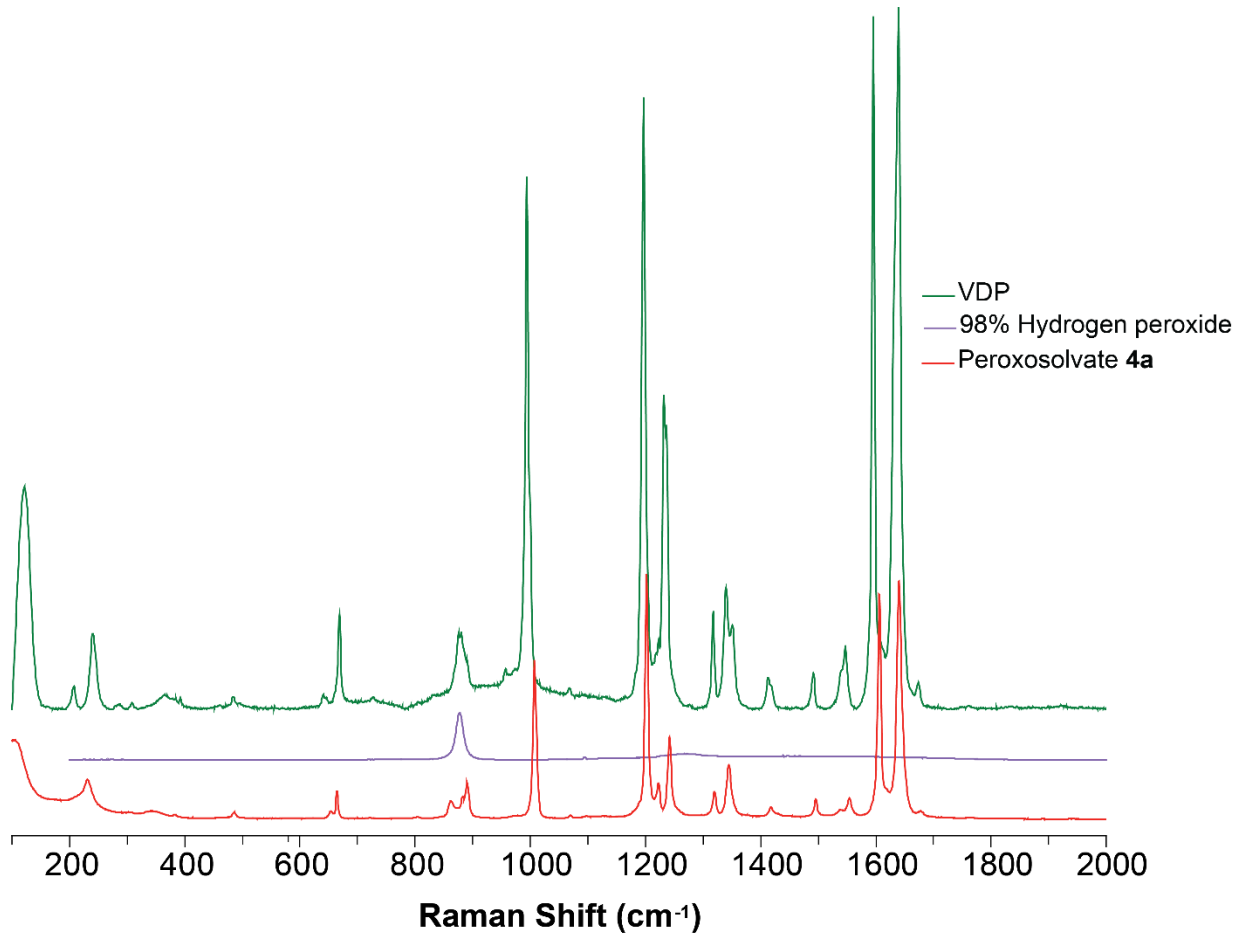


Figure 2.15. Full range (100-2000 cm^{-1}). Stacked Raman spectra of compound **4a** (VDP-green), 98% hydrogen peroxide (purple), and peroxosolvate **4a** (red).

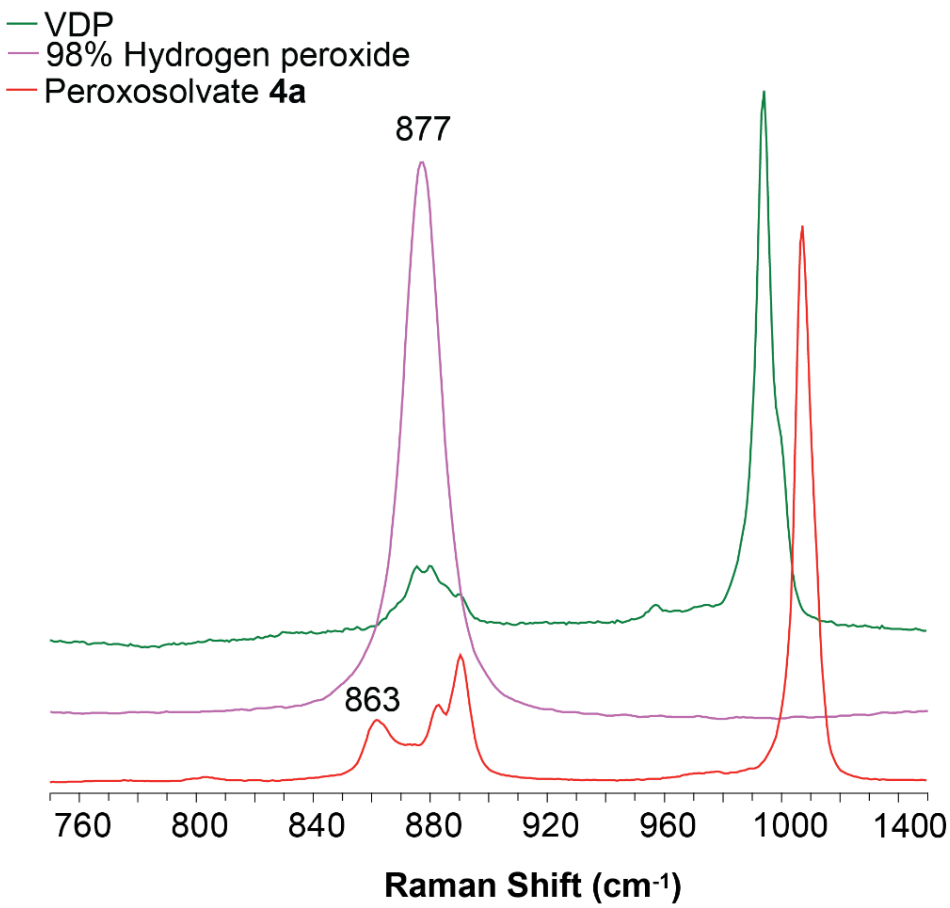


Figure 2.16. Zoomed in, stacked Raman spectra (750-1500 cm^{-1}) of compound **4a** (VDP-green), 98% hydrogen peroxide (black), and peroxosolvate **4a** (red).

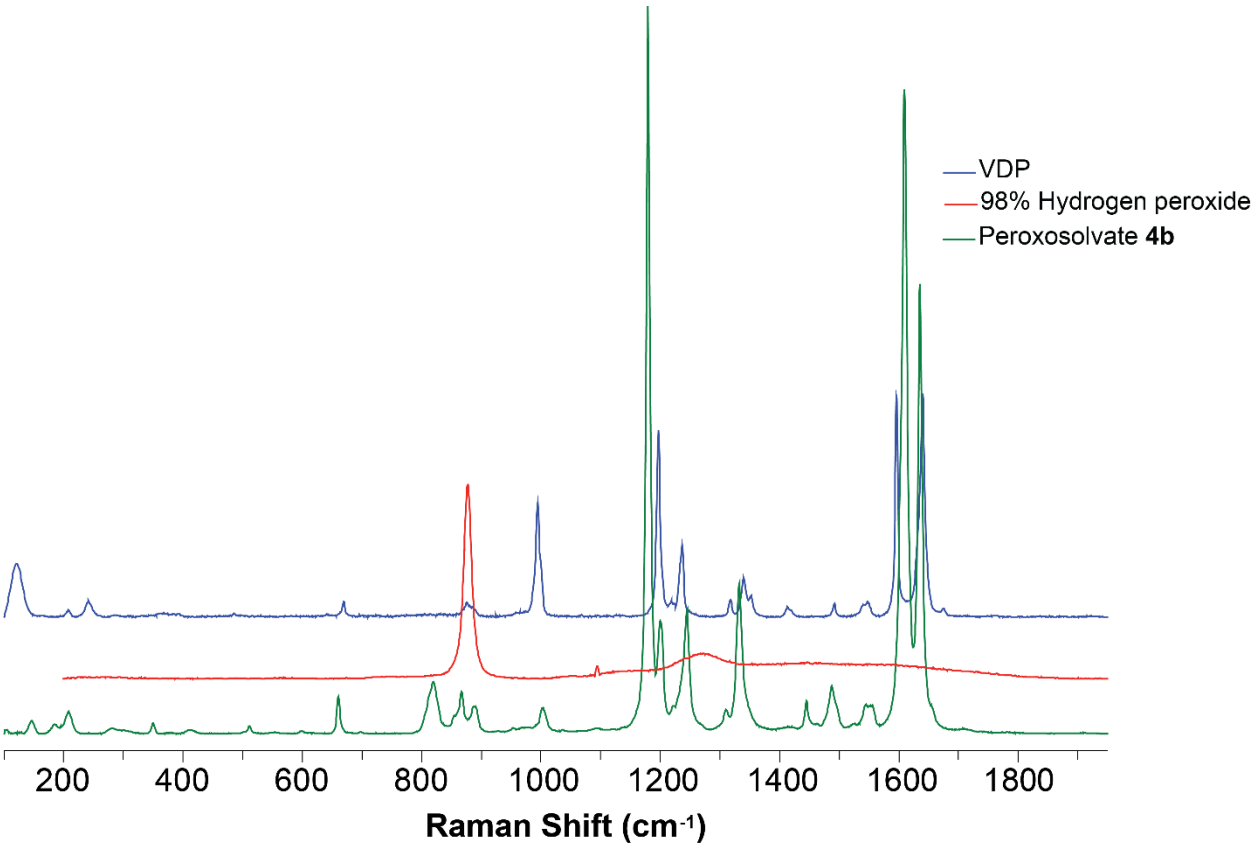


Figure 2.17. Full range (100-1900 cm^{-1}). Stacked Raman spectra of compound **4a** (VDP-blue), 98% hydrogen peroxide (red), and peroxosolvate **4b** (green).

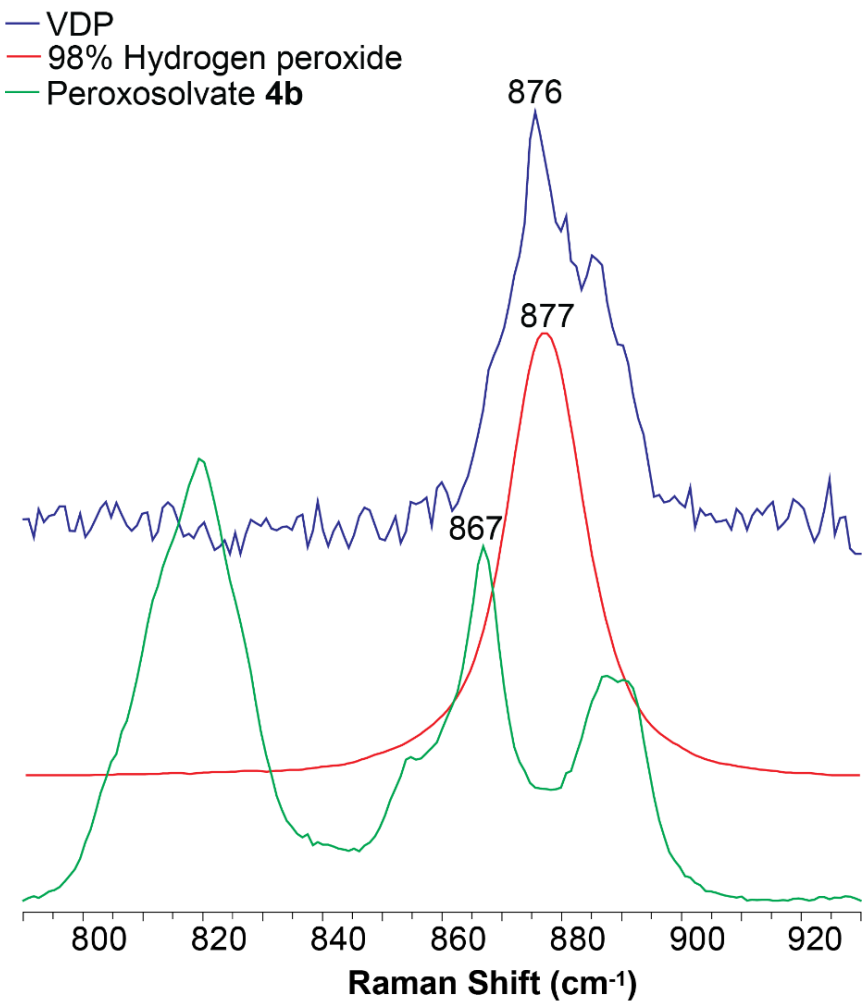


Figure 2.18. Zoomed in, stacked Raman spectra (790-930 cm^{-1}) of compound **4a** (VDP-blue), 98% hydrogen peroxide (red), and peroxosolvate **4b** (green).

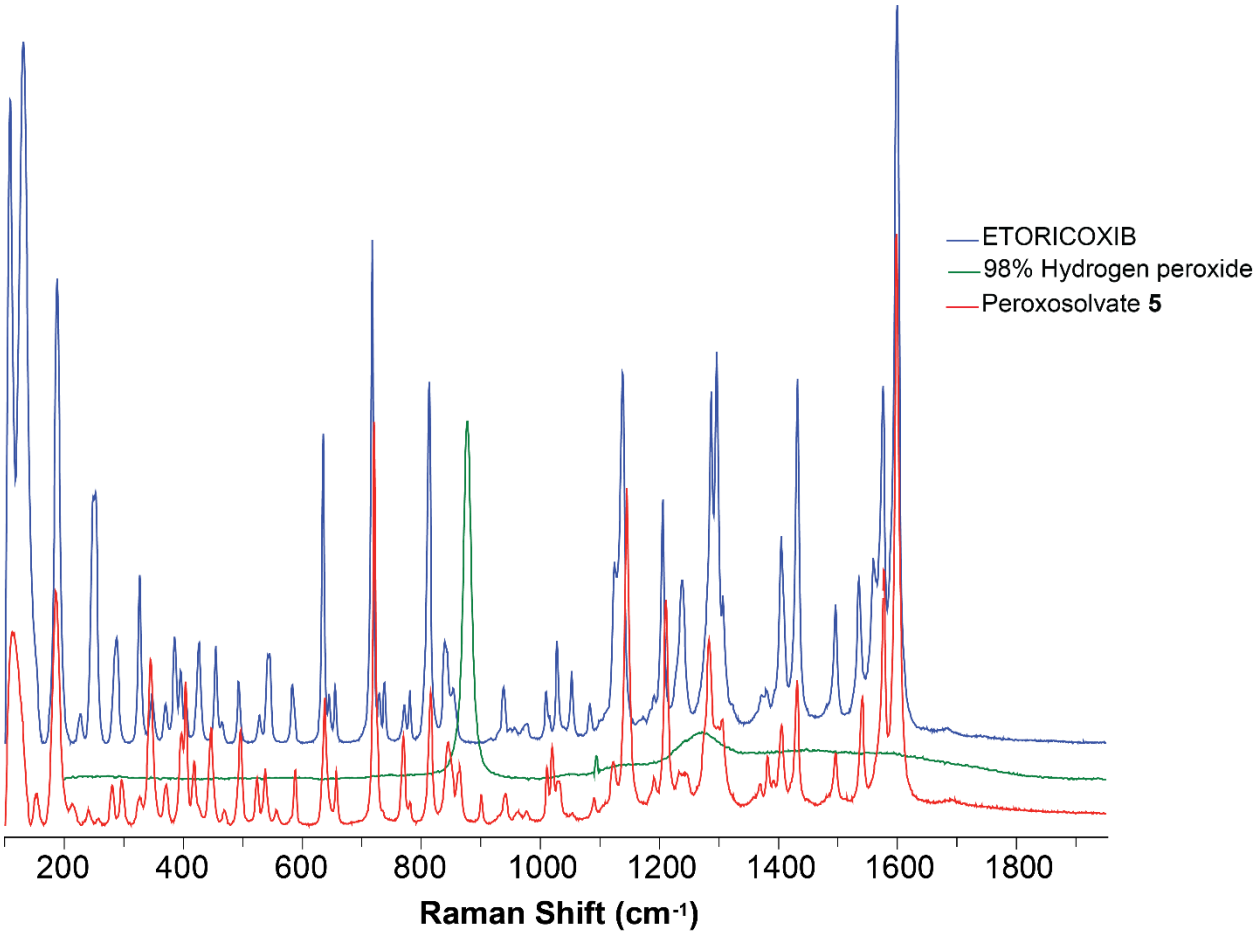


Figure 2.19. Full range (100-1940 cm^{-1}). Stacked Raman spectra of compound **5** (ETORICOXIB-blue), 98% hydrogen peroxide (green), and peroxosolvate **5** (red).

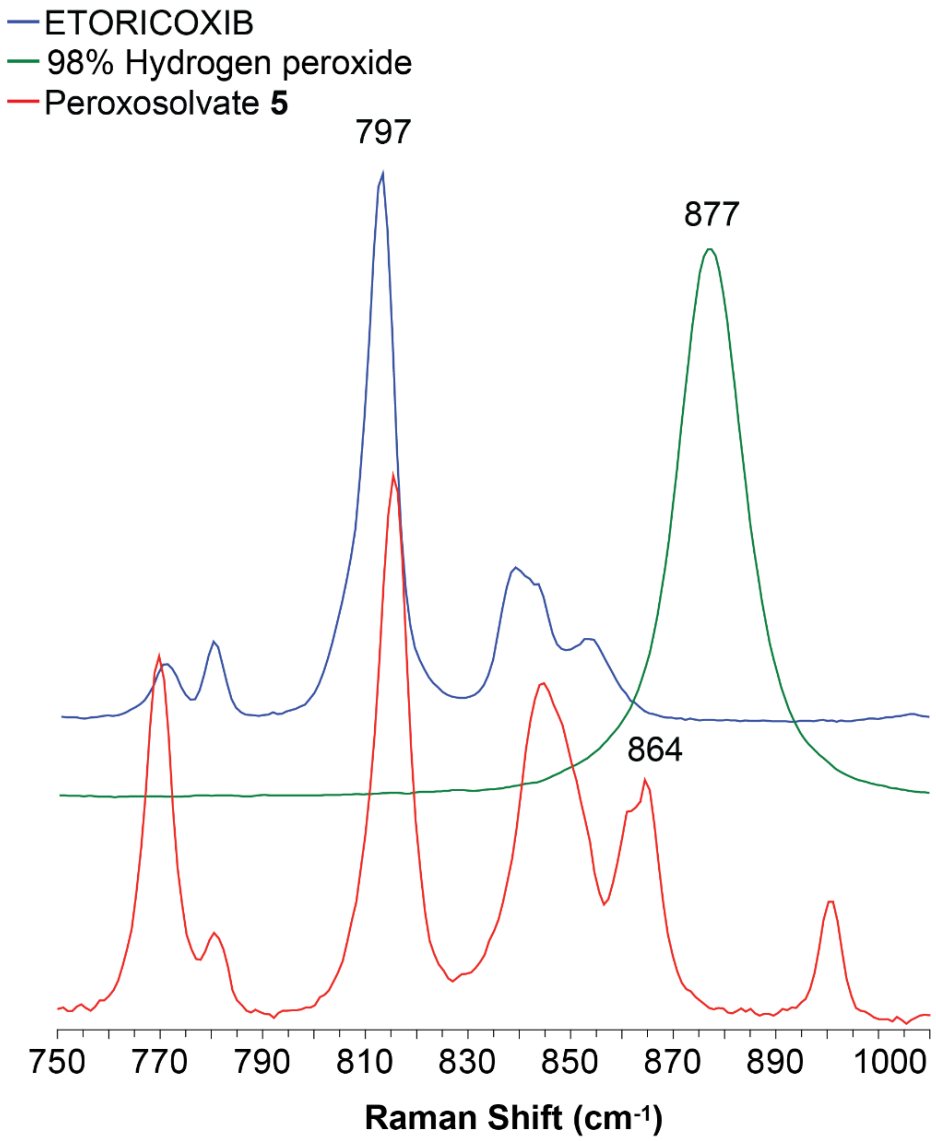


Figure 2.20. Zoomed in, stacked Raman spectra (750-1200 cm^{-1}) of compound **5** (ETORICOXIB-blue), 98% hydrogen peroxide (green), and peroxosolvate **5** (red).

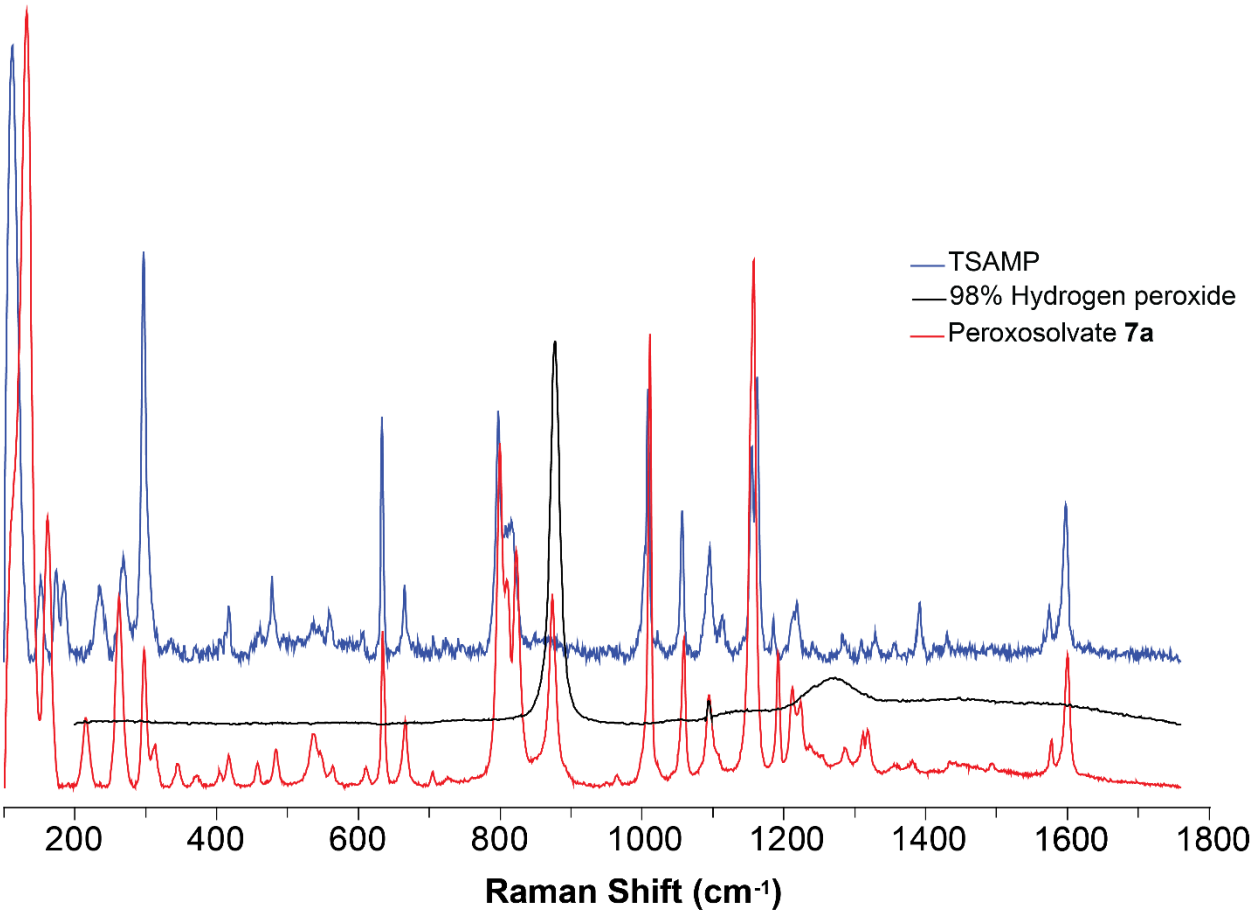


Figure 2.21. Full range (100-1760 cm^{-1}). Stacked Raman spectra of compound **7a** (TSAMP-blue), 98% hydrogen peroxide (black), and peroxosolvate **7a** (red).

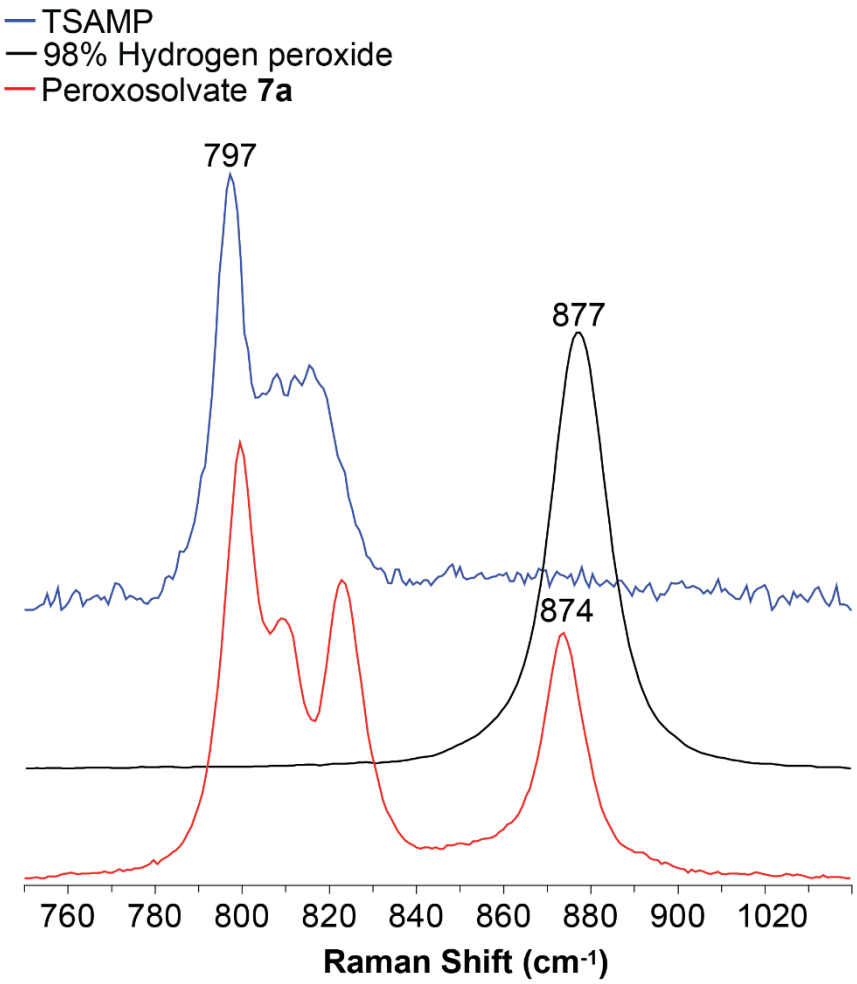


Figure 2.22. Zoomed in, stacked Raman spectra (750-1040 cm^{-1}) of compound **7a** (TSAMP-blue), 98% hydrogen peroxide (black), and peroxosolvate **7a** (red).

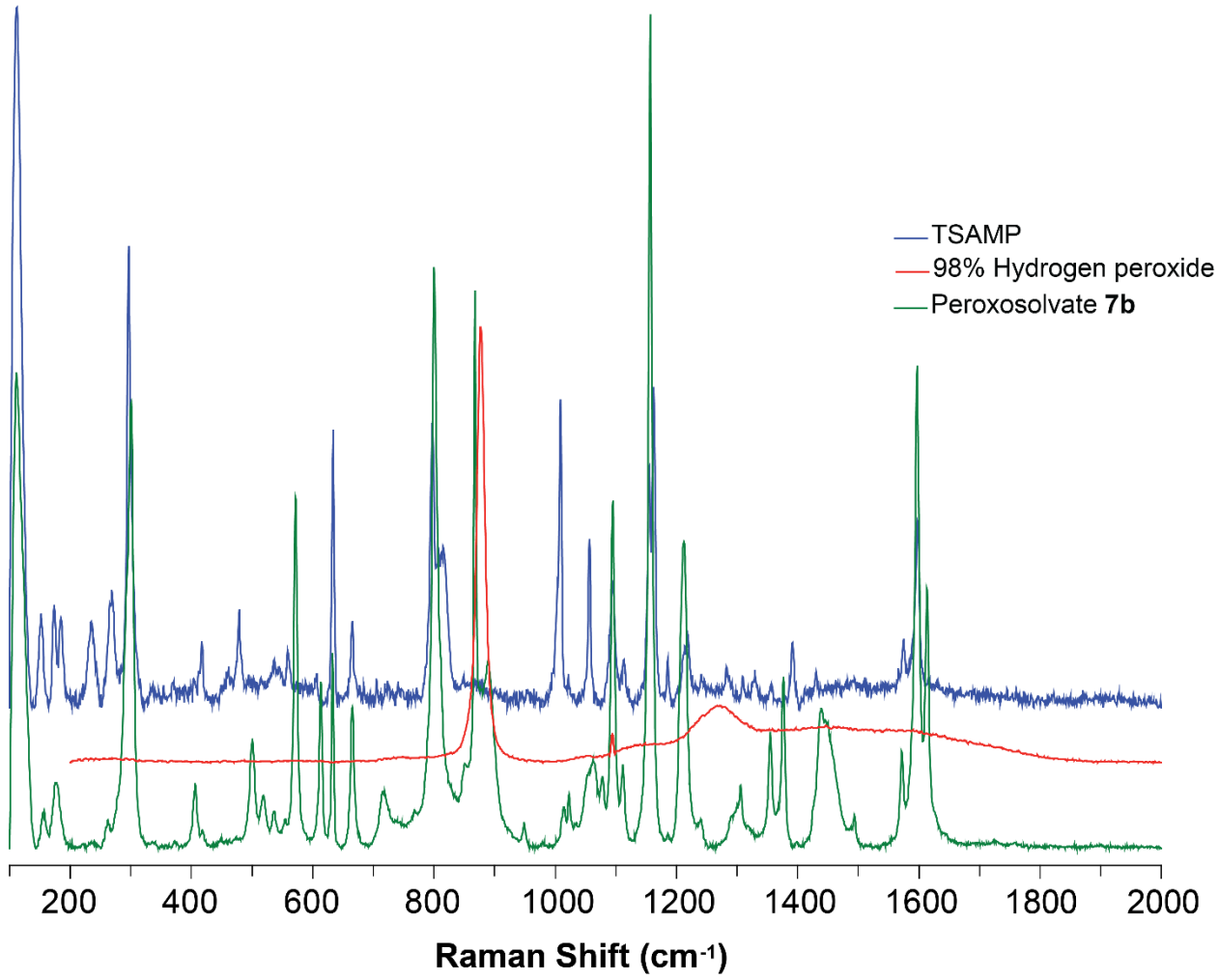


Figure 2.23. Full range (100-2000 cm^{-1}). Stacked Raman spectra of compound **7a** (TSAMP-blue), 98% hydrogen peroxide (red), and peroxosolvate **7b** (green).

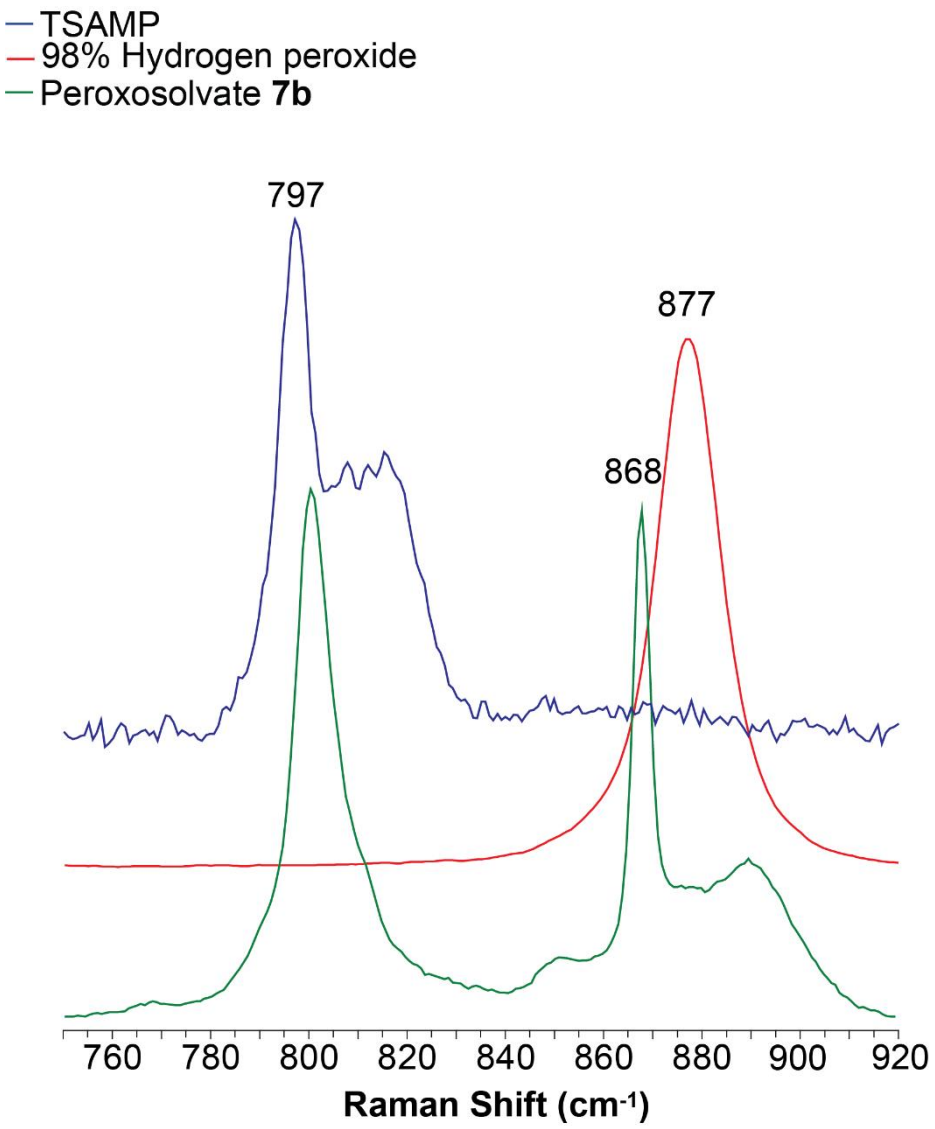


Figure 2.24. Zoomed in, stacked Raman spectra (750-920 cm^{-1}) of compound **7a** (TSAMP, blue), 98% hydrogen peroxide (red), and peroxosolvate **7b** (green).

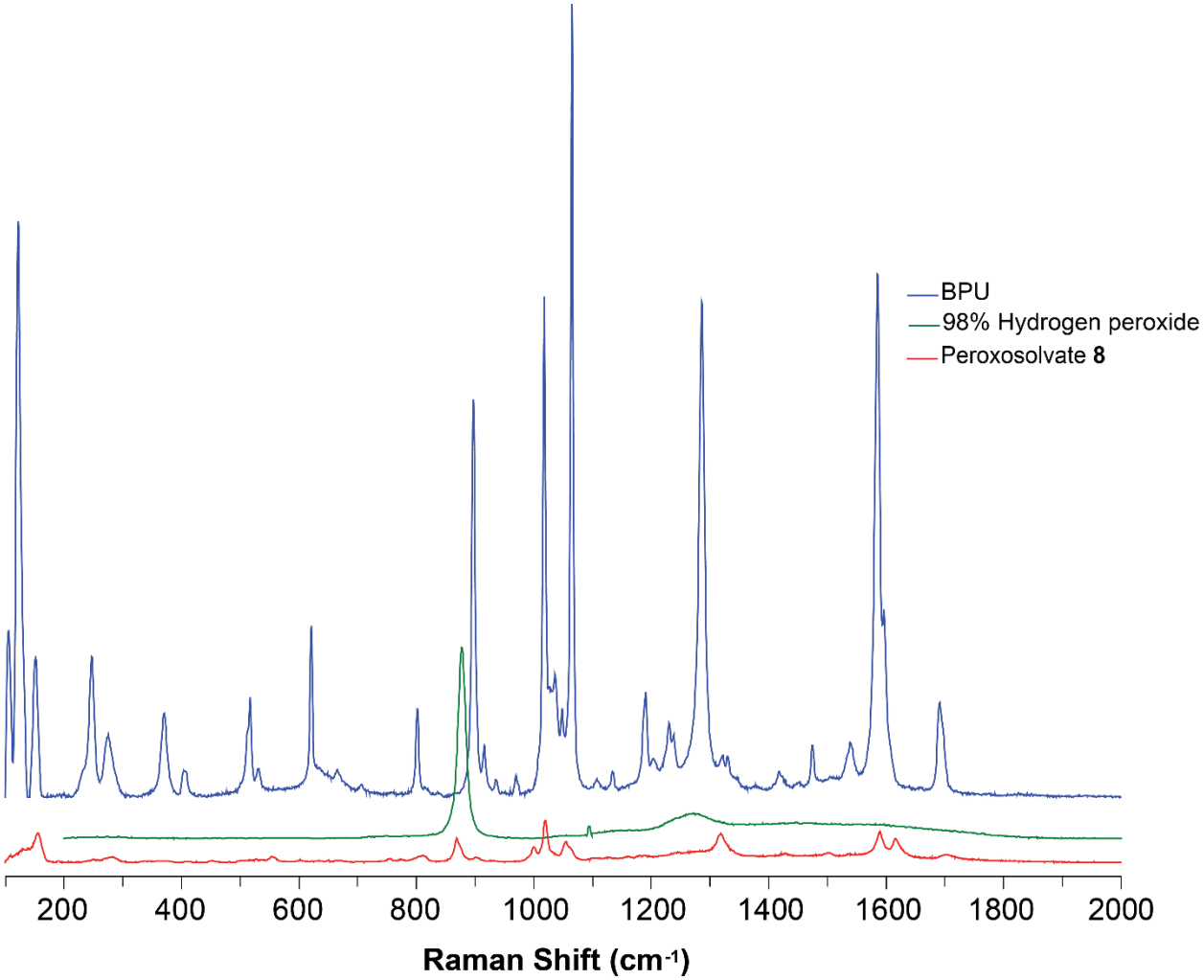


Figure 2.25. Full range (100-2000 cm^{-1}). Stacked Raman spectra of compound **8** (BPU-blue), 98% hydrogen peroxide (green), and peroxosolvate **8** (red).

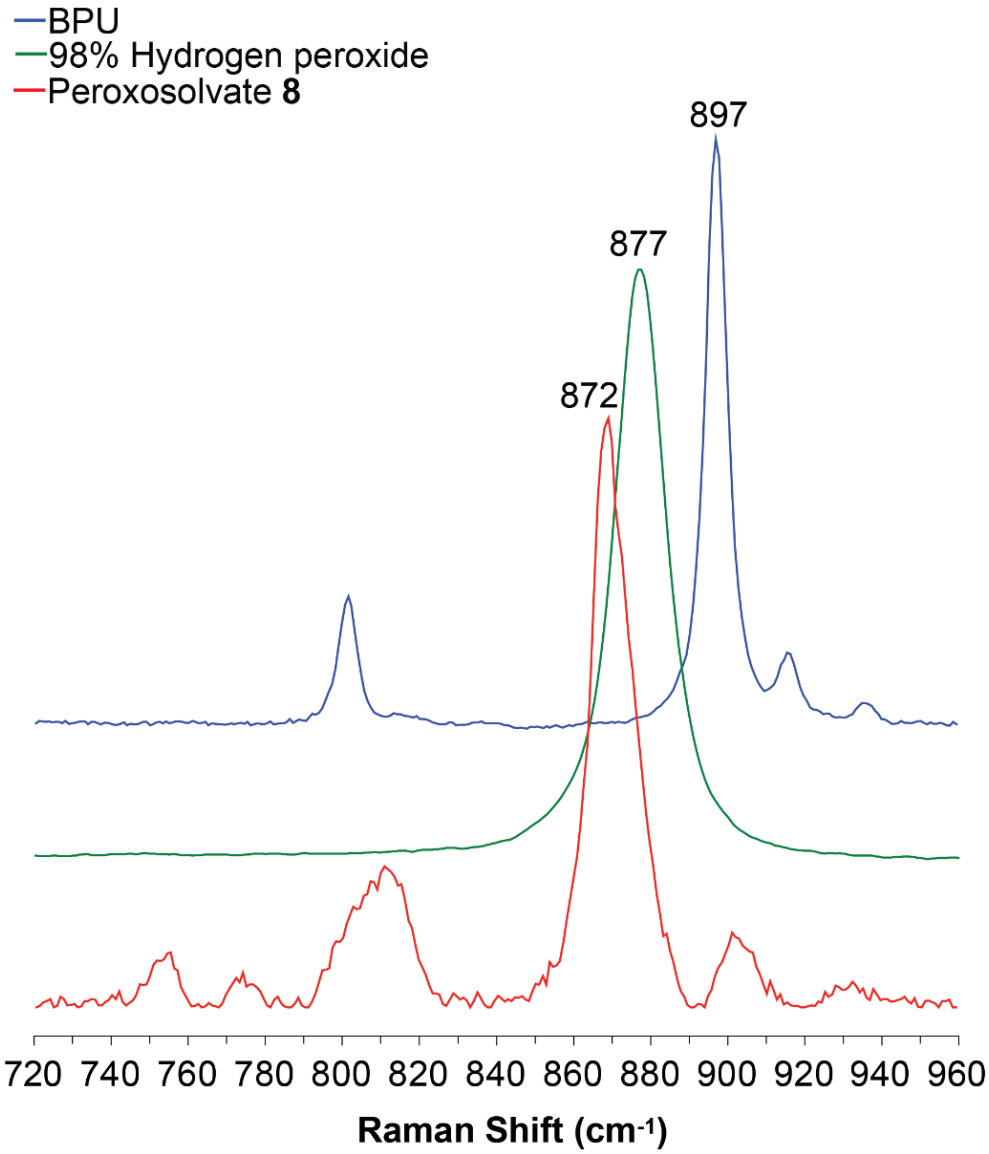


Figure 2.26. Zoomed in, stacked Raman spectra (720-960 cm^{-1}) of compound **8** (BPU-blue), 98% hydrogen peroxide (green), and peroxosolvate **8** (red).

2.6 Additional Tables

Table 2.4. Crystallographic data for peroxosolvates and previously published (relevant) hydrates of compound **2**.

Structural Information	**Hydrate (SAZXAS)**[32]	**Peroxosolvate (2)**
Space Group	C 2/m	I 2/m
Stoichiometry (compound:solvent)	Dihydrate	1:1
a (Å)	18.155(5)	11.02249(18)
b (Å)	6.871(2)	6.98644(11)
c (Å)	11.077(3)	18.1242(3)
α (°)	90	90
β (°)	110.96(2)	105.1257(16)
γ (°)	90	90
Volume ($Å^3$)	1290.35	1347.35
Z	4	4
R-Factor (%)	4.70	5.44
Temperature (K)	283-303	293
Density	1.258	1.278
R_1/wR_2	4.70 (some disorder)	5.44 (some disorder)

Table 2.5. Crystallographic data for peroxosolvates and previously published (relevant) hydrates of compounds **4a** and **b**.

Structural Information	**Hydrate (RAPRUW)**[34]	**Hydrate (ITEWOT)**[40]	**Peroxosolvate (4a)**	**Peroxosolvate (4b)**
Space Group	P n a 2_1	P b c n	P n a 2_1	P 2_1/c
Stoichiometry (compound:solvent)	Mono-hydrate	Penta-hydrate	1:1	1:1
a (Å)	9.1778(18)	11.9300(8)	9.9546(3)	4.8322(3)
b (Å)	14.768(3)	7.2004(5)	14.9417(4)	10.9821(5)
c (Å)	7.6109(15)	17.2426(12)	7.14621(18)	10.7744(4)
α (°)	90	90	90	90
β (°)	90	90	90	99.801(4)
γ (°)	90	90	90	90
Volume (Å^3)	1031.56	1481.15	1062.92	563.428
Z	4	4	4	2
R-Factor (%)	3.62	3.92	2.75	5.18
Temperature (K)	100	90	283-303	293-303
Density	1.289	1.365	1.351	1.463
R_1/wR_2	3.62	3.92	2.75	5.18

Table 2.6. Crystallographic data for peroxosolvates and previously published (relevant) hydrates of compound **5**.

Structural Information	**Hydrate (WECHAP)**[36]	**Peroxosolvate (5)**
Space Group	P21/c	P2/c
Stoichiometry (compound:solvent)	Hydrate	1:1.5
a (Å)	10.889(2)	13.5348(4)
b (Å)	12.359(3)	10.0394(3)
c (Å)	12.803(3)	14.6286(5)
α (°)	90	90(4)
β (°)	93.496(7)	110.940(4)
γ (°)	90	90
Volume ($Å^3$)	1719.78	1856.47
Z	4	4
R-Factor (%)	4.70	6.00
Temperature (K)	150	283-303
Density	1.434	1.470
R_1/wR_2	4.70	6.00 (some disorder)

Table 2.7. Crystallographic data for peroxosolvates and previously published (relevant) hydrates of compounds **7a** and **b**.

Structural Information	**Hydrate (HUGMEB)**[37]	**Peroxosolvate (7a)**	**Peroxosolvate (7b)**
Space Group	C 2/c	P1	P 2_1/c
Stoichiometry (compound:solvent)	Hemihydrate	1:2	1:1
a (Å)	27.145(11)	6.25200(10)	8.3442(2)
b (Å)	6.012(1)	7.8465(2)	5.80505(18)
c (Å)	16.690(7)	15.1735(3)	30.0995(8)
α (°)	90	94.033(2)	90
β (°)	99.10(2)	92.061(2)	96.489(3)
γ (°)	90	103.135(2)	90
Volume (Å^3)	2689.411	722.052	1448.63
Z	8	2	4
R-Factor (%)	8.40	4.37	4.50
Temperature (K)	283	283-303	283-303
Density	1.34	1.363	1.432
R_1/wR_2	8.40	4.37 (some disorder)	4.50

2.7 References

[1] C. Loschen, A. Klamt, *Pharm. Res.* **2016**, *33*, 2794–2804.

[2] H. D. Clarke, K. K. Arora, H. Bass, P. Kavuru, T. T. Ong, T. Pujari, L. Wojtas, M. J. Zaworotko, *Cryst. Growth Des.* **2010**, *10*, 2152–2167.

[3] C. R. Groom, I. J. Bruno, M. P. Lightfoot, S. C. Ward, *Acta Crystallogr., Sect. B: Struct. Sci. Cryst. Eng. Mater.* **2016**, *72*, 171–179.

[4] A. Bajpai, H. S. Scott, T. Pham, K.-J. Chen, B. Space, M. Lusi, M. L. Perry, M. J. Zaworotko, *IUCrJ*. **2016**, *3*, 430–439.

[5] K. Fujii, M. Aoki, H. Uekusa, *Cryst. Growth Des*. **2013**, *13*, 2060–2066.

[6] S. M. Reutzel-Edens, D. E. Braun, A. W. Newman, in *Polymorphism in the Pharmaceutical Industry* (Eds.: R. Hilfiker, M. von Raumer), Wiley-VCH Verlag GmbH & Co. KGaA, Weinheim, Germany, **2018**, pp. 159–188.

[7] A. L. Gillon, N. Feeder, R. J. Davey, R. Storey, *Cryst. Growth Des*. **2003**, *3*, 663–673.

[8] J. C. Bennion, N. Chowdhury, J. W. Kampf, A. J. Matzger, *Angew. Chem. Int. Ed.* **2016**, *55*, 13118–13121.

[9] K. M. Kersten, M. E. Breen, A. K. Mapp, A. J. Matzger, *Chem. Commun.* **2018**, *54*, 9286–9289.

[10] K. Takieddin, Y. Z. Khimyak, L. Fábián, *Cryst. Growth Des.* **2016**, *16*, 70–81.

[11] L. Jia, S. Zhang, W. Yang, Y. Bao, B. Hou, L. Zhou, Q. Yin, *Cryst. Growth Des*. **2021**, *21*, 3677–3688.

[12] I. Yu. Chernyshov, M. V. Vener, P. V. Prikhodchenko, A. G. Medvedev, O. Lev, A. V. Churakov, *Cryst. Growth Des.* **2017**, *17*, 214–220.

[13] A. G. Medvedev, A. V. Churakov, P. V. Prikhodchenko, O. Lev, M. V. Vener, *Molecules.* **2020**, *26*, 26.

[14] L. M. Foroughi, A. J. Matzger, *Cryst. Growth Des.* **2021**, *21*, 5873–5879.

[15] J. Tang, H. Yang, Y. Cui, G. Cheng, *Mater. Chem. Front.* **2021**, *5*, 7108–7118.

[16] J. Zhou, J. Zhang, B. Wang, L. Qiu, R. Xu, A. B. Sheremetev, *FirePhysChem.* **2021**, S2667134421000444.

[17] V. P. Andreev, *Russ. J. Org. Chem.* **2009**, *45*, 1061–1069.

[18] D. Guo, S. V. Zybin, A. P. Chafin, W. A. Goddard, *ACS Appl. Mater. Interfaces.* **2022**, *14*, 5257–5264.

[19] Q. Sun, N. Ding, C. Zhao, Q. Zhang, S. Zhang, S. Li, S. Pang, *Sci. Adv.* **2022**, *8*, eabn3176.

[20] V. S. Vuppuluri, J. C. Bennion, R. A. Wiscons, I. E. Gunduz, A. J. Matzger, S. F. Son, *Prop., Explos., Pyrotech.* **2019**, *44*, 313–318.

[21] P. Yin, J. M. Shreeve, in *Advances in Heterocyclic Chemistry*, Elsevier, **2017**, pp. 89–131.

[22] T. M. Klapötke, T. G. Witkowski, *Prop., Explos., Pyrotech.* **2015**, *40*, 366–373.

[23] T. G. Witkowski, E. Sebastiao, B. Gabidullin, A. Hu, F. Zhang, M. Murugesu, *ACS Appl. Energy Mater.* **2018**, *1*, 589–593.

[24] A. Maan, R. S. Mathpati, V. D. Ghule, *ChemistrySelect.* **2020**, *5*, 8557–8561.

[25] R. A. Wiscons, R. Nikhar, K. Szalewicz, A. J. Matzger, *Phys. Chem. Chem. Phys.* **2022**, *24*, 11206–11212.

[26] M. A. Navasardyan, S. I. Bezzubov, L. G. Kuz'mina, P. V. Prikhodchenko, A. V. Churakov, *Acta Crystallogr., Sect. E: Cryst. Commun.* **2017**, *73*, 1793–1796.

[27] R. Sevcik, M. Necas, J. Novosad, *Polyhedron.* **2003**, *22*, 1585–1593.

[28] I. J. Bruno, J. C. Cole, P. R. Edgington, M. Kessler, C. F. Macrae, P. McCabe, J. Pearson, R. Taylor, *Acta Crystallogr., Sect. B: Struct. Sci.* **2002**, *58*, 389–397.

[29] L. S. Reddy, S. Basavoju, V. R. Vangala, A. Nangia, *Cryst. Growth Des*. **2006**, *6*, 161–173.

[30] D. K. Kumar, D. A. Jose, A. Das, P. Dastidar, *Chem. Commun.* **2005**, 4059.

[31] R. A. Wiscons, M. K. Bellas, J. C. Bennion, A. J. Matzger, *Cryst. Growth Des*. **2018**, *18*, 7701–7707.

[32] S. Baggio, R. Baggio, A. W. Mombrú, *Acta Crystallogr., Sect. C: Cryst. Struct. Commun.* **1998**, *54*, 1900–1902.

[33] D. Britton, L. C. Thompson, R. C. Holz, *Acta Crystallogr., Sect. C: Cryst. Struct. Commun.* **1991**, *47*, 1101–1103.

[34] W. Huang, H.-F. Qian, *Acta Crystallogr., Sect. E: Struct. Rep. Online.* **2005**, *61*, o2050–o2052.

[35] Y.L. Zhao, D. Benítez, I. Yoon, J. F. Stoddart, *Chem. Asian J.* **2009**, *4*, 446–456.

[36] P. Grobelny, A. Mukherjee, G. R. Desiraju, *CrystEngComm.* **2012**, *14*, 5785.

[37] M. L. Durán, J. A. García-Vázquez, C. Gómez, A. Sousa-Pedrares, J. Romero, A. Sousa, *Eur. J. Inorg. Chem.* **2002**, *2002*, 2348–2354.

[38] A. Congreve, R. Kataky, M. Knell, D. Parker, H. Puschmann, K. Senanayake, L. Wylie, *New J. Chem.* **2003**, *27*, 98–106.

[39] T. Kretz, H.-W. Lerner, M. Bolte, **2011**, DOI 10.5517/CCV21LJ.

[40] B. Q. Ma, H. L. Sun, S. Gao, **2004**, DOI 10.5517/CC7CVHX.

[41] B. Q. Ma, H. L. Sun, S. Gao, **2004**, DOI 10.5517/CC7CVGW.

[42] O. V. Dolomanov, L. J. Bourhis, R. J. Gildea, J. A. K. Howard, H. Puschmann, *J. Appl Crystallogr.* **2009**, *42*, 339–341.

[43] G. M. Sheldrick, *Acta Crystallogr., Sect. A: Found. Adv.* **2015**, *71*, 3–8.

[44] G. M. Sheldrick, *Acta Crystallogr., Sect. C: Struct. Chem.* **2015**, *71*, 3–8.

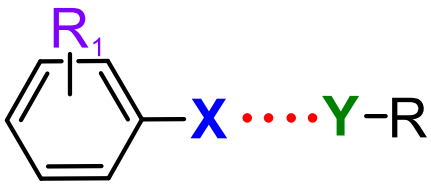
Chapter 3

Halogen Bonding Propensity in Solution: Direct Observation and Computational Prediction

T. A. Bramlett, A. J. Matzger, *Chem. Eur. J.* **2021**, *27*, 15472–15478.

3.1 Introduction

The implementation of non-covalent interactions, such as hydrogen bonding, into supramolecular complex design in chemistry and biology is an attractive approach for molecular recognition.[1-3] Toward this pursuit, various avenues are being investigated to establish robust strategies that can encompass a wide variety of molecular design processes. Halogen bonding, a directional non-covalent interaction between a halogen atom (X) and a Lewis base (LB) as shown in **Figure 3.1**,[4–7] has been observed to facilitate strong and directional interactions in the solid state, solution, and gas phase and is well described with computational modeling.[8]



R= C, N, Ar, halogen, etc….
R_1= EDG or EWG
X= halogens (Cl, Br, and I)
Y= atom with lone-pair of electrons (N, O, S, etc...)

Figure 3.1. Illustration of halogen bonding interactions between a halogenated compound and a Lewis base.

Formation of these types of interactions is associated with a σ-hole,[6,9,10] a region of electropositive potential located on the halogen atom along the axis of the covalent bond, that allows halogens to act as electron pair acceptors upon interaction with a LB.[9] The strength of halogen bonding interactions and extent to which the σ-hole magnitude increases relate to the polarizability of halogen atoms following the order of F < Cl < Br < I.[7] Iodine, the most polarizable in the series, develops larger σ-holes which can lead to stronger interactions upon complexation.[11,12] Since the discovery of halogen bonding, researchers have been exploring the ways in which halogen bonds (XBs) are affected by substituents in both aromatic[13] and non-aromatic systems, designing halogen bond donor/acceptor complexes and employing computational methods that can predict halogen bonding interactions and their strengths.[4,14] Commonly evaluated concepts pertaining to the driving forces for halogen bonding interactions are polarizability, dispersion, charge transfer, and electrostatics, which are accessible from computational methods.[15] Design strategies for non-covalent complex formation frequently utilize electrostatic potential (ESP)[16-18] maps of both the donor and acceptor as a way to predict interaction propensities thus enabling correlations to interaction strengths to be made.[16,19] ESP maps as illustrated in **Figure 3.2**, are used as quantitative representations of charge distribution characterized by maximum electrostatic potential ($V_{s,max}$) and minimum electrostatic potential ($V_{s,min}$) values;[16,20,21] $V_{s,max}$ and $V_{s,min}$ are relevant to the magnitude of the σ-hole and lone pairs, respectively.

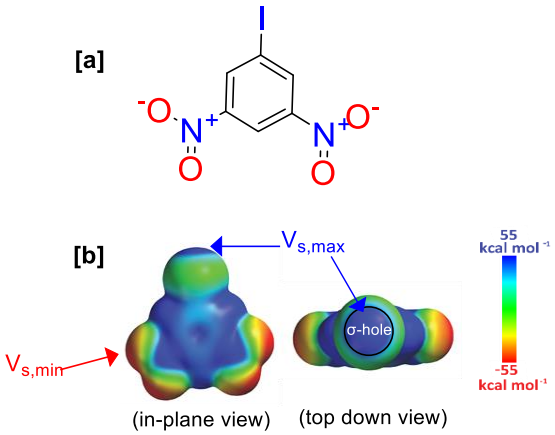


Figure 3.2. (**a**) 1-iodo-3,5-dinitrobenzene strucuture. (**b**) Electrostatic potential map of 1-iodo-3,5-dinitrobenzene with positive ($V_{s,max}$) to negative ($V_{s,min}$) regions (blue +55 to red -55 kcal mol^{-1}), respectively.

Many studies have reported taking advantage of ESP maps as a predictive tool for the design of solid-state supramolecular assemblies.[16–19,22,23] In cases involving halogen bonding between aromatic partners,[23,24] the approach for selecting XB donors and acceptors relies on electron withdrawing or donating substituents that activate the interacting sites involved.[18,22,24] The best donors contain large positive $V_{s,max}$ values and the best acceptors have large negative $V_{s,min}$ values. Though the use of ESP maps to predict interactions in the solid state is common,[16,25] such interactions are perturbed by competition among hierarchies of intermolecular forces[24] that facilitate assembly within a crystal lattice making direct correlations tenuous. To overcome this challenge, we have set out to investigate solution phase halogen bonding to evaluate the use of theoretical gas phase binding energies (ΔE_{bind})[26] to predict favorable halogen bonding propensities.[27–29] ΔE_{bind} are then compared with predictions from ESP maps, as a predictor of halogen bonding propensities in solution. Five iodinated XB donors with various extents of electronic activation and four nitrogen heterocyclic XB acceptors are experimentally assessed via Raman spectroscopy to analyze interaction propensity.

3.2 Results and Discussion

3.2.1 Electronic effects on XB strength

ESP maps were used to choose complementary XB donor and acceptor pairs in **Figure 3.3**. The values associated with the most positive and negative electrostatic potentials, on the ESP maps (0.002 e/au isosurface) for a given XB donor and acceptor, are $V_{s,max}$ and $V_{s,min}$, respectively.[20] Electron withdrawing substituents (fluoro and nitro) influence the strength of XB donors through the activation of the σ-hole.[27,28,30]

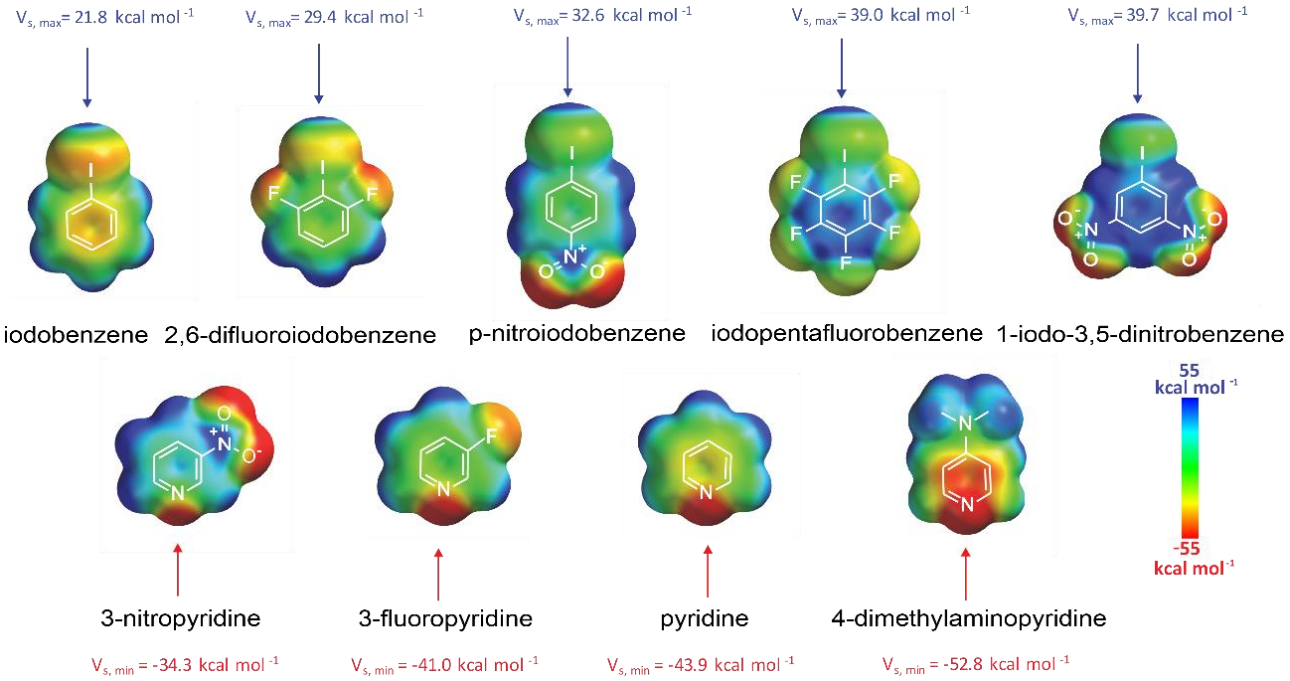


Figure 3.3. ESP maps of iodinated halogen bond donors and pyridine derived acceptors to visualize $V_{s,max}$ (blue) and $V_{s,min}$ (red) regions (kcal mol^{-1}) at the B3LPY/6-311G** level of theory.

The σ-hole magnitude of the iodobenzenes increases in the order iodobenzene (IB) < 2,6-difluoroiodobenzene (DFIB) < p-nitroiodobenzene (p-NIB), < iodopentafluorobenzene (IPFB) < 1-iodo-3,5-dinitrobenzene (IDNB). $V_{s,max}$ values range between positive ESPs of 21.8 kcal mol^{-1}, for the smallest σ-hole containing molecule (IB), and 39.7 kcal $mo1^{-1}$ for the largest (IDNB). $V_{s,min}$ values for the XB acceptors increase as acceptor strengths of the nitrogen atom lone pairs increase. XB acceptor strengths increase following the trend: 3-nitropyridine (3-NPy) < 3-fluoropyridine (3-FPy) < pyridine (PY) < 4-dimethylaminopyridine (DMAP). Negative $V_{s,min}$ values (-34.3 kcal mol^{-1} for the weakest acceptor 3-NPy) to -52.8 kcal mol^{-1} (for the strongest acceptor DMAP) are calculated. **Table 3.1** lists all XB donors and acceptors with corresponding $V_{s,max}$ and $V_{s,min}$ values.

Table 3.1. Electrostatic potential values for the XB donors and acceptors in kcal mol^{-1} calculated at B3LYP/6-311G** level.

XB Donors	**$V_{s,max}$**	**XB Acceptor**	**$V_{s,min}$**
IB	21.8	3-NPy	-34.3
DFIB	29.4	3-FPy	-41.0
p-NIB	32.6	PY	-43.9
IPFB	39.0	DMAP	-52.8
IDNB	39.7		

The $V_{s,min}$ value from an interacting acceptor was subtracted from the $V_{s,max}$ value from a donor to produce an electrostatic potential energy difference value (ΔV_s). It has been hypothesized that the energy difference ($\Delta V_s = V_{s,max} - V_{s,min}$) between a donor and acceptor pair suggests how strongly a donor would interact with an acceptor.[16] **Table 3.2** shows that when the difference between $V_{s,max}$ and $V_{s,min}$ of all XB donors and acceptors is applied, the ΔV_s values of the 20 complexes suggest an increase in halogen bonding propensities as ΔV_s increases positively from 56.1 kcal mol^{-1} for IB/3-NPy to 92.5 kcal mol^{-1} for IDNB/DMAP. IDNB is the largest σ-hole containing XB donor of the series with the greatest ΔV_s energy difference and is predicted, based on the ΔV_s

values, to have the strongest interactions with all the acceptors. Note, IPFB follows closely behind IDNB having ΔV_s energy difference values between donor and acceptor pairs less than 1 kcal mol^{-1} weaker.

Table 3.2. ΔV_s values of all 20-halogen bond donor/acceptor complexes in kcal mol^{-1} calculated at B3LYP/6-311G** level.

	XB Donors				
XB Acceptors	IB	DFIB	p-NIB	IPFB	IDNB
3-NPy	56.1	63.7	66.9	73.3	74.0
3-FPy	62.8	70.4	73.6	80.0	80.7
PY	65.7	73.3	76.5	82.9	83.6
DMAP	74.6	82.2	85.4	91.8	92.5

Though ESPs have been demonstrated as a way to predict bonding preferences,[17,22,27] there are a multitude of energy factors aside from electrostatics[31] that influence binding affinities of XB donor/acceptor pairs that are not taken into account.[32,33] As a means of considering the energy factors that contribute to halogen bonding interactions as a whole, theoretical binding energy ($\Delta E_{bind} = E_{complex} - (E_{XB\ donor} + E_{XB\ acceptor})$), which encompasses the total energy of each XB donor, acceptor, and complex, was explored. **Table 3.3** shows the listing of total energy in hartrees of each XB donor, acceptor, and complex. Calculated ΔE_{bind} values for the selected XB donor/acceptor complexes are shown in **Table 3.4**.

Table 3.3. Listing of total energies (hartrees) for all XB bond donors, acceptors, and complexes at B3LYP/6-311G** level of theory using Spartan '16.

Donors	**Total Energies (hartrees)**
iodobenzene	-7151.223106
2,6-difluoroiodobenzene	-7349.745974
p-nitroiodobenzene	-7355.777159
iodopentafluorobenzene	-7647.501169
1-iodo-3,5-dinitrobenzene	-7560.324533
Acceptors	
3-nitropyridine	-452.899217
3-fluoropyridine	-347.608788
pyridine	-248.346868
4-dimethylaminopyridine	-382.35383
XB Donor/Acceptor Complex	
iodobenzene/3-nitropyridine	-7604.122323
iodobenzene/3-fluoropyridine	-7498.831894
iodobenzene/pyridine	-7399.569974
iodobenzene/4-dimethylaminopyridine	-7533.576936
2,6-difluoroiodobenzene/3-nitropyridine	-7802.645191
2,6-difluoroiodobenzene/3-fluoropyridine	-7697.354762
2,6-difluoroiodobenzene/pyridine	-7598.092842
2,6-difluoroiodobenzene/4-dimethylaminopyridine	-7732.099804
p-nitroiodobenzene/3-nitropyridine	-7808.676376
p-nitroiodobenzene/3-fluoropyridine	-7703.385947
p-nitroiodobenzene/pyridine	-7604.124027
p-nitroiodobenzene/4-dimethylaminopyridine	-7738.130989
iodopentafluorobenzene/3-nitropyridine	-8100.400386
iodopentafluorobenzene/3-fluoropyrindine	-7995.109957
iodopentafluorobenzene/pyridine	-7895.848037
iodopentafluorobenzene/4-dimethylpyridine	-8029.854999
1-iodo-3,5-dinitrobenzene/3-nitropyridine	-8013.22375
1-iodo-3,5-dinitrobenzene/3-fluoropyridine	-7907.933321
1-iodo-3,5-dinitrobenzene/pyridine	-7808.671401
1-iodo-3,5-dinitrobenzene/4-dimethylpyridine	-7942.678363

Table 3.4. Theoretical binding energies (ΔE_{bind}) of all XB donor/acceptor complexes in kcal mol^{-1} calculated at B3LYP/6-311G** level.

	XB Donors				
XB Acceptors	IB	DFIB	p-NIB	IPFB	IDNB
3-NPy	-2.53	-4.16	-3.48	-5.26	-4.37
3-FPy	-2.95	-4.73	-4.26	-6.20	-5.34
PY	-3.31	-5.17	-4.81	-7.00	-6.09
DMAP	-3.97	-6.27	-5.93	-8.77	-7.86

Application of ΔE_{bind} to the halogen bonded donor/acceptor complexes led to the evaluation of halogen bonding interaction trends affected not only by electrostatics, but also additional energy terms. ΔE_{bind} values were plotted against XB acceptor strengths, represented by $V_{s,min}$ values, and a linear correlation was found (**Figure 3.4**) suggesting that binding energies for a given halogen bond donor/acceptor complex are well predicted by acceptor strength. By contrast donor strengths correlate to binding energies but are considerably weaker than the acceptor strengths (**Figure 3.5**).

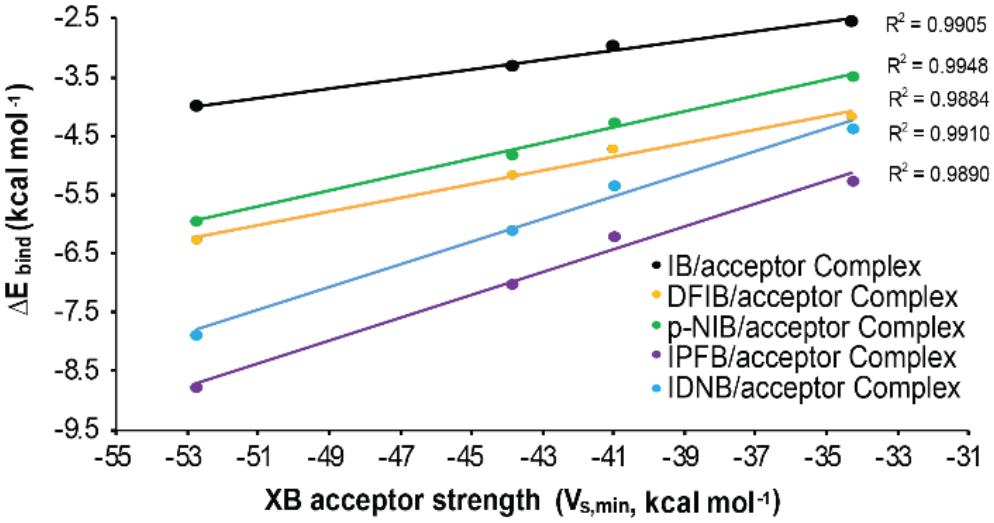


Figure 3.4. Graph representing the correlation between theoretical ΔE_{bind} and XB acceptor strength ($V_{s,min}$, kcal mol^{-1}).

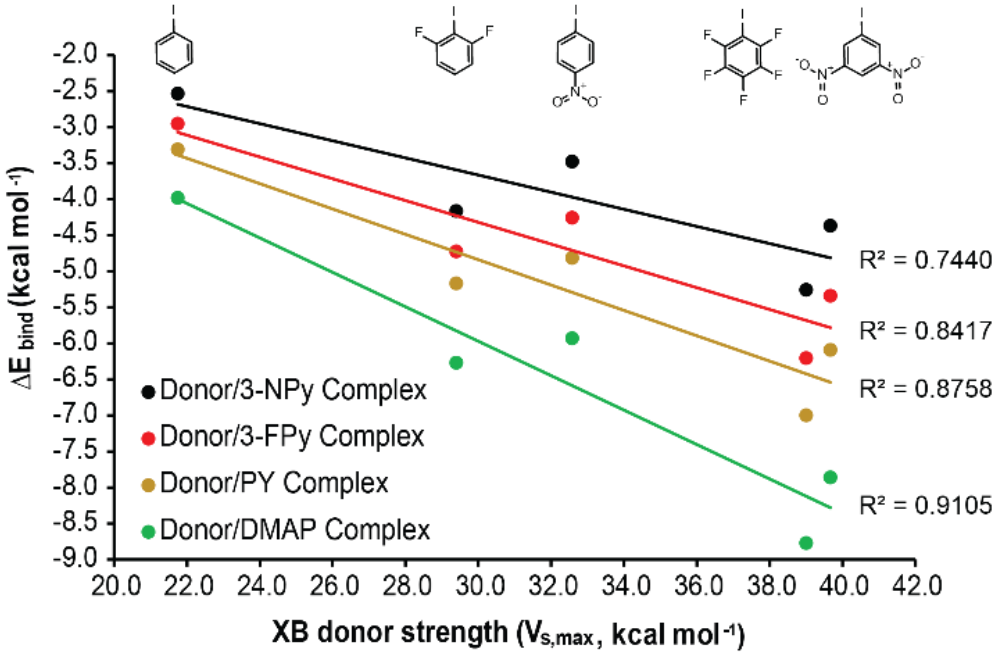


Figure 3.5. Graph representing the correlation between ΔE_{bind} and XB donor strengths ($V_{s,max}$, kcal mol^{-1}).

Figure 3.4 illustrates that as negative $V_{s,min}$ values increase following the trend 3-NPy < 3-FPy < PY < DMAP, there is an increase in the negative ΔE_{bind} values (i.e. binding affinity) within the XB donor/acceptor complexes. DMAP, with a $V_{s,min}$ = -52.8 kcal mol^{-1}, is a better XB acceptor for all XB donors than PY ($V_{s,min}$= -43.9 kcal mol^{-1}), which out-competes 3-FPy ($V_{s,min}$ = -41.0 kcal mol^{-1}) and 3-NPy ($V_{s,min}$ = -34.3 kcal mol^{-1}), and thus forms the strongest XB donors/acceptor complexes.

With respect to the chosen basis set, the B3LYP functional can underestimate forces contributing to association[34] thus a D3 dispersion correction was also examined (**Table 3.5**). B3LYP-D3 calculations in **Table 3.5** show that while the trends in binding energies are the same as B3LYP shown in **Table 3.4**, the binding energies of the complexes are more attractive in nature (average = 2.58 ± 0.26 kcal mol^{-1}) with shorter interaction distances (average = 0.04 ± 0.02 Å) than in B3LYP (**Table 3.6**).

Table 3.5. Calculated theoretical binding energies (ΔE_{bind}) of all XB donor/acceptor complexes (kcal mol^{-1}) at B3LYP-D3/6-311G** level of theory using Spartan '18.

	XB Donors				
XB Acceptors	IB	DFIB	p-NIB	IPFB	IDNB
3-NPy	-4.95	-6.90	-5.76	-8.08	-6.93
3-FPy	-5.16	-7.47	-6.55	-8.67	-7.94
PY	-5.53	-8.08	-7.14	-9.93	-8.75
DMAP	-6.36	-8.87	-8.40	-11.78	-10.85

Table 3.6. Calculated C-I bond lengths (Å) for all XB donors and donor/acceptor complexes with interaction distances (Å) and bond angles (°) at B3LYP and B3LYP-D3/6-311G** level of theory using Spartan '16 and '18.

XB Donor and Donor/Acceptor Complex	**C-I bond length (Å)[a]**	**C-I bond length (Å)[b]**	**C-I bond length (Å)[c]**	**C-I···N distance (Å)[a]**	**C-I···N distance (Å)[b]**	**C-I···N distance (Å)[c]**	**C-I···N bond angle (°)[a]**	**C-I···N bond angle (°)[b]**	**C-I···N bond angle (°)[c]**
IB	2.138	2.140	2.143						
IB/3-NPy	2.140	2.139	2.146	3.207	3.194	3.172	179.62	178.40	179.59
IB/3-FPy	2.141	2.141	2.149	3.164	3.111	3.137	179.63	178.28	179.90
IB/PY	2.142	2.143	2.149	3.139	3.068	3.125	179.84	177.90	179.90
IB/DMAP	2.144	2.144	2.151	3.078	3.035	3.075	179.87	179.36	179.88
DFIB	2.108	2.112	2.110						
DFIB/3-NPy	2.120	2.120	2.126	3.098	3.089	3.046	179.58	179.04	179.65
DFIB/3-FPy	2.124	2.123	2.130	3.054	3.048	3.006	179.65	179.23	179.13
DFIB/PY	2.126	2.128	2.135	3.017	2.962	2.937	179.87	178.51	179.89
DFIB/DMAP	2.132	2.135	2.146	2.946	2.896	2.842	179.79	178.86	179.88
p-NIB	2.126	2.130	2.129						
p-NIB/3-NPy	2.133	2.132	2.136	3.128	3.080	3.098	179.47	178.21	179.53
p-NIB/3-FPy	2.134	2.132	2.138	3.086	3.043	3.069	179.80	178.60	179.81
p-NIB/PY	2.135	2.134	2.140	3.057	3.011	3.042	179.92	178.72	179.92
p-NIB/DMAP	2.137	2.139	2.143	2.995	2.951	2.982	179.85	179.51	179.98
IPFB	2.105	2.106	2.107						
IPFB/3-NPy	2.122	2.123	2.128	3.021	2.980	2.955	179.50	178.19	179.57
IPFB/3-FPy	2.127	2.130	2.138	2.953	2.899	2.839	179.86	178.25	179.90
IPFB/PY	2.133	2.135	2.146	2.885	2.848	2.798	179.88	178.40	179.95
IPFB/DMAP	2.144	2.147	2.158	2.795	2.768	2.736	179.99	179.06	179.99
IDNB	2.123	2.127	2.125						
IDNB/3-NPy	2.133	2.131	2.136	3.060	3.010	3.024	179.22	177.93	179.21
IDNB/3-FPy	2.135	2.130	2.139	3.015	3.000	2.987	179.84	178.66	179.86
IDNB/PY	2.139	2.133	2.140	2.962	2.952	2.920	179.92	178.76	179.94
IDNB/DMAP	2.145	2.145	2.153	2.861	2.838	2.810	179.70	179.27	179.99

[a] Spartan '16 calculations (B3LYP/6-311G**), [b] Spartan '18 calculations (B3LYP-D3/6-311G**), and [c] Spartan '18 (B3LYP/6-311G** in DCM), respectively.

Additionally, ΔE_{bind} calculations were undertaken in the solvent model dichloromethane (DCM) to compare interaction stability. For the DCM solvent model (**Table 3.7**), all XB donor/acceptor complexes are found to have binding energies that are less attractive (average = 1.17 ± 0.56 kcal mol^{-1}) though with shorter interaction distances (average = 0.05 ± 0.03 Å) than those shown in the **Table 3.5** and **Table 3.6**, respectively. The tendency for halogen bonded complexes to have shorter interaction distances in solvent models has been previously reported.[35]

Table 3.7. Calculated theoretical binding energies (ΔE_{bind}) for the solvent model (DCM) of all the XB donor/acceptor complexes (kcal mol^{-1}) at B3LYP/6-311G** level of theory using Spartan '18.

	XB Donors				
XB Acceptors	IB	DFIB	p-NIB	IPFB	IDNB
3-NPy	-1.95	-3.86	-2.47	-4.87	-3.34
3-FPy	-1.99	-4.19	-2.84	-5.1	-3.81
PY	-2.2	-4.64	-3.16	-5.76	-4.27
DMAP	-2.78	-5.22	-3.89	-7.34	-5.38

ΔE_{bind} is a property assigned to a halogen bonding complex and not just the single XB donor or acceptor molecules and therefore consideration was given to the electrostatic potential equivalent, ΔV_s, for insight into predicting halogen bonding interaction trends. When ΔE_{bind} values were plotted against ΔV_s values (**Figure 3.6**), an increase in the strength of the XB donor results in steeper slopes (m) denoting favorable complexation (e.g., IB/acceptor complex (m = -0.080) < DFIB/acceptor complex (m = -0.116) < p-NIB/acceptor complex (m = -0.134) < IDNB/acceptor complex (m = -0.192) < IPFB/acceptor complex (m = -0.194)). The parallel slopes of DFIB and p-NIB/acceptor complexes as well as IDNB and IPFB/acceptor complexes reflect a similar sensitivity within the pairs toward XB acceptors. However, the different slopes evident in **Figure 3.6** suggest that there are energy terms in ΔE_{bind} missing from ΔV_s predictions that differentially affect the complexes containing fluorinated and nitrated XB donors.

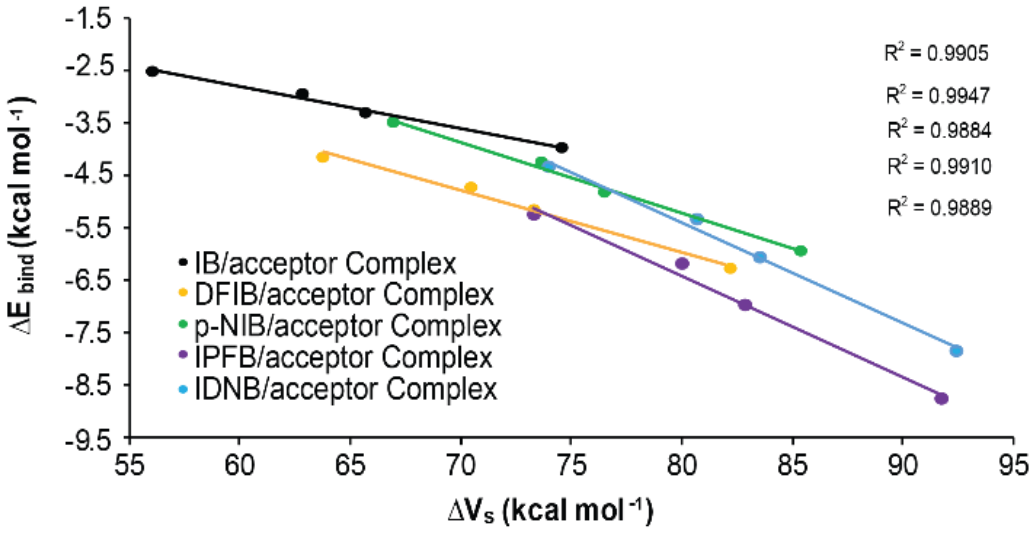


Figure 3.6. Graph representing the correlation between ΔE_{bind} and ΔV_s in kcal mol^{-1}.

ESP predictions, specifically for IPFB and IDNB/acceptor complexes, show that electrostatics alone do not fully describe binding energy trends thus motivating a more thorough analysis of unaccounted for energy terms that can be derived by deconvoluting total energy. The total intermolecular interaction energies for the IPFB/acceptor complexes and IDNB/acceptor complexes were partitioned by absolutely-localized molecular orbital energy decomposition analysis (ALMO-EDA) using the Q-Chem 5.3.2 software package[36] into terms as shown in **Equation 3.1**:

Equation 3.1: $\Delta E = \Delta E_{FRZ} + \Delta E_{POL} + \Delta E_{CT}$

The frozen (FRZ) term is defined as the change in energy from bringing together two fragments that are far apart without allowing any molecular orbital (MO) relaxation and can be further broken down into electrostatics (ELEC), Pauli repulsion (PAULI), and dispersion (DISP) energies (**Equation 3.2**):

Equation 3.2: $\Delta E_{FRZ} = (\Delta E_{ELEC} + \Delta E_{PAULI}) + \Delta E_{DISP}$

The polarization term is described as the intrafragment relaxation of the frozen occupied MOs of each fragment. The charge transfer (CT) term is derived from further interfragment relaxation of the frozen occupied MOs of each fragment. In assessing the values of the ALMO-EDA terms, initial focus was placed on evaluating the frozen terms because these do not include fragment relaxation and encompass electrostatic effects. **Table 3.8** shows that both IPFB and IDNB/acceptor complexes have comparable electrostatic/Pauli repulsion (computed as a combined ELEC+PAULI) terms for a given acceptor and are repulsive overall. The greater repulsion observed with better acceptors is consistent with their closer interactions as shown in **Table 3.6** and a dominance of the Pauli repulsion term. The dispersion terms in IPFB and IDNB/acceptor complexes are very similar to one another and are attractive (negative values) for a given acceptor.

Table 3.8. Deconvoluted frozen (FRZ) term ($\Delta E_{FRZ} = (\Delta E_{ELEC} + \Delta E_{PAULI}) + \Delta E_{DISP}$) in kcal mol^{-1} as dispersion (DISP), electrostatics (ELEC), and Pauli repulsion (PAULI) energies in ALMO-EDA for IPFB/acceptor complexes and IDNB/acceptor complexes.

XB Acceptors	**ELEC+PAULI**	**DISP**	**ΔE_{FRZ}**
IPFB/3-NPy	0.69	-0.83	-0.14
IPFB/3-FPy	1.21	-1.00	0.21
IPFB/PY	2.11	-1.19	0.92
IPFB/DMAP	3.32	-1.46	1.86
IDNB/3-NPy	1.09	-0.76	0.33
IDNB/3-FPy	1.06	-0.86	0.2
IDNB/PY	1.51	-1.00	0.51
IDNB/DMAP	2.64	-1.28	1.36

Including intrafragment (polarization) and interfragment (charge transfer) relaxation in the ALMO-EDA results gives the full picture of the energy terms influencing halogen bonding strength (**Table 3.9**, see **Tables 3.12-3.19** in the **Additional Tables** section for Cartesian

coordinates). IPFB/acceptor complexes show a significantly larger charge transfer contribution, relative to the total interaction energy, than IDNB/acceptor complexes which counter the trends from the frozen terms. This finding echoes the results on iodomethane derivatives.[37] The implication of larger CT in IPFB than IDNB/acceptor complexes, which is reflected in the theoretical binding energies, is indicative of greater dimer stabilization (C-I···N), more so in IPFB/acceptor complexes than IDNB/acceptor complexes. The polarization terms, while not as prominent as CT in either IPFB or IDNB/acceptor complexes, are also attractive in nature and contribute to complex stability.

Table 3.9. Summary of interaction energies ($\Delta E = \Delta E_{FRZ} + \Delta E_{POL} + \Delta E_{CT}$) in kcal mol $^{-1}$ deconvoluted into 3 energy terms (frozen (FRZ), polarization (POL), and charge transfer (CT)) in ALMO-EDA from Q-Chem 5.3.2 for IPFB/acceptor complexes and IDNB/acceptor complexes.

XB Donor/Acceptor Complex	FRZ	POL	CT	ΔE
IPFB/3-NPy	-0.14	-1.06	-4.06	-5.26
IPFB/3-FPy	0.21	-1.51	-4.97	-6.27
IPFB/PY	0.92	-2.02	-6.02	-7.12
IPFB/DMAP	1.86	-3.13	-7.84	-9.11
IDNB/3-NPy	0.33	-0.98	-3.67	-4.32
IDNB/3-FPy	0.2	-1.32	-4.31	-5.43
IDNB/PY	0.51	-1.68	-5.05	-6.22
IDNB/DMAP	1.36	-2.69	-6.66	-7.99

3.2.2 Observation of halogen bonding in solution

While general agreement is found between the gas phase ΔE_{bind} and ΔV_s for halogen bonding predictions, the discrepancy in ordering the relative binding strengths of XB donor/acceptor complexes featuring XB donors with fluoro and nitro substituents, motivated comparison to experimental results for halogen bonding interactions. All XB donor and acceptor pairs were analyzed via Raman spectroscopy in order to assess halogen bonding interaction trends

between and perturbations within the molecules. Raman spectroscopy was employed for analysis of halogen bonding in solution studies due to detection sensitivity toward the formation of halogen bonded complexes. Red shifted C-I vibrational frequencies (ν) of XB donors, denoting XB complex formation, were analyzed. The compilation of C-I stretching frequencies are shown for each XB donor and complex (if detected) in **Table 3.10**.

Table 3.10. C-I stretching vibrational frequency (ν) in cm^{-1} of each unbound XB donor and each complex observed in CH_2Cl_2.

XB donors and XB Complexes	**C-I Raman Shift (cm^{-1})**
IB	266.0
p-NIB	213.6
DFIB	218.7
DFIB/DMAP	211.7[a]
IPFB	204.0
IPFB/3-FPy	197.2 [a]
IPFB/PY	194.6[a]
IPFB/DMAP	190.0[a]
IDNB	241.9
IDNB/DMAP	233.4[a]
[a] Red shifted peaks of formed complexes.	

For each Raman experiment, the C-I stretching vibrational frequencies of unbound 1.00 mol/kg (molal) solutions of the XB donors (except 0.220 mol/kg p-NIB due to limited solubility) were examined as reference points to evaluate the magnitude of potential red shifting in C-I stretches due to interactions with XB acceptors. Upon the addition of the XB acceptors (0.500 equiv, 1.00 equiv, and 1.50 equiv), the extent to which halogen bonding interactions were taking place, through the observation of newly formed, red shifted C-I peaks signifying complexation (iodine interacting with pyridyl nitrogen: C-I···N), was evaluated. Raman spectra for IB, p-NIB,

and DFIB/acceptor mixtures were predicted to form weak XB donor/acceptor interactions by both computed ΔV_s and ΔE_{bind}. The XB donor/acceptor mixtures contained only the C-I stretching vibrational frequency of unbound IB at $\boldsymbol{\nu}$ = 266.0 cm^{-1}, unbound p- NIB at $\boldsymbol{\nu}$ = 213.6 cm^{-1}, and unbound DFIB at $\boldsymbol{\nu}$ = 218.7 cm^{-1} (with the exception of DFIB/DMAP mixtures shown in **Figure 3.7**.

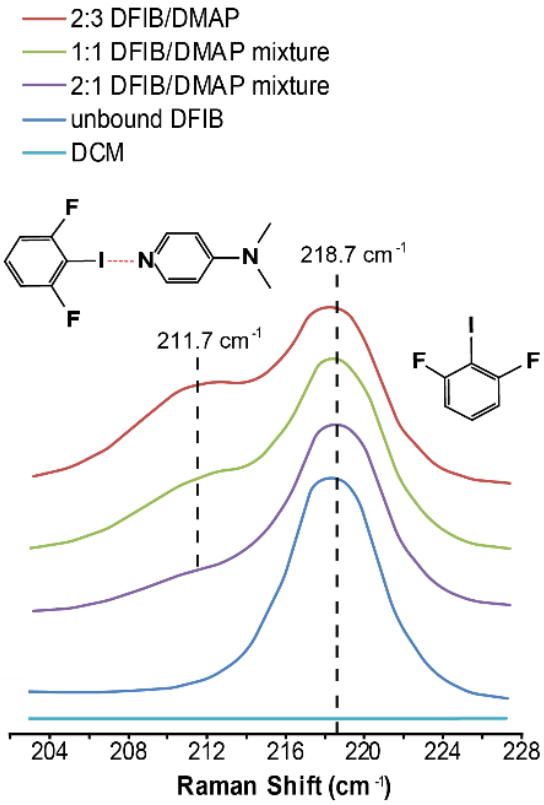


Figure 3.7. Raman spectra of unbound DFIB and 2:3, 1:1, and 2:1 molar ratios of DFIB/DMAP solutions.

In contrast to a purely electrostatic model based on ΔV_s, ΔE_{bind} predicts that IPFB binds more strongly with XB acceptors than IDNB. Interactions between IPFB/acceptors (3-NPy, 3-FPy, PY, and DMAP) were evaluated and the following observed: complex formation, denoted by a red shift in newly formed C-I peak compared to that of unbound IPFB at $\boldsymbol{\nu}$ = 190.0 cm^{-1}, was observed in all XB acceptor concentrations except with 3-NPy (the weakest Lewis base). **Figure 3.8a** with IPFB/3-FPy mixtures illustrates the presence of the C-I···N interaction from new, red shifted C-I

vibrational stretching frequency at $\boldsymbol{\nu}$ = 197.2 cm^{-1}, which is consistent with the ΔE_{bind} predictions for the IPFB/3-FPy complexes. IPFB/PY complexes with C-I stretches at $\boldsymbol{\nu}$ = 194.6 cm^{-1} (**Figure 3.8b**) and IPFB/DMAP complexes with C-I stretches at $\boldsymbol{\nu}$ = 190.0 cm^{-1} (**Figure 3.8c**) show distinct peak formation consistent with stronger halogen bonding interactions than 3-FPy complexes. The more intense red shifted peak formation within IPFB/DMAP complexes was found as the molar ratio of DMAP increased. This correlates back to the strength of DMAP as a good XB acceptor from the predictions of both ΔE_{bind} and ΔV_s computed calculations.

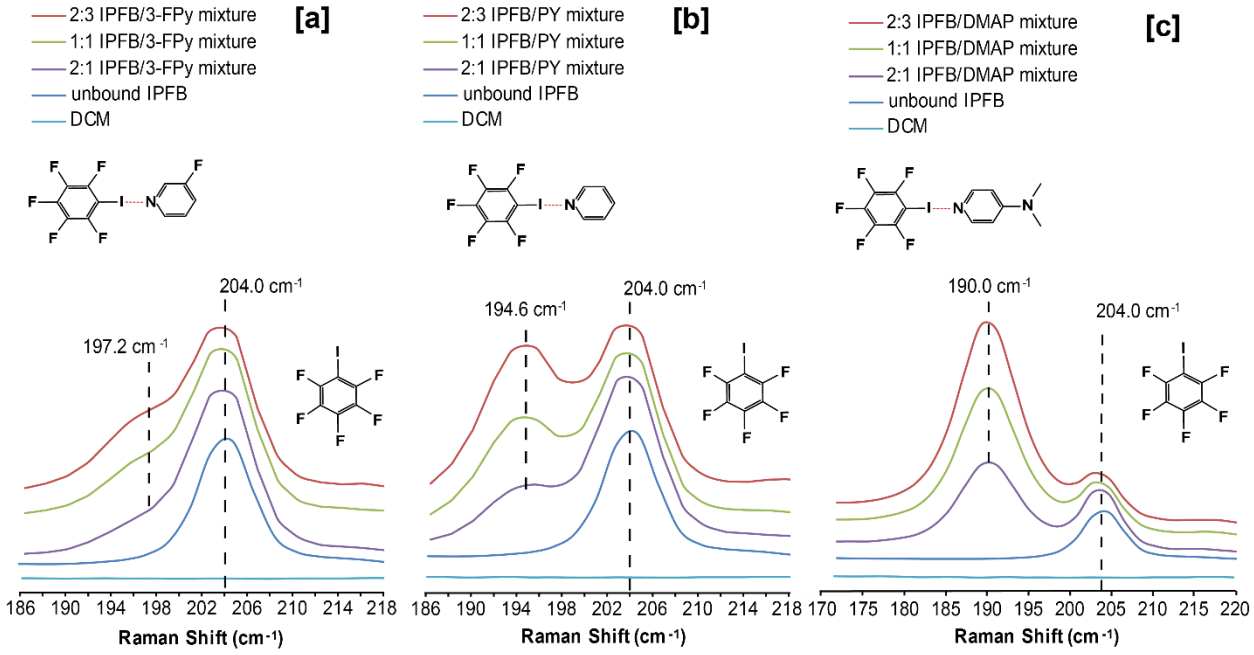


Figure 3.8a-c. Raman spectra of unbound IPFB and 2:3, 1:1, and 2:1 molar ratios of (**a**) IPFB/3-FPy solutions, (**b**) IPFB/PY, and (**c**) IPFB/DMAP solutions.

The experimental outcome of the interactions between IDNB/acceptors was not predicted by the ESPs. IDNB, in comparison to the other XB donors, has the largest σ-hole region and $V_{s,max}$ value which suggests the most favorable interactions to occur with the addition of a XB acceptor (large computed ΔV_s). Therefore, the formation of new red-shifted C-I stretches were expected to be observed in all IDNB/acceptor solution experiments. However, analysis of the Raman spectra

yielded only one successful complexation experiment (IDNB/DMAP) with a red shifted peak at $\boldsymbol{\nu}$ = 233.4 cm^{-1} (**Figure 3.9**) and 241.9 cm^{-1} for unbound IDNB.

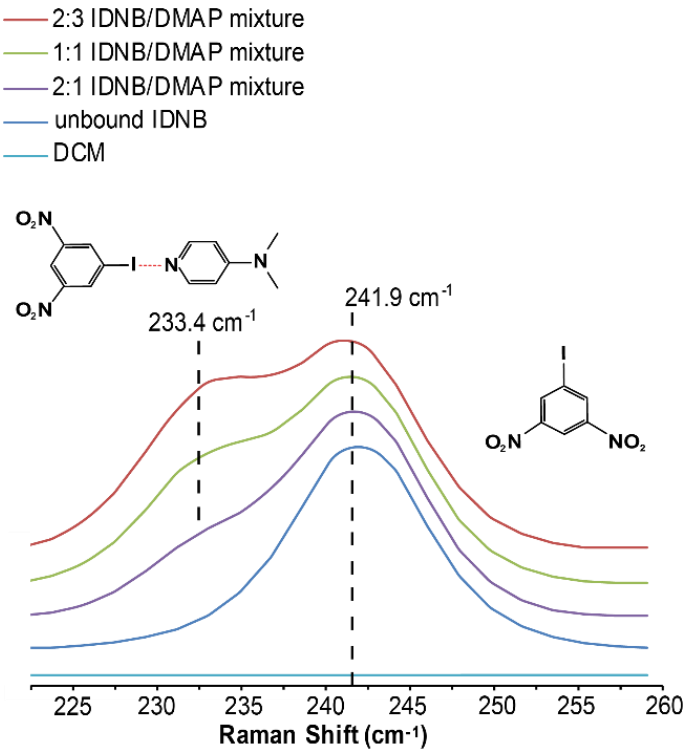


Figure 3.9. Raman spectra of unbound IDNB and 2:3, 1:1, and 2:1 molar ratios of IDNB/DMAP solutions.

Raman spectra of IPFB/acceptor complexes and IDNB/acceptor complexes were compared to resolve which predictions (i.e. ΔE_{bind} or ΔV_s) more accurately suggest the orders and strengths of halogen bonding propensities. Note, ΔE_{bind} are directly related to the observed red shifts in the Raman spectra (**Figure 3.10**), where the relationship between the two is as follows: with strong binding affinity there is also a large shift in the C-I stretch from the unbound to the bound halogen bond donor.

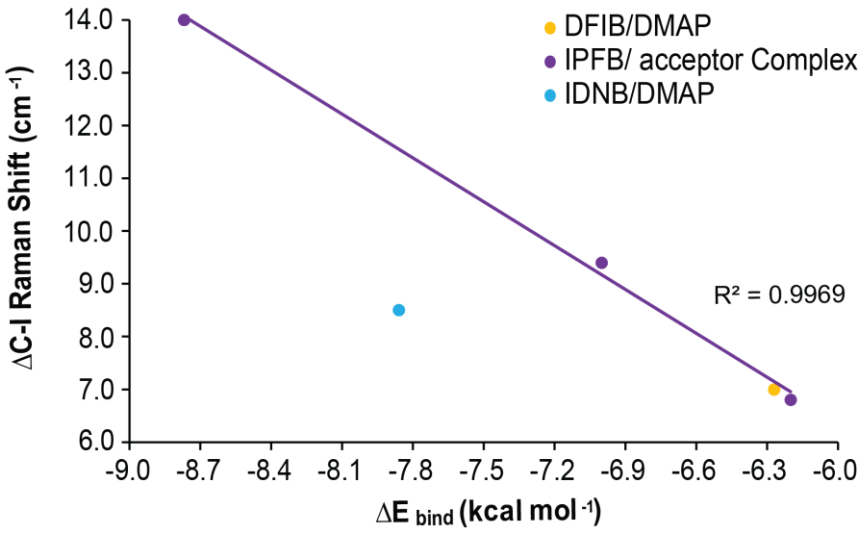


Figure 3.10. Graph representing the correlation between observed red shifted ΔC-I stretch (cm^{-1}) and ΔE_{bind} (kcal mol^{-1}). The purple line represents the fit for observed IPFB/acceptor complexes.

Raman spectra reveal ΔE_{bind} does reflect the distinct interaction strength hierarchy between IPFB/acceptor complexes and IDNB/acceptor complexes exhibited in the Raman spectra. Notably, the computed C-I···N interaction distances in IPFB and IDNB/acceptor complexes are consistent with the theoretical binding energy predictions (**Figure 3.11**) rather than ESP predictions. Additionally, relative areas of the bound and unbound states were used to estimate ΔG values for the observed complexes which are shown in **Table 3.11**. The relative concentration of the bound states for each observed complex was found to increase with increasing acceptor strengths (ΔG values become more negative) across a particular XB donor/acceptor complex. Overall, IPFB is proven, experimentally and in agreement with ΔE_{bind} predictions, to be the stronger interacting XB donor despite having a somewhat smaller σ-hole magnitude than IDNB. The origin of this is contributed to a greater degree of CT within IPFB/acceptor complexes than IDNB/acceptor complexes.

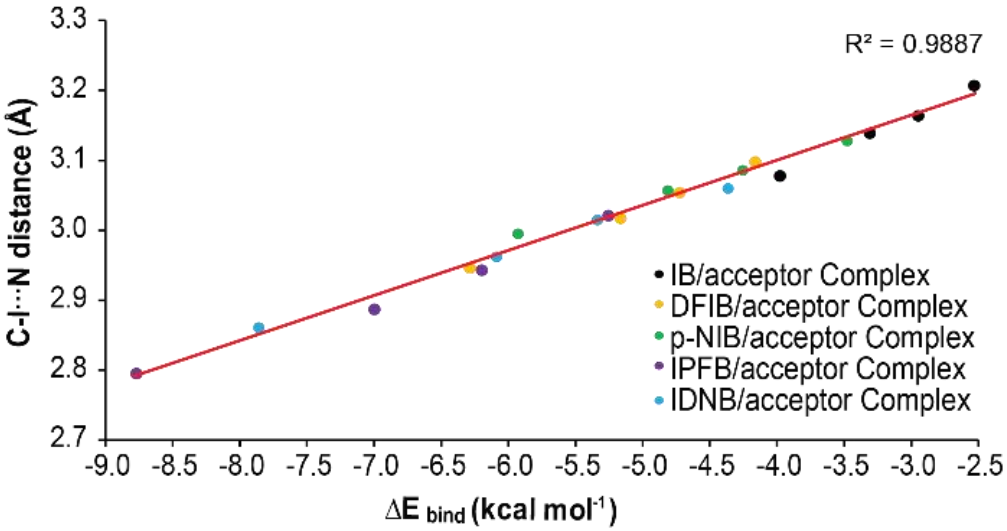


Figure 3.11. Graph representing the correlation between C-I···N interaction distances (Å) and ΔE_{bind} (kcal mol^{-1}).

Table 3.11. ΔG values (kcal mol^{-1}) of observed XB donor/acceptor complexes were derived from the relative areas of the bound and unbound donors to determine relative concentration of bound and unbound states. These free energy values assume equal Raman scattering.

XB Acceptors	**XB Donors**		
	0.50 mol/kg DFIB	0.50 mol/kg IPFB	0.50 mol/kg IDNB
0.75 mol/kg 3-FPy		-0.22	
0.75 mol/kg PY		-0.51	
0.75 mol/kg DMAP	-0.41	-1.78	-2.34

3.3 Conclusion

The most common method for predicting halogen bonding propensities, electrostatic potential calculations, fails to reproduce theoretical or experimental binding properties for highly activated halogen bond donors. Raman spectroscopy was employed to observe both the extent of C-I vibrational frequency shifts in solution of XB donor when a XB acceptor solution was added and to evaluate the population of the bound state relative to the ranking of interaction strengths. These studies unambiguously demonstrate that a model based on the electrostatics of the uncomplexed donor has limited predictive ability even in a relative sense. IPFB and

IDNB/complexes containing the most powerful acceptors were further evaluated using ALMO-EDA revealing that, although larger σ-holes are generally indicative of stronger binding affinity, partitioning into charge transfer, frozen, and polarization terms points to significant charge transfer interactions in differentiating binding strength. The findings inform broad applications in the fields of chemistry, crystal engineering, and molecular recognition because reliable methods to predict strong non-covalent interactions in solid, solution, and gas phases are essential for populating the supramolecular design toolbox.

3.4 Methods

Raman spectra were recorded at room temperature using a Renishaw inVia Qontor Raman Microscope (Laser λ=532 nm) featuring a Leica microscope, 1800 lines/mm gratings, a CCD area detector, and 50 μm slit size. Using WiRE 3.4 software package (Renishaw) and a silicon internal standard for calibration, spectra for the XB solution experiments were collected via 50 increments of scans at 0.5 secs per scan in static mode, with a range of 120-820 reciprocal wavelength (cm^{-1}). The chemical shifts are given in cm^{-1}, the signal of the dissolved halogen bond donors' C-I vibrational frequency shifts (at ν =190-266 cm^{-1}) have been used as reference signals.

3.4.1 Experimental Setup

All reagents were commercially available, purchased, and used without any additional purification. Stock solutions of 5.00 mL of 1.00 mol/kg XB donors (~0.220 mol/kg p-NIB due to low solubility) were made, in dry solvent DCM, in tared 20 mL vials by converting the molecular weight (g mol^{-1}) of each XB donor to moles (mol) then dividing it by kilograms (kg) of solvent DCM. DCM was selected as the solvent for Raman solution studies because it dissolves the XB donors and acceptors without contributing peaks that overlap with those of interest in the XB

donor/acceptor complexes. The XB acceptor stock solution concentrations were made from the serial dilution of 5.00 mL of 1.50 mol/kg. Solutions at 1.00 mol/kg were achieved by aliquoting 1.90 mL of the 1.50 mol/kg stock solution into a 10 mL graduated cylinder and diluting it with DCM to a final volume of 3.00 mL then pipetted into a 4 mL vial. Solutions at 0.500 mol/kg were achieved by aliquoting 1.00 mL of the 1.00 mol/kg stock solution into a graduated cylinder and diluting it with DCM to a final volume of 2.00 mL then pipetted into a 4 mL vial. Each donor solution (200 µL) and acceptor solution (200 µL), 1:1 by volume, were added to a clean 4 mL vial then placed on the stage of the Raman microscope and data collected with a 5x objective lens.

3.4.2 Computations

Density functional theory (DFT) and electrostatic potential maps (mapped on 0.002e/au electron density contour) were calculated at the B3LYP level of theory and 6 311G**basis set with Spartan'16 software (Wavefunction Inc., Irvine, CA). Energies in the gas phase (B3LYP-D3/6-311G**) and solution phase with the Conductor like Polarizable Continuum Model (C-PCM) in DCM (dielectric constant = 8.93) at B3LYP/6-311G** were calculated with Spartan '18 software. Starting geometrics were set to mimic halogen bonding interactions found in the CSD (Cambridge Structural Database), where all interactions were built to interact at a ~180° bond angle for C-I···N interactions with energy minimization. The achievement of minimum energy geometry was confirmed by the absence of imaginary frequencies. Single point energy and second generation ALMO-EDA calculations were performed at the B3LYP/6-311G** level of theory using the Q-Chem 5.3.2 software package for iodopentafluorobenzene and 1-iodo-3,5-dinitrobenzene/acceptor complexes.

3.5 Additional Tables

Table 3.12. Cartesian coordinates of the computed IPFB/3-NPy complex at the B3LYP/6-311G** level of theory in Q-Chem 5.3.2 for ALMO-EDA.

IPFB/3-NPy Complex			
0 1			
--			
0 1			
H	-2.2862038747	0.3023848969	2.2733190345
C	-1.3784360155	0.1944638120	2.8584771106
H	-2.3552750686	0.4245362032	4.7639751643
C	-1.4162437060	0.2640118990	4.2496682186
C	-0.2286182882	0.1248536415	4.9562023187
C	0.9309128487	-0.0789282291	4.2208382988
H	1.7983490247	-0.3005188574	2.2625073686
C	0.8911626009	-0.1399047474	2.8317898700
N	-0.2535213489	-0.0027023860	2.1620104666
N	2.2253059519	-0.2317297745	4.9194391595
O	3.2165587297	-0.4107055518	4.2283734387
O	2.2130612905	-0.1675896626	6.1397946082
H	-0.1805839783	0.1703660424	6.0357346747
--			
0 1			
C	-0.2652971638	-0.0164565854	-2.9805147179
C	-0.2641581045	-0.0082280687	-5.7780300455
C	-0.4990498990	1.1700739636	-5.0797623675
C	-0.0300709253	-1.1906364095	-5.0864671519
C	-0.0325832330	-1.1865332509	-3.6965782384
C	-0.4976935634	1.1576949841	-3.6900198536
I	-0.2637279138	-0.0211568842	-0.8584385292
F	-0.7255795333	2.3088113172	-3.0482262821
F	0.1937781034	-2.3413214752	-3.0614096300
F	0.1945301219	-2.3216535240	-5.7618798131
F	-0.2636252118	-0.0042166574	-7.1119440977
F	-0.7229908435	2.3050853041	-5.7488590045

Table 3.13. Cartesian coordinates of the computed IPFB/3-FPy complex at the B3LYP/6-311G** level of theory in Q-Chem 5.3.2 for ALMO-EDA.

IPFB/3-FPy Complex			
0 1			
--			
0 1			
H	-2.0118348499	-0.4519684946	2.6937728917
C	-1.1201771816	-0.2491749324	3.2776117129
H	-2.0817586447	-0.4761575134	5.1900160798
C	-1.1562944095	-0.2629196027	4.6694646959
C	0.0129681427	0.0000217989	5.3760543835
C	1.1562397785	0.2634308257	4.6403169719
H	2.0178046869	0.4719322285	2.6786833115
C	1.1206161084	0.2630818671	3.2522754386
H	0.0497580894	0.0030294349	6.4584774147
N	-0.0064697344	0.0086566013	2.5852260440
F	2.3163741701	0.5213592761	5.2701015313
--			
0 1			
C	-0.0277436144	-0.0116347371	-5.2944936066
C	-0.0216318294	-0.0038036999	-2.4952931384
C	0.2052088822	1.1709374950	-4.6030477011
C	-0.2576870982	-1.1903289217	-4.5954665848
C	-0.2524448833	-1.1775938335	-3.2056534308
C	0.2060249985	1.1660057687	-3.2131240279
I	-0.0182903711	0.0016821891	-0.3680260844
F	-0.4763249059	-2.3306541851	-2.5647936796
F	0.4319115493	2.3226351013	-2.5796187626
F	-0.4814747598	-2.3261752532	-5.2643271676
F	-0.0307133459	-0.0154219625	-6.6290318905
F	0.4259392223	2.3030605494	-5.2791244017

Table 3.14. Cartesian coordinates of the computed IPFB/3-PY complex at the B3LYP/6-311G** level of theory in Q-Chem 5.3.2 for ALMO-EDA.

IPFB/PY Complex			
0 1			
--			
0 1			
H	-1.9191074	-0.7331105	2.6677156
C	-1.0641895	-0.4063393	3.2517841
H	-1.9907514	-0.7632359	5.1589220
C	-1.1016280	-0.4220865	4.6429048
C	0.0216650	0.0075758	5.3432567
C	1.1352072	0.4344783	4.6258533
H	1.9255264	0.7376683	2.6385034
C	1.0786131	0.4134022	3.2354993
N	0.0024548	0.0022996	2.5573272
H	0.0291459	0.0097210	6.4272519
H	2.0313537	0.7775925	5.1282525
--			
0 1			
C	-0.0101254	-0.0036274	-2.4610035
C	-0.0146264	-0.0060774	-5.2603337
C	0.2075018	1.1771623	-4.5666016
C	-0.2345534	-1.1880952	-4.5638381
C	-0.2299828	-1.1773408	-3.1740170
C	0.2073752	1.1688496	-3.1767365
I	-0.0072071	-0.0021271	-0.3275951
F	0.4234033	2.3264781	-2.5402918
F	-0.4442619	-2.3337927	-2.5348372
F	-0.4485238	-2.3246036	-5.2356278
F	-0.0167210	-0.0072838	-6.5953549
F	0.4194317	2.3124923	-5.2410336

Table 3.15. Cartesian coordinates of the computed IPFB/DMAP complex at the B3LYP/6-311G** level of theory in Q-Chem 5.3.2 for ALMO-EDA.

IPFB/DMAP Complex			
0 1			
--			
0 1			
H	-1.4615043	-1.4467211	0.6671139
C	-0.8077534	-0.7991911	1.2443079
H	-1.5365448	-1.5212564	3.1073454
C	-0.8489941	-0.8399624	2.6264680
C	0.0028632	0.0045587	3.3761937
H	1.5414670	1.5300645	3.1013033
C	0.8532595	0.8475615	2.6230979
H	1.4621680	1.4500624	0.6613097
C	0.8095595	0.8037069	1.2411141
N	0.0041306	0.0060965	4.7435401
C	0.8979829	0.8933906	5.4735489
H	0.6982047	1.9469475	5.2467552
H	1.9497927	0.6871807	5.2447493
H	0.7516481	0.7462939	6.5418729
C	-0.8893486	-0.8785377	5.4772191
H	-0.7401600	-0.7299325	6.5449435
H	-0.6915109	-1.9326829	5.2516597
H	-1.9414994	-0.6713278	5.2507100
N	0.0002992	0.0014543	0.5382605
--			
0 1			
C	-0.0056633	-0.0114883	-7.2023568
C	-0.0033905	-0.0046248	-4.4001546
C	-1.2077207	-0.0048251	-6.5053830
C	1.1975193	-0.0145941	-6.5072930
C	1.1876287	-0.0111320	-5.1174601
C	-1.1955726	-0.0014478	-5.1155775
I	-0.0018818	-0.0017154	-2.2562640
F	-2.3745221	0.0044625	-4.4792240
F	2.3675829	-0.0141900	-4.4829578
F	2.3544308	-0.0214964	-7.1801099
F	-0.0067488	-0.0149794	-8.5383806
F	-2.3657218	-0.0016749	-7.1763518

Table 3.16. Cartesian coordinates of the computed IDNB/3-NPy complex at the B3LYP/6-311G** level of theory in Q-Chem 5.3.2 for ALMO-EDA.

IDNB/3-NPy Complex			
0 1			
--			
0 1			
H	2.1745615	-0.7411456	3.1613287
C	1.2936868	-0.4761815	3.7375379
H	2.1813936	-0.9259300	5.6476095
C	1.2974637	-0.5795703	5.1273224
C	0.1477308	-0.2313947	5.8243950
C	-0.9411791	0.2027788	5.0809324
H	-1.7246793	0.6181952	3.1197846
N	0.2368755	-0.0571193	3.0321277
H	0.0764749	-0.2872610	6.9021725
N	-2.1926093	0.5859875	5.7694983
O	-3.1204439	0.9685627	5.0730838
O	-2.2111187	0.4929413	6.9878122
C	-0.8708268	0.2801150	3.6937445
--			
0 1			
C	0.2218384	0.0144435	-4.9750301
C	0.2384515	0.0001957	-2.1613017
C	0.4738401	-1.1430222	-4.2547577
C	-0.0212212	1.1646335	-4.2401680
C	-0.0202885	1.1849127	-2.8496757
C	0.4889294	-1.1773491	-2.8645918
I	0.2487823	-0.0102647	-0.0279573
H	-0.2202556	2.1151780	-2.3371093
H	0.2151495	0.0200187	-6.0543365
H	0.6935959	-2.1129693	-2.3639063
N	-0.2940694	2.4299207	-4.9711151
O	-0.5273851	3.4242307	-4.3011324
O	-0.2656934	2.3879541	-6.1907321
N	0.7399904	-2.4003929	-5.0013628
O	0.6896314	-2.3483287	-6.2198282
O	0.9913743	-3.3991387	-4.3443446

Table 3.17. Cartesian coordinates of the computed IDNB/3-FPy complex at the B3LYP/6-311G** level of theory in Q-Chem 5.3.2 for ALMO-EDA.

IDNB/3-FPy			
0 1			
--			
0 1			
H	0.4748705	-2.0089259	3.5712417
C	0.2623094	-1.1176694	4.1523528
H	0.5041506	-2.0726707	6.0667278
C	0.2786431	-1.1510188	5.5444625
C	0.0021128	0.0162128	6.2493054
C	-0.2762784	1.1543471	5.5111285
H	-0.4965166	2.0098621	3.5490851
C	-0.2765994	1.1154534	4.1229983
N	-0.0096015	-0.0092224	3.4566052
H	0.0000211	0.0551983	7.3316760
F	-0.5479552	2.3128079	6.1381678
--			
0 1			
C	0.0081702	-0.0195833	-4.5092539
C	0.0000943	-0.0172292	-1.6933600
C	-1.1679451	0.0992104	-3.7847237
C	1.1801724	-0.1370756	-3.7778881
C	1.2038137	-0.1382201	-2.3874601
C	-1.1996468	0.1028267	-2.3943875
I	-0.0047803	-0.0173139	0.4420494
H	2.1524918	-0.2331528	-1.8785043
H	0.0112441	-0.0205743	-5.5885382
H	-2.1512499	0.1987171	-1.8910969
N	2.4653588	-0.2679124	-4.5125072
O	2.4148249	-0.2716238	-5.7323354
O	3.4846420	-0.3625360	-3.8457371
N	-2.4489402	0.2279095	-4.5270479
O	-3.4722249	0.3219059	-3.8663925
O	-2.3911815	0.2302774	-5.7465679

Table 3.18. Cartesian coordinates of the computed IDNB/PY complex at the B3LYP/6-311G** level of theory in Q-Chem 5.3.2 for ALMO-EDA.

IDNB/PY Complex			
0 1			
--			
0 1			
H	-1.9647561	-0.5795081	3.5413072
C	-1.0872542	-0.3201947	4.1260505
H	-2.0440289	-0.5986773	6.0322567
C	-1.1294864	-0.3302915	5.5174398
C	0.0227108	0.0101515	6.2198732
C	1.1680015	0.3459615	5.5041569
H	1.9841905	0.5820863	3.5185389
C	1.1123131	0.3267333	4.1133687
N	0.0091581	0.0011507	3.4319892
H	0.0280167	0.0136880	7.3039209
H	2.0875367	0.6174346	6.0083444
--			
0 1			
C	-0.0149750	-0.0048986	-4.4862692
C	-0.0055202	-0.0031925	-1.6690610
C	0.1271766	1.1671512	-3.7592890
C	-0.1518854	-1.1761250	-3.7569600
C	-0.1500061	-1.2025074	-2.3664974
C	0.1346356	1.1952467	-2.3688654
I	-0.0009230	-0.0019781	0.4696660
H	-0.2610620	-2.1504824	-1.8593926
H	-0.0189423	-0.0055078	-5.5655117
H	0.2489270	2.1438769	-1.8637111
N	-0.3075214	-2.4568584	-4.4939990
O	-0.3125551	-2.4040534	-5.7138975
O	-0.4195340	-3.4759464	-3.8294628
N	0.2775607	2.4470358	-4.4988985
O	0.3947970	3.4668435	-3.8363603
O	0.2734262	2.3928614	-5.7187367

Table 3.19. Cartesian coordinates of the computed IDNB/DMAP complex at the B3LYP/6-311G** level of theory in Q-Chem 5.3.2 for ALMO-EDA.

IDNB/DMAP Complex			
0 1			
--			
0 1			
H	-1.4512180	-1.4552438	1.5586304
C	-0.8013190	-0.8031140	2.1352520
H	-1.5380472	-1.5169420	3.9999052
C	-0.8504746	-0.8367460	3.5178075
C	-0.0041821	0.0133738	4.2671819
H	1.5403378	1.5318052	3.9937924
C	0.8526239	0.8497875	3.5144662
H	1.4722944	1.4410483	1.5529188
C	0.8153117	0.7983043	2.1320965
N	-0.0135550	0.0256760	5.6349042
C	0.8989235	0.8931254	6.3656795
H	0.7363857	1.9478216	6.1178442
H	1.9487142	0.6509528	6.1605068
H	0.7281622	0.7706816	7.4334539
C	-0.8900865	-0.8752120	6.3691703
N	0.0096328	-0.0065868	1.4277682
H	-1.9431842	-0.7017359	6.1219990
H	-0.6596768	-1.9281589	6.1666314
H	-0.7645619	-0.7028713	7.4363370
--			
0 1			
C	-0.0086380	-0.0075077	-6.3989625
C	0.0005041	-0.0041593	-3.5785044
C	-1.1861173	-0.0039610	-5.6665766
C	1.1735046	-0.0096072	-5.6741453
C	1.2045793	-0.0083061	-4.2835802
C	-1.2081251	-0.0020407	-4.2758932
I	0.0064295	0.0005486	-1.4336832
H	-0.0121338	-0.0084749	-7.4780813
H	2.1612965	-0.0103718	-3.7806585
H	-2.1615342	0.0014887	-3.7666996
N	-2.4771462	-0.0014469	-6.4009900
O	-3.5018828	-0.0004089	-5.7353061
O	-2.4284722	-0.0006163	-7.6214733
N	2.4597334	-0.0128936	-6.4169065
O	2.4031771	-0.0146993	-7.6370475
O	3.4887442	-0.0135093	-5.7578373

3.6 References

[1] R. Wilcken, M. O. Zimmermann, A. Lange, A. C. Joerger, F. M. Boeckler, *J. Med. Chem.* **2013**, *56*, 1363–1388.

[2] T. M. Beale, M. G. Chudzinski, M. G. Sarwar, M. S. Taylor, *Chem. Soc. Rev.* **2013**, 42, 1667–1680.

[3] J. Heidrich, T. E. Exner, F. M. Boeckler, *J. Chem. Inf. Model*. **2019**, *59*, 636–643.

[4] P. Metrangolo, F. Meyer, T. Pilati, G. Resnati, G. Terraneo, *Angew. Chem. Int. Ed.* **2008**, *47*, 6114–6127.

[5] M. Erdélyi, *Chem. Soc. Rev*. **2012**, *41*, 3547-3557.

[6] T. Clark, M. Hennemann, J. S. Murray, P. Politzer, *J. Mol. Model*. **2007**, *13*, 291–296.

[7] P. Politzer, J. S. Murray, T. Clark, *Phys. Chem. Chem. Phys*. **2010**, *12*, 7748-7757.

[8] G. Cavallo, P. Metrangolo, R. Milani, T. Pilati, A. Priimagi, G. Resnati, G. Terraneo, *Chem. Rev*. **2016**, *116*, 2478–2601.

[9] P. Politzer, J. S. Murray, T. Clark, *Phys. Chem. Chem. Phys*. **2013**, *15*, 11178-11189.

[10] J. S. Murray, P. Lane, P. Politzer, *J. Mol. Model*. **2009**, *15*, 723–729.

[11] H. Fan, J. K. Eliason, C. D. Moliva A., J. L. Olson, S. M. Flancher, M. W. Gealy, D. J. Ulness, *J. Phys. Chem*. **A 2009**, *113*, 14052–14059.

[12] B. Hawthorne, H. Fan-Hagenstein, E. Wood, J. Smith, T. Hanks, Int. *J. Spectrosc*. **2013**, *2013*, 1–10.

[13] C. Präsang, A. C. Whitwood, D. W. Bruce, *Cryst. Growth Des*. **2009**, *9*, 5319-5326.

[14] A. Siiskonen, A. Priimagi, *J. Mol. Model*. **2017**, *23*, 50.

[15] L. P. Wolters, P. Schyman, M. J. Pavan, W. L. Jorgensen, F. M. Bickelhaupt, S. Kozuch, *Wiley Interdiscip. Rev. Comput. Mol. Sci*. **2014**, *4*, 523–540.

[16] D. Musumeci, C. A. Hunter, R. Prohens, S. Scuderi, J. F. McCabe, *Chem. Sci*. **2011**, *2*, 883-890.

[17] J. S. Murray, P. Politzer, *Wiley Interdiscip. Rev. Comput. Mol. Sci*. **2011**, *1*, 153–163.

[18] J. S. Murray, P. Politzer, *J. Mol. Struct: THEOCHEM* **1998**, *425*, 107–114.

[19] K. B. Landenberger, A. J. Matzger, *Cryst. Growth Des*. **2010**, *10*, 5341–5347.

[20] P. Politzer, J. S. Murray, T. Clark, G. Resnati, *Phys. Chem. Chem. Phys*. **2017**, *19*, 32166–32178.

[21] N. R. Goud, O. Bolton, E. C. Burgess, A. J. Matzger, *Cryst. Growth Des*. **2016**, *16*, 1765–1771.

[22] M. D. Perera, J. Desper, A. S. Sinha, C. B. Aakeröy, *CrystEngComm* **2016**, *18*, 8631–8636.

[23] C. A. Gunawardana, C. B. Aakeröy, *Chem. Commun*. **2018**, *54*, 14047–14060.

[24] A. Bauzá, D. Quiñonero, A. Frontera, P. M. Deyá, *Phys. Chem. Chem. Phys*. **2011**, *13*, 20371–20379.

[25] R. A. Wiscons, V. Coropceanu, A. J. Matzger, *Chem. Mater*. **2019**, *31*, 6598–6604.

[26] J. Yang, B. Hong, N. Wang, X. Li, X. Huang, Y. Bao, C. Xie, H. Hao, *CrystEngComm* **2019**, *21*, 6374–6381.

[27] C. B. Aakeröy, T. K. Wijethunga, J. Desper, *J. Mol. Struct*. **2014**, *1072*, 20–27.

[28] B. A. DeHaven, A. L. Chen, E. A. Shimizu, S. R. Salpage, M. D. Smith, L. S. Shimizu, *Cryst. Growth Des*. **2019**, *19*, 5776–5783.

[29] C. B. Aakeröy, T. K. Wijethunga, J. Desper, M. Đaković, *Cryst. Growth Des*. **2016**, *16*, 2662–2670.

[30] C. B. Aakeröy, P. D. Chopade, J. Desper, *Cryst. Growth Des*. **2013**, *13*, 4145–4150.

[31] T. Clark, *WIREs Comp Mol Sci*. **2013**, *3*, 13–20.

[32] G. R. Desiraju, P. S. Ho, L. Kloo, A. C. Legon, R. Marquardt, P. Metrangolo, P. Politzer, G. Resnati, K. Rissanen, *Pure Appl. Chem*. **2013**, *85*, 1711–1713.

[33] A. J. Stone, *J. Am. Chem. Soc*. **2013**, *135*, 7005–7009.

[34] S. Kozuch, J. M. L. Martin, *J. Chem. Theory Comput*. **2013**, *9*, 1918-1931.

[35] Y. Lu, H. Li, X. Zhu, H. Liu, W. Zhu, *Int. J. Quantum Chem*. **2012**, *112*, 1421-1430.

[36] Y. Shao, Z. Gan, E. Epifanovsky, A. T. B. Gilbert, M. Wormit, J. Kussmann, A. W. Lange, A. Behn, J. Deng, X. Feng, D. Ghosh, M. Goldey, P. R. Horn, L. D. Jacobson, I. Kaliman, R. Z. Khaliullin, T. Kuś, A. Landau, J. Liu, E. I. Proynov, Y. M. Rhee, R. M. Richard, M. A. Rohrdanz, R. P. Steele, E. J. Sundstrom, H. L. W. III, P. M. Zimmerman, D. Zuev, B. Albrecht, E. Alguire, B. Austin, G. J. O. Beran, Y. A. Bernard, E. Berquist, K. Brandhorst, K. B. Bravaya, S. T. Brown, D. Casanova, C.-M. Chang, Y. Chen, S. H. Chien, K. D. Closser, D. L. Crittenden, M. Diedenhofen, R. A. D. Jr, H. Do, A. D. Dutoi, R. G. Edgar, S. Fatehi, L. Fusti-Molnar, A. Ghysels, A. Golubeva-Zadorozhnaya, J. Gomes, M. W. D. Hanson-Heine, P. H. P. Harbach, A. W. Hauser, E. G. Hohenstein, Z. C. Holden, T.-C. Jagau, H. Ji, B. Kaduk, K. Khistyaev, J. Kim, J. Kim, R. A. King, P. Klunzinger, D. Kosenkov, T. Kowalczyk, C. M. Krauter, K. U. Lao, A. D. Laurent, K. V. Lawler, S. V. Levchenko, C. Y. Lin, F. Liu, E. Livshits, R. C. Lochan, A. Luenser, P. Manohar, S. F. Manzer, S.-P. Mao, N. Mardirossian, A. V. Marenich, S. A. Maurer, N. J. Mayhall, E. Neuscamman, C. M. Oana, R. Olivares-Amaya, D. P. O'Neill, J. A. Parkhill, T. M. Perrine, R. Peverati, A. Prociuk, D. R. Rehn, E. Rosta, N. J. Russ, S. M. Sharada, S. Sharma, D. W. Small, A. Sodt, T. Stein, D. Stück, Y.-C. Su, A. J. W. Thom, T. Tsuchimochi, V. Vanovschi, L. Vogt, O. Vydrov, T. Wang, M. A. Watson, J. Wenzel, A. White, C. F. Williams, J. Yang, S. Yeganeh, S. R. Yost, Z.-Q. You, I. Y. Zhang, X. Zhang, Y. Zhao, B. R. Brooks, G. K. L. Chan, D. M. Chipman, C. J. Cramer, W. A. G. III, M. S. Gordon, W. J. Hehre, A. Klamt, H. F. S. III, M. W. Schmidt, C.

D. Sherrill, D. G. Truhlar, A. Warshel, X. Xu, A. Aspuru-Guzik, R. Baer, A. T. Bell, N. A. Besley, J.-D. Chai, A. Dreuw, B. D. Dunietz, T. R. Furlani, S. R. Gwaltney, C.-P. Hsu, Y. Jung, J. Kong, D. S. Lambrecht, W. Liang, C. Ochsenfeld, V. A. Rassolov, L. V. Slipchenko, J. E. Subotnik, T. V. Voorhis, J. M. Herbert, A. I. Krylov, P. M. W. Gill, M. Head-Gordon, *Mol. Phys.* **2015**, *113*, 184–215.

[37] J. Thirman, E. Engelage, S. M. Huber, M. Head-Gordon, *Phys. Chem. Chem. Phys.* **2018**, *20*, 905-915.

Chapter 4

Synthesis and Characterization of Strongly Polarized Haloarenes for Multicomponent Crystal Design

4.1 Introduction

Design strategies that support stabilization of multicomponent crystals through halogen bonds (XBs) have emphasized the utility of halogen bonding interactions to produce strong, tunable, and directional assemblies.[1] Halogen bonding interactions most commonly feature polarizable halogen atoms (Cl < Br < I)[2] covalently bound in a molecule (**Figure 4.1**) with substituents that decrease electron density around the halogen by increasing the degree of electron withdrawing groups (EWGs) that are attached to the halogenated species.[3,4] This produces an electropositive region along the axis of the covalently bound halogen (i.e. σ-hole)[5], as shown in **Figure 4.1**, which contributes to the attractive interaction that has been shown to form between halogen atoms and Lewis bases (LBs) or halogen bond (XB) donors and acceptors.[6,7] The development of halogenated multicomponent crystals has acquired substantial attention due to diverse applications within supramolecular chemistry and crystal engineering.[8,9] Specifically in the case of crystal engineering of energetic materials[10], compounds that upon decomposition release energy in the form of heat and gaseous byproducts, halogens have been incorporated to promote interaction specificity that is both predictable and facile to establish[11]; often time this is not afforded by hydrogen bonding due to the insufficient number of traditional hydrogen bond (HB) donors and acceptors found among energetics.[12]

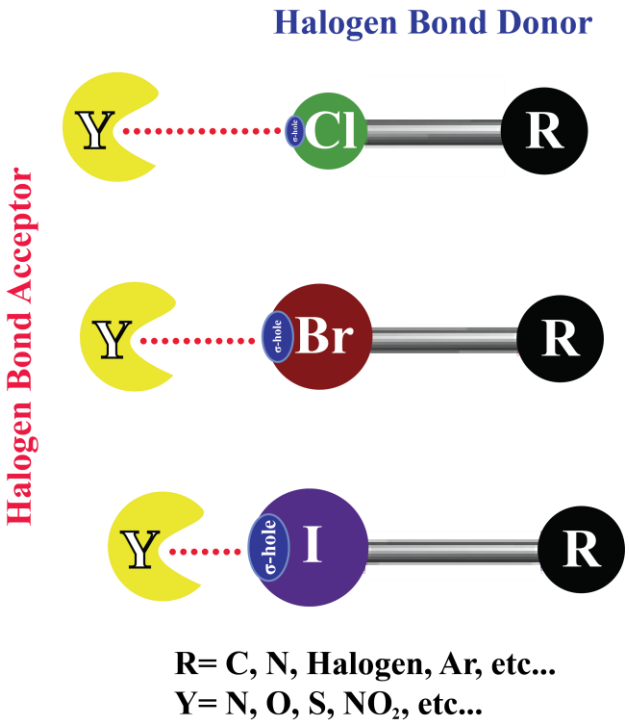


Figure 4.1. Illustration of halogen bonding interactions between chlorinated, brominated, and iodinated complexes (Cl-R, Br-R, and I-R, respectively) and a halogen bond acceptor denoted as Y.

In recent years, various studies have demonstrated the utility of halogenated motifs within energetic multicomponent crystals like cocrystals, which are formed when two or more neutral molecular species interact in a way that alters the physical properties of the pure components, to access new assemblies with distinct characteristics from the two pure starting components.[13] An example of how cocrystallization of a halogenated compound with an energetic can produce a new crystalline species with greater stability than its two components include the cocrystal[12] formed between 1,3,5-iodo-2,4,6-trinitrobenzene (TITNB), which currently has the largest known σ-hole, and the coformer 1,3,5-trinitrobenzene (TNB) in **Figure 4.2**. The interactions that facilitate the formation of the TITNB/TNB cocrystal are halogen bonding and hydrogen bonding.

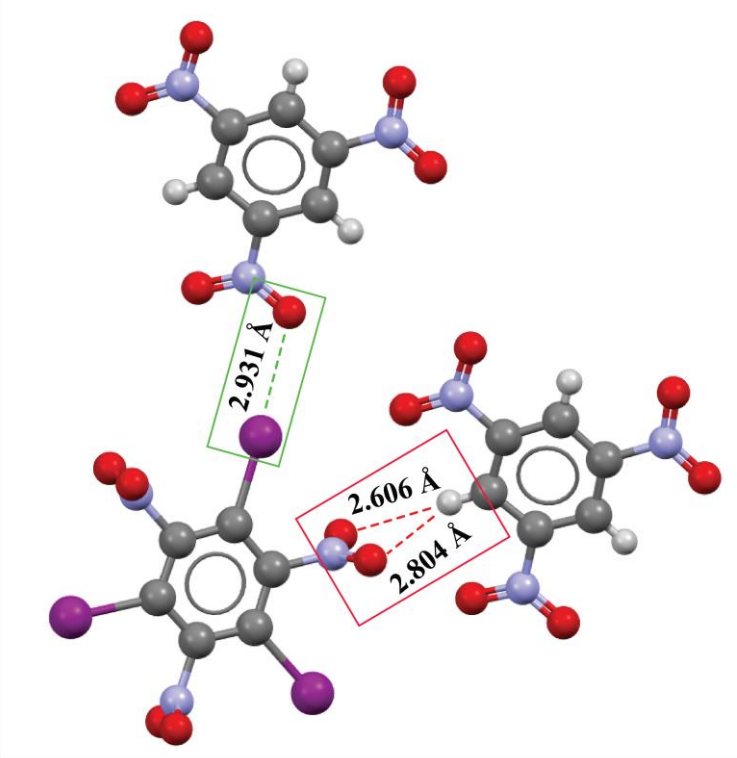


Figure 4.2. Halogen and hydrogen bonding interactions within TITNB/TNB cocrystal.

Key features that are directly related to the formation of these cocrystals are the attributes of the XB donor and acceptor: 1) TITNB is aromatic XB donor containing nitro-groups that enhance the σ-hole of the iodine atoms and 2) TNB is an aromatic XB acceptor composed of nitro-group substituents that act as nucleophiles to the iodine atoms of TITNB. Computational modeling of the XB donor/acceptor complex formed with TITNB demonstrated that both the polarizability of the halogen atom and the nucleophilic nature of the coformer play roles that support the formation and stabilization of the cocrystal.

Computational analysis of electrostatic potentials (ESPs) has shown that nitro-groups along with oxygen atoms, *N*-oxide and pyridyl-groups are complementary synthons[14,15] to strongly polarized halogen atoms like the iodine atoms found in TITNB, which have favorable implications toward cocrystal formation. The strongest predicted halogen bonding interaction among the

functionalities mentioned above and TITNB occurs with pyridyl-groups. Notability, the strength of the XB donor can be modulated to increase the attraction to a weaker XB acceptor.[16] Herein, we hypothesize that the synthesis of 1-iodo-2,3,4,5,6-pentanitrobenzene (IPNB), a more polarized XB donor than TITNB, would result in a σ-hole magnitude (quantified by a maximum ESP value or $V_{s,max}$ on an ESP map in **Figure 4.3**) far greater than TITNB and thus would form stronger halogen bonding interactions within a cocrystal formed with the same XB acceptors. The $V_{s,max}$ values of TITNB and IPNB, as shown in **Figure 4.3**, are 48.42 and 59.15 kcal mol^{-1}, respectively.

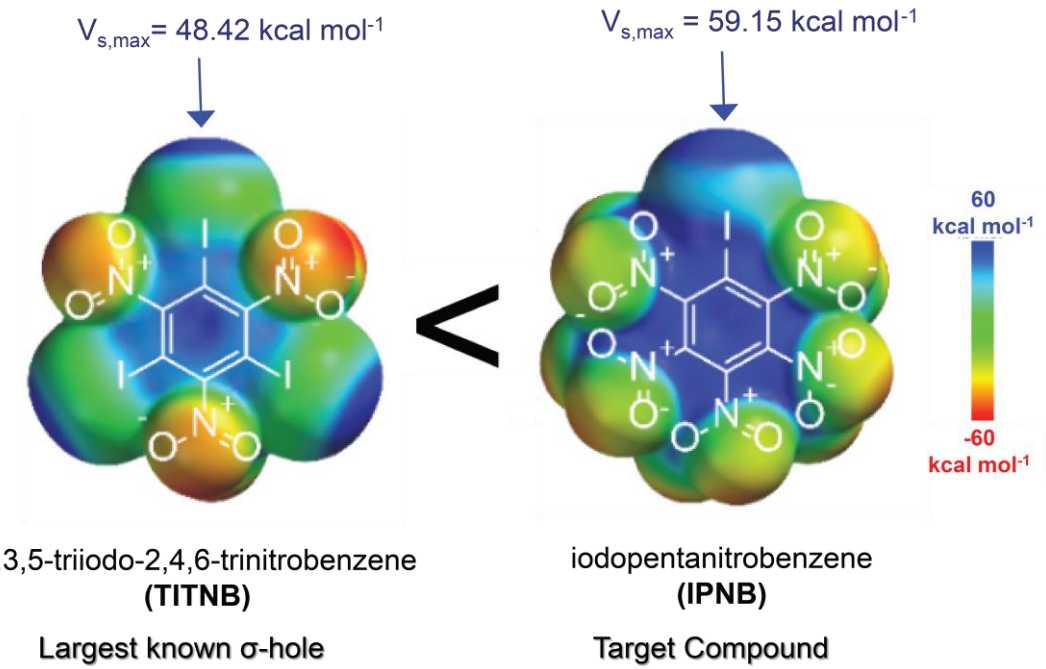


Figure 4.3. ESP maps of TITNB and IPNB calculated at B3LYP/6-311G** level of theory Spartan '18 software along with their corresponding $V_{s,max}$ values.

Cocrystals of IPNB would become the new standard toward the design of halogenated energetic complexes. Moreover, in utilizing computed ESP maps to predict the formation of highly polarized halogen bonded multicomponent crystals, opportunities arise for the predictions to be experimentally tested and translated from gas phase models to solution and solid-state; thus, the accuracy of the predictions can be evaluated.

4.2 Results and Discussion

4.2.1 ESP predictions

Gas phase prediction models based on ESPs (i.e. $V_{s,max}$ values) were utilized to quantify the extent at which IPNB interacts as a stronger XB donor than TITNB. When comparing the $V_{s,max}$ values of IPNB and TITNB, IPNB is calculated to outcompete TITNB by 10.8 kcal mol^{-1} as a XB donor. The scope for suitable XB acceptors for IPNB was defined using coformers of TITNB (i.e. diacetone diperoxide (DADP)[17], 1,4-dithiane (DT)[13], and 4-ethylaminomethyl pyridine (EAMP)[13]) which provided a base range of $V_{s,min}$ values (between -25.74 to -48.16 kcal mol^{-1}) to select diverse XB acceptors from.

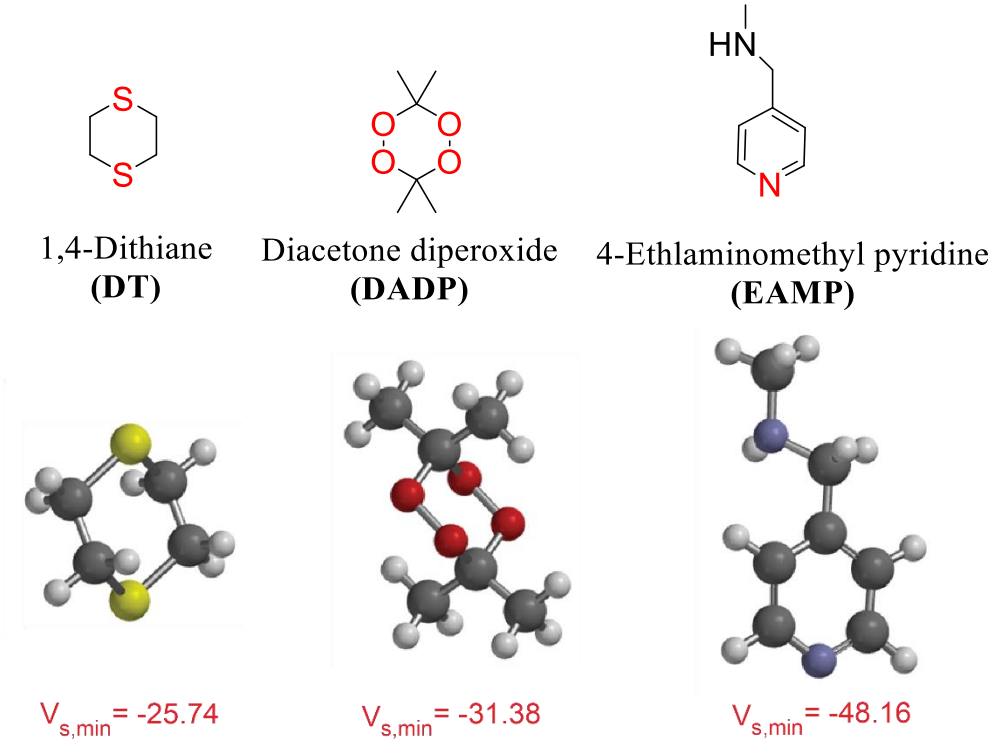


Figure 4.4. Three TITNB coformers and their $V_{s,min}$ values in kcal mol^{-1} calculated at B3LYP/6-311G** level.

Previous studies have shown that pyridyl-groups interact predictably well with TITNB; thus pyridine derivatives are an attractive pairing for IPNB. Four diverse XB acceptors (**Figure**

4.4), which include aromatic and aliphatic compounds, were chosen due to their range of $V_{s,min}$ values (**Table 4.1**) and varying structural sizes. **Figure 4.4** shows the strength of the XB acceptor ranked from weakest to strongest in the following way: hexamethylenetetramine (HMTA)<4,4'-bipyridine (4,4'-BIPY)< 4-picoline *N*-oxide (4-PICO) < 4-dimethylaminopyridine (DMAP). **Table 4.1** shows the $V_{s,max}$ and $V_{s,min}$ values of TITNB and IPNB along with the four XB acceptors, respectively.

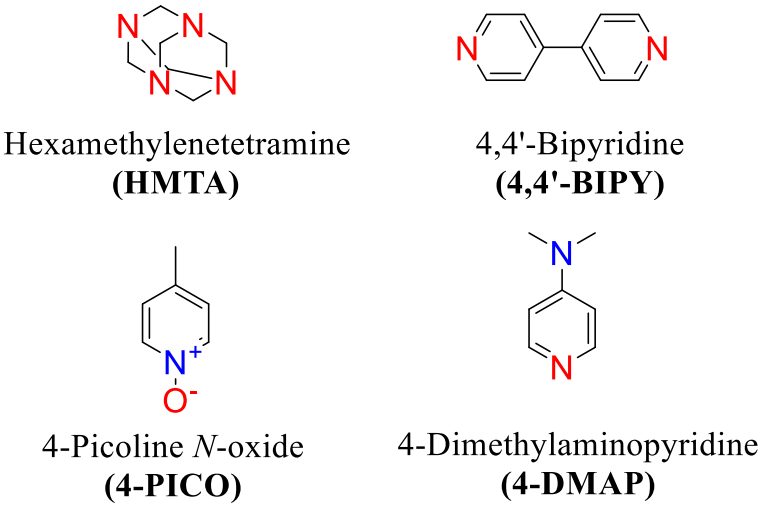


Figure 4.5. Four target XB acceptors.

Table 4.1 ESP values for the XB donors ($V_{,max}$) and acceptors ($V_{s,min}$) in kcal mol^{-1} calculated at B3LYP/6-311G** level.

XB Donors	$V_{s,max}$	XB Acceptor	$V_{s,min}$
TITNB	48.42	Hexamethylenetetramine (HMTA)	-37.64
IPNB	59.15	4,4'-Bipyridine (4,4'-BIPY)	-42.71
		4-Picoline *N*-oxide (4-PICO)	-49.45
		4-Dimethylaminopyridine (DMAP)	-53.37

In regards to halogen bond complexes, both the $V_{s,max}$ values of the XB donors and the energy difference between the XB donors ($V_{s,max}$) TITNB or IPNB and an acceptor ($V_{s,min}$) denoted as ΔV_s were compared to determine interaction propensity (**Tables 4.1** and **4.2**). ΔV_s calculations are commonly used to suggest how well donors and acceptors interact. The ΔV_s values of IPNB/acceptor complexes suggest that IPNB interacts more strongly (at an average of 10.73 ± 5.37 kcal mol^{-1}) than TITNB in TITNB/acceptor complexes.

Table 4.2. ΔV_s values of halogen bond donor/acceptor complexes for TITNB and IPNB in kcal mol^{-1} calculated at B3LYP/6-311G** level.

	XB Donors	
XB Acceptors	TITNB	IPNB
HMTA	86.07	96.80
4,4'-BIPY	91.13	101.86
4-PICO	97.87	108.60
DMAP	101.79	112.52

4.2.2 Synthesis of IPNB

The synthesis of IPNB was based on the previously reported studies by Atkins et al.[18] and Nielson et al.[19,20], on polynitrobenzenes. Due to the energetic nature of the precursors of IPNB, safety precautions were taken to ensure unintentional detonations did not occur. The small-scale synthesis of the IPNB precursors, starting from the commercially available 3,5-dinitroaniline, were performed behind a blast shield throughout the duration of each experiment. Each reaction step, illustrated by **Figure 4.6a-c**, was optimized to increase the overall yields of the reactions from the reported syntheses; optimized reaction conditions can be found in the **4.4.2 General Methods Section: Reaction Conditions for IPNB Synthesis**.

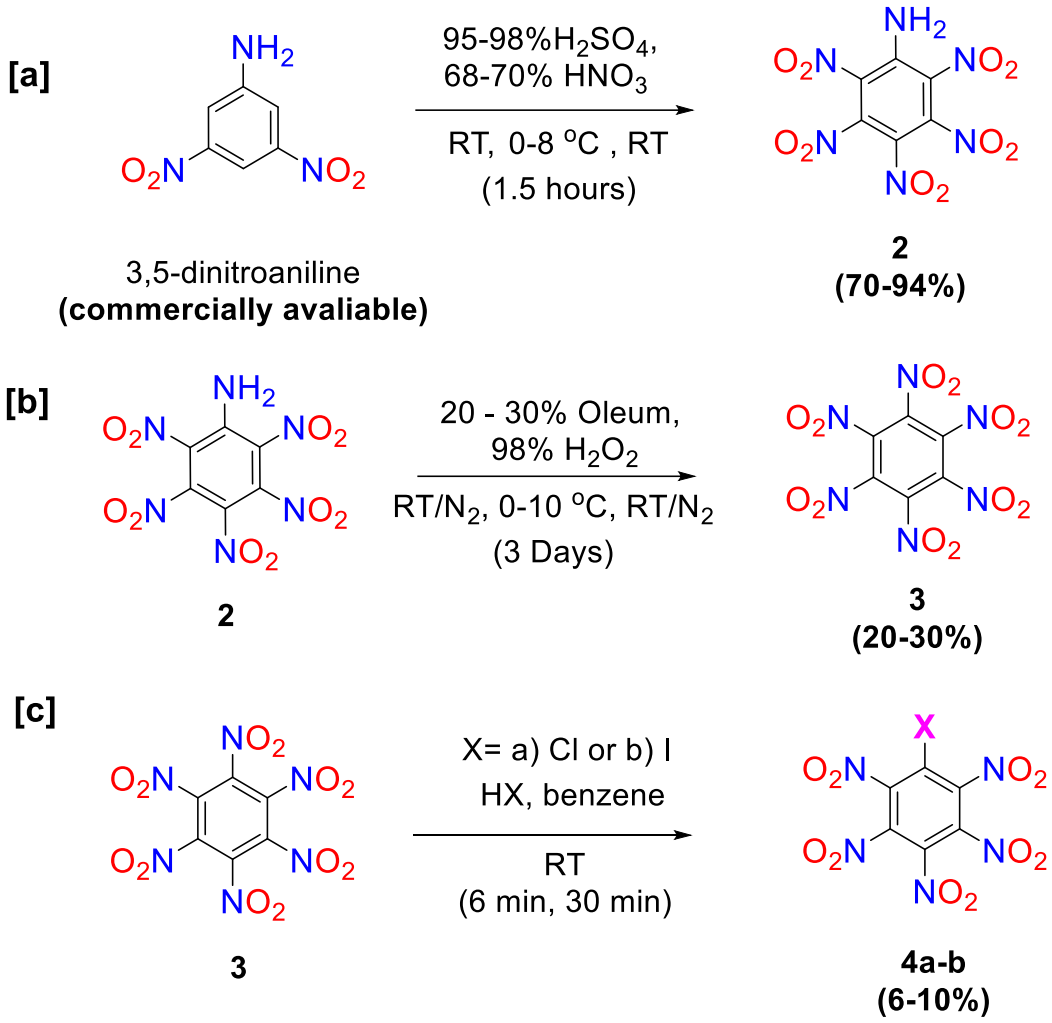


Figure 4.6a-c. Optimized synthetic approach to access halopentanitrobenzene derivatives (chloro or iodo). (**a**) Nitration of 3,5-dinitroaniline to pentanitroaniline, (**b**) oxidation of pentanitroaniline to hexanitrobenzene, and (**c**) halogenation of hexanitrobenzene to halopentanitrobenzenes (X=Cl or I).

Notably, the recrystallization of precursor pentanitroaniline (PNA), as compound **2** in **Figure 4.6a**, led to the discovery of the first non-solvated form of PNA (**Figure 4.7**). According to SciFinder, the only known form of PNA exists in a solvate with 1,2-dichloroethylene (DCE).[21] Upon isolation, compound **2** was characterized via FT-IR (**Figure 4.16** in the **Additional Figures** section), and SC-XRD (**Figure 4.7**). Thermal analysis was conducted using a Q10 DSC instrument and the DSC curve of PNA is shown in **Figure 4.18** of the **Additional Figures** section. See **Table**

4.5 in the **Additional Tables** section for full crystallographic information of PNA. The analysis of the crystal structure revealed that compound **2** contains both amine $H_2N\cdots O_2N$ (nitro-group) intra and intermolecular interactions at 2.651 and 3.120 Å as well as $NO_2\cdots\pi$ interactions at 3.090 Å, respectively.

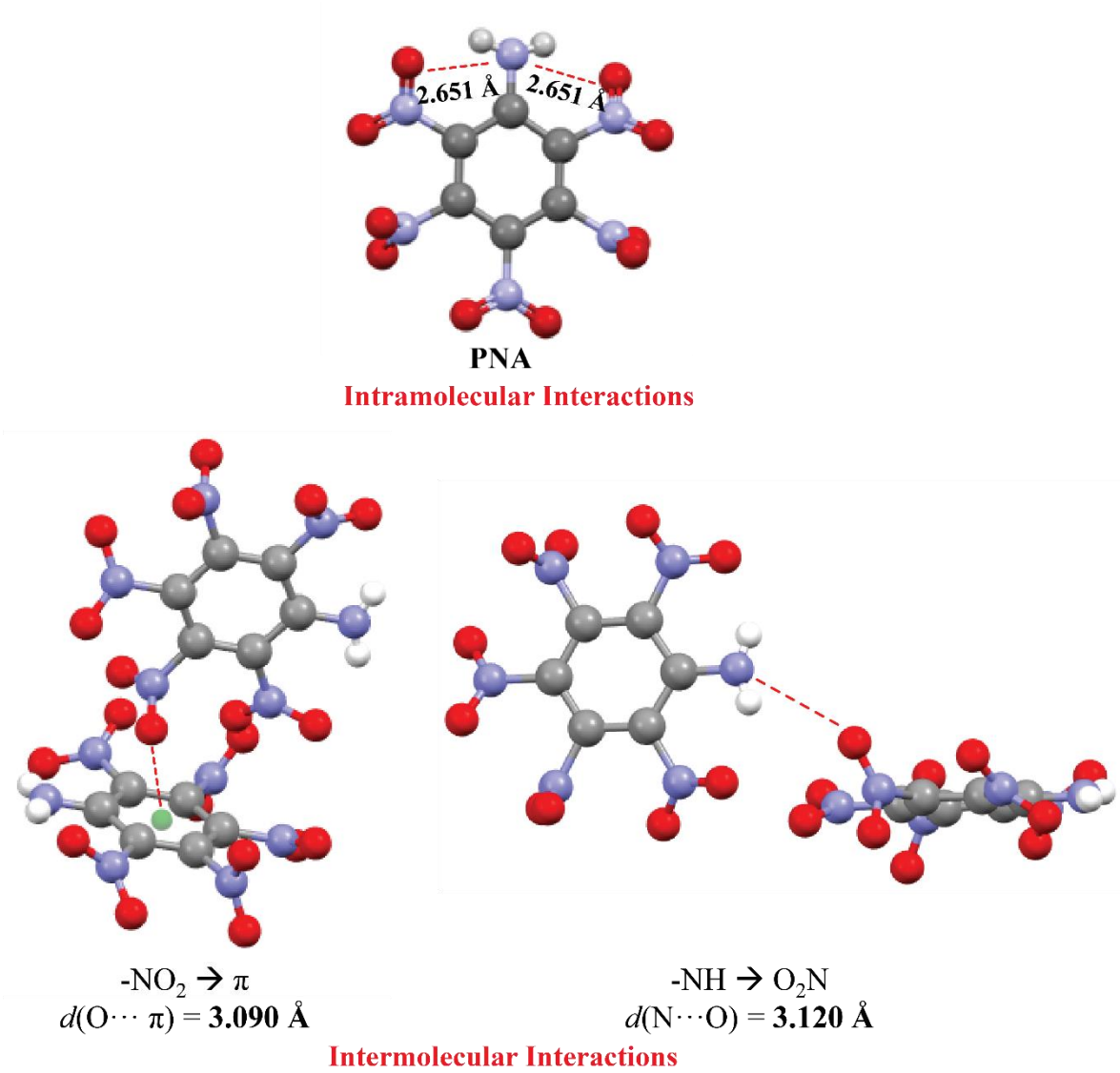


Figure 4.7. First reported non-solvated structure of PNA with intra-and intermolecular interactions.

The oxidation of the sp^3-hybridized amine to a nitro-group in compound **2** was conducted in fuming sulfuric acid and 98% H_2O_2 which produced in situ Caro's acid and resulted in HNB (compound **3**) in **Figure 4.6b**. Compound **3** (**HNB**) was characterized by FT-IR and Raman **Figures 4.16** and **4.17**, respectively, in the **Additional Figures** section as well as SC-XRD (**Figure 4.8**). **Figure 4.8** shows a molecule of compound **2**, which when viewed perpendicular to the *a*- and *c*-axes, the benzene ring is co-planar with the C-N bonds and the stericly hindered nitro-groups twisted out of the plane. In comparison to the known structure of HNB found in the Cambridge Structural Database (CSD)[22] with Ref code HNOBEN[23], compound **3** has a different space group and has more molecules per asymmetric unit (see **Table 4.6** in the **Additional Tables** section for full crystallographic information of HNB). When using the "structure overlay" feature in Mercury 2020.2.0, the two structures display the same packing (**Figure 4.9**). Thermal analysis was conducted using a Q10 DSC instrument and DSC curve of HNB shown in **Figure 4.19** in the **Additional Figures** section.

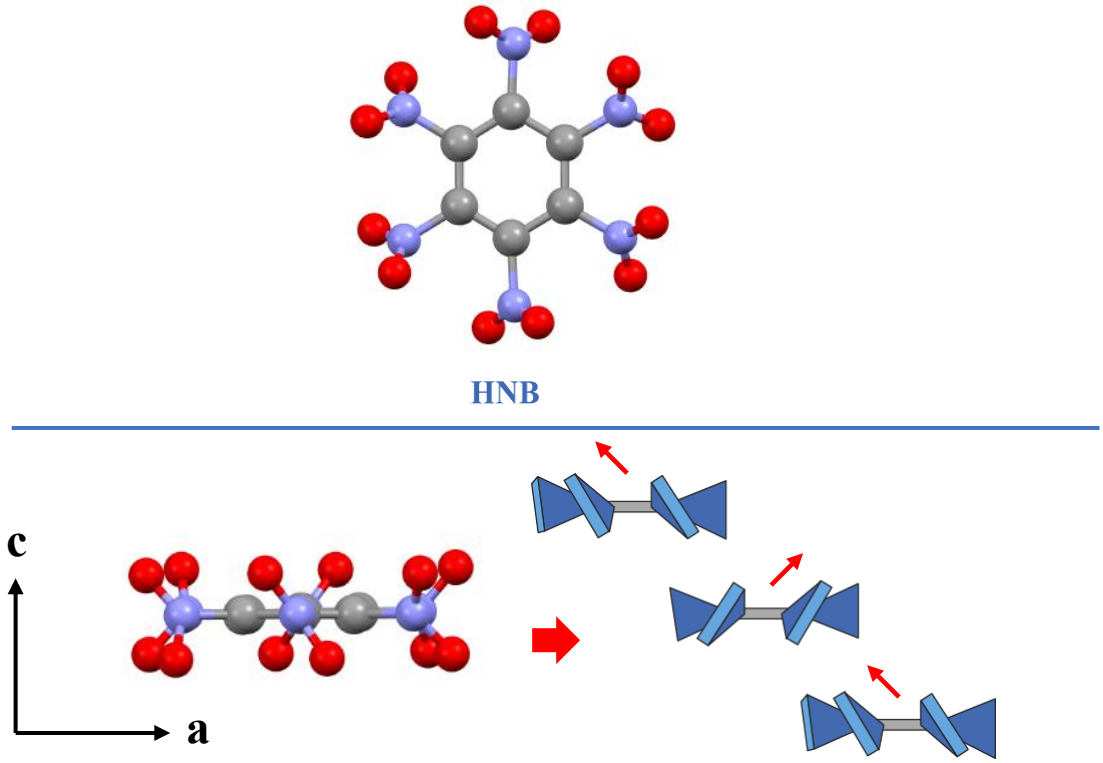


Figure 4.8. Illustration of a HNB molecule with a view of the benzene ring that is perpendicular to the a- and c-axes. The sterically hindered nitro-groups are denoted as rotated around the C-N bonds.

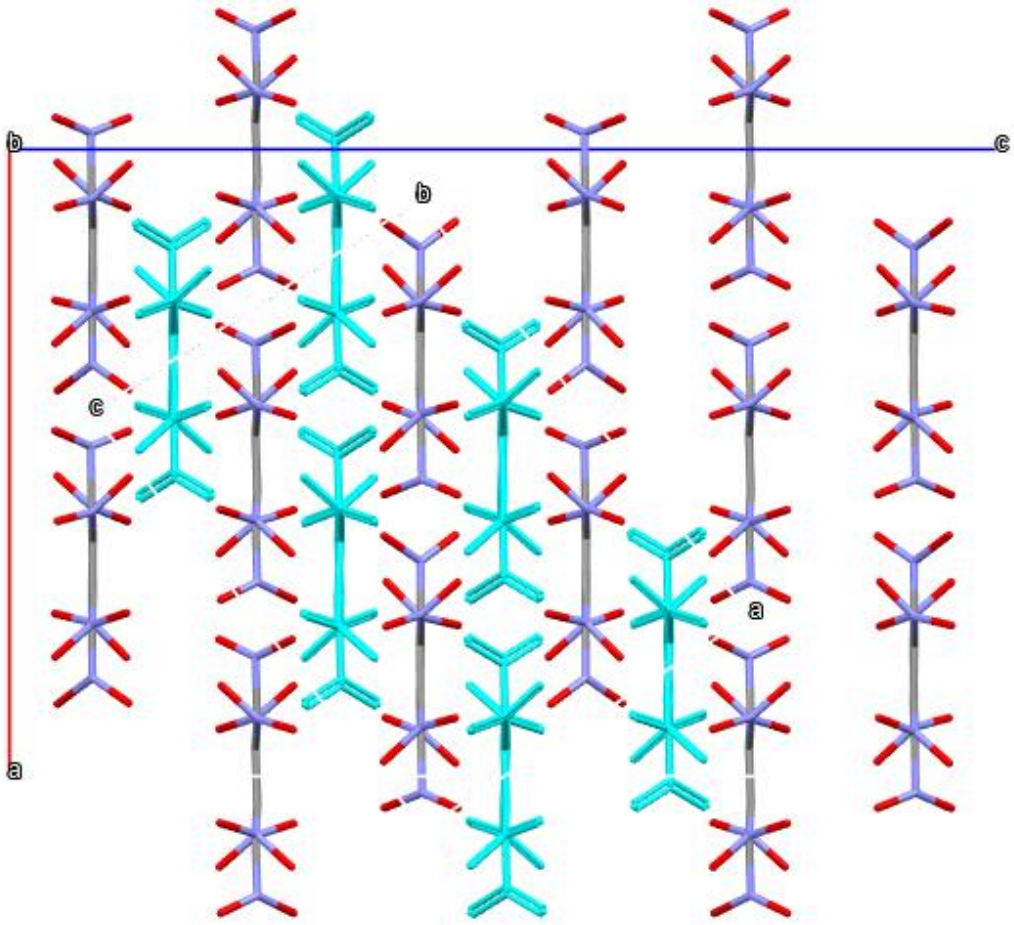


Figure 4.9. Illustration of the similarities in the crystal structures of HNOBEN (blue) and compound **2** (colored by element) with cell axes shown.

The HNOBEN structure was reported to refine poorly with a 19% R-factor, a measure of the agreement between the crystallographic model and the experimental X-ray diffraction data; the poor refinemen could be contributed to by the twisting of the nitro-groups about the carbon to nitrogen C-N bond and out of the aromatic plane.[24] The halogenation of compound **3**, upon exposure to strong halogenated acids (i.e. HCl and HI as denoted in **Figure 4.6c**), produced compounds **4** (CPNB) and **5** (IPNB)**.** Both were characterized, for the first time, via SC-XRD (**Figure 4.10** and **4.11**).

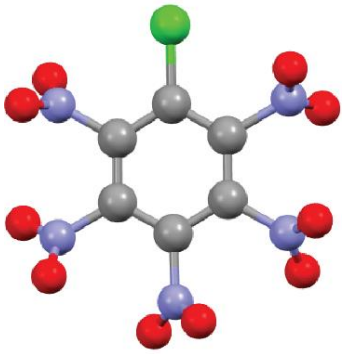


Figure 4.10. Experimental structure of compound **4** (CPNB) from crystallography.

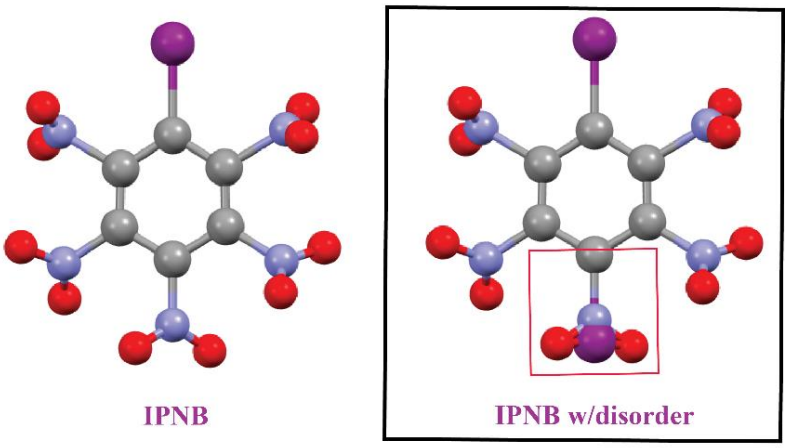
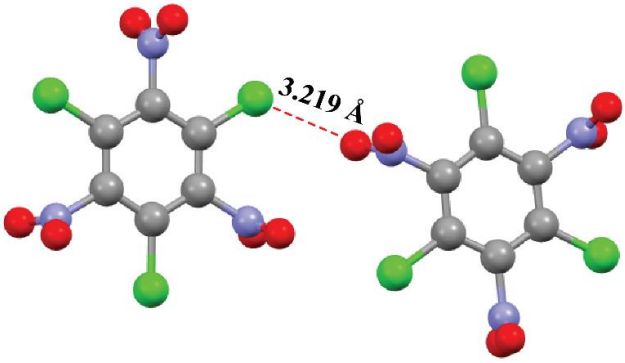


Figure 4.11. Experimental structure of compound **5** (IPNB) from crystallography without and with disorder highlighted by a red box.

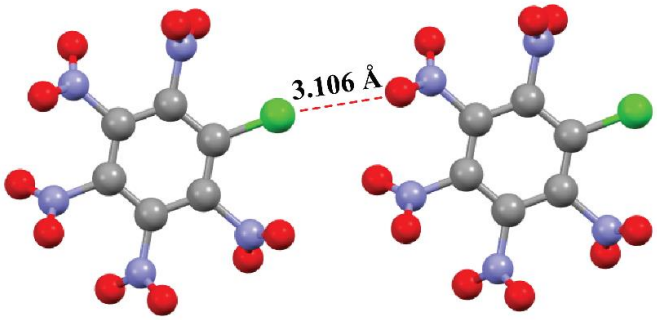
Literature precedence for 1,3,5-chloro-2,4,6-trinitrobenzene (TCTNB) with Ref code WANMON[25], a strong halogen bond donor, shows strong chlorine to nitro-group (i.e. Cl···O_2N) interactions within the dimer molecule. When comparing dimers of compound **4** to TCTNB dimers (**Figure 4.12**), there is a similar intermolecular halogen bonding interaction occurring. However, compound **4** has a shorter Cl···O_2N interaction distance at 3.106 (Å) than TCTNB at 3.219 (Å); this difference in interaction distance suggests that the halogen bond donor strength of compound **4** is stronger than TCTNB with a nitro-group acting as a halogen bond acceptor.



TCTNB dimer

-Cl → O_2N

d(Cl···O_2N) = **3.219 Å**



CPNB dimer

-Cl → O_2N

d(Cl···O_2N) = **3.106 Å**

Figure 4.12. Comparison of halogen bonding interactions between TCTNB and CPNB dimers.

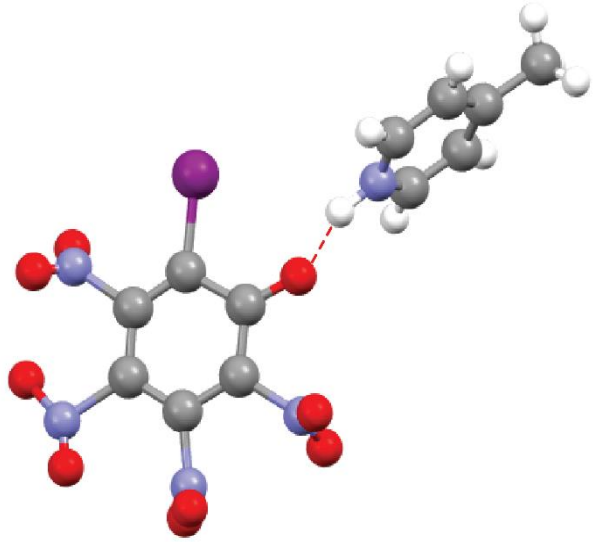
With regard to the crystal structure of compound **5** (IPNB), illustrated by **Figure 4.11**, there is a 180° rotational disorder which shortens the carbon to iodine C-I bonds due to averaging with the carbon to nitrogen C-N bonds making interpretation unreliable.

4.2.3 Cocrystallization of IPNB

Once the optimized synthetic route for compound **5** was established, cocrystallization conditions using vapor diffusion crystallization were screened in order to produce halogen bonded complexes between compound **5** and the halogen bond acceptors shown in **Figure 4.5**. The criteria for vapor diffusion crystallization solvent/precipitant combination were as follows: 1) both compound **2** and the acceptors need to be easily solubilized in the solvent and less so in the precipitant with a low boiling point and 2) the combination should result in a weaker halogen bond acceptor than the ones mentioned above, which would make the predicted halogen bonding interaction the dominant force that drives that formation of the complexes. Vapor diffusion crystallization with ethyl acetate (solvent) and hexane (precipitant) was found to be the optimal technique because it did not require tedious sample preparation and enabled small quantities of sample to form high quality crystalline materials. The cocrystallization conditions of compound **5** with HMTA, 4,4'-BIPY, 4-PICO, and DMAP involved dissolving compound **5** and a halogen bond acceptor in an organic solvent (i.e. ethyl acetate or EtOAc) inside a 4 mL vial then adding the vial in a capped 20 mL with hexane between 1-3 days. See **4.4.3 General Methods: Cocrystallization of IPNB** for all full details on cocrystallization conditions.

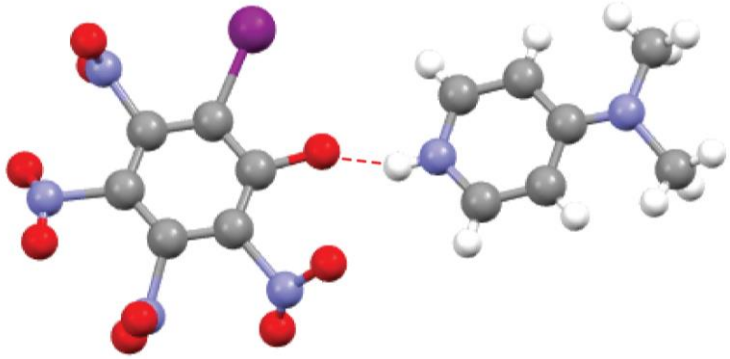
Upon execution of the cocrystallization conditions stated above for compound **5** with HMTA, 4,4'-BIPY, 4-PICO, and DMAP, single crystals were only obtained for compound **5** with 4-PICO and DMAP. The characterization of the single crystals via SC-XRD revealed decomposition products of both compound **5**/4-PICO and DMAP, in the form of salts (**Figures**

4.13 and **4.14**, respectively). The full crystallographic information of compound **5**/4-PICO and DMAP, which have some disorder, are shown in **Table 4.3**.



IPNB/4-PICO

Figure 4.13. Salt of compound **5**/4-PICO (one conformer shown).



IPNB/DMAP

Figure 4.14. Salt of compound **5**/DMAP (one conformer shown).

Table 4.3 Crystallographic data for compounds **5**/4-PICO and DMAP.

Structural Information	Compound 5/4-PICO (some disorder)	Compound 5/DMAP (some disorder)
Space Group	P 1	P 2_1/n
a (Å)	4.9385(5)	4.8413(5)
b (Å)	12.2143(11)	19.689(3)
c (Å)	14.0592(10)	19.8363(15)
α (°)	82.839(7)	90
β (°)	85.055(7)	94.41(1)
γ (°)	87.627(8)	90
Volume (Å^3)	87.627(8)	1885.2

Given that IPNB was reported to undergo decomposition during recrystallization and the experimental cocrystallizations attempted above resulted in salt formation, these suggest instability within IPNB when exposed to ambient conditions over extended periods of time; thus reaction conditions that would allow for rapid determination of halogen bond formation was required.

4.2.4 Halogen bonding in solution for IPNB

Previous studies have reported the use of Raman spectroscopy in the solution phase to investigate halogen bonding propensity in systems that contain six membered halogen bond donors and acceptors with a range of donor and acceptor strengths.[26] Therefore, Raman spectroscopy was utilized to determine changes in the C-I vibrational frequency (ν) of IPNB, shown in **Table 4.4**, with THF ($V_{s,min}$= -43.98 kcal mol^{-1}) denoted by a red shifted C-I peak which would signify complexation (iodine interaction with oxygen: C-I···O). The experimental setup for Raman spectroscopy in solution for IPNB is detailed in section **4.4.8** of the **Experimental Setup** section. **Figure 4.15** with the IPNB/THF mixture illustrates a successful complexation denoted by the

presence of the new red shifted C-I vibrational stretching frequency at = 200.5 cm^{-1} (**Table 4.4**), which is consistent with the strength of halogen bonding interactions formed between a strong halogen bond donor and a weak Lewis base

Table 4.4. C-I stretching vibrational frequency (ν) in cm^{-1} of unbound IPNB and the complex observed with THF in DCE.

XB donor and XB Complex	C-I Raman Shift (cm^{-1})
IPNB	209.5
IPNB/THF	200.5[a]
[a] Red shifted peaks of formed complex.	

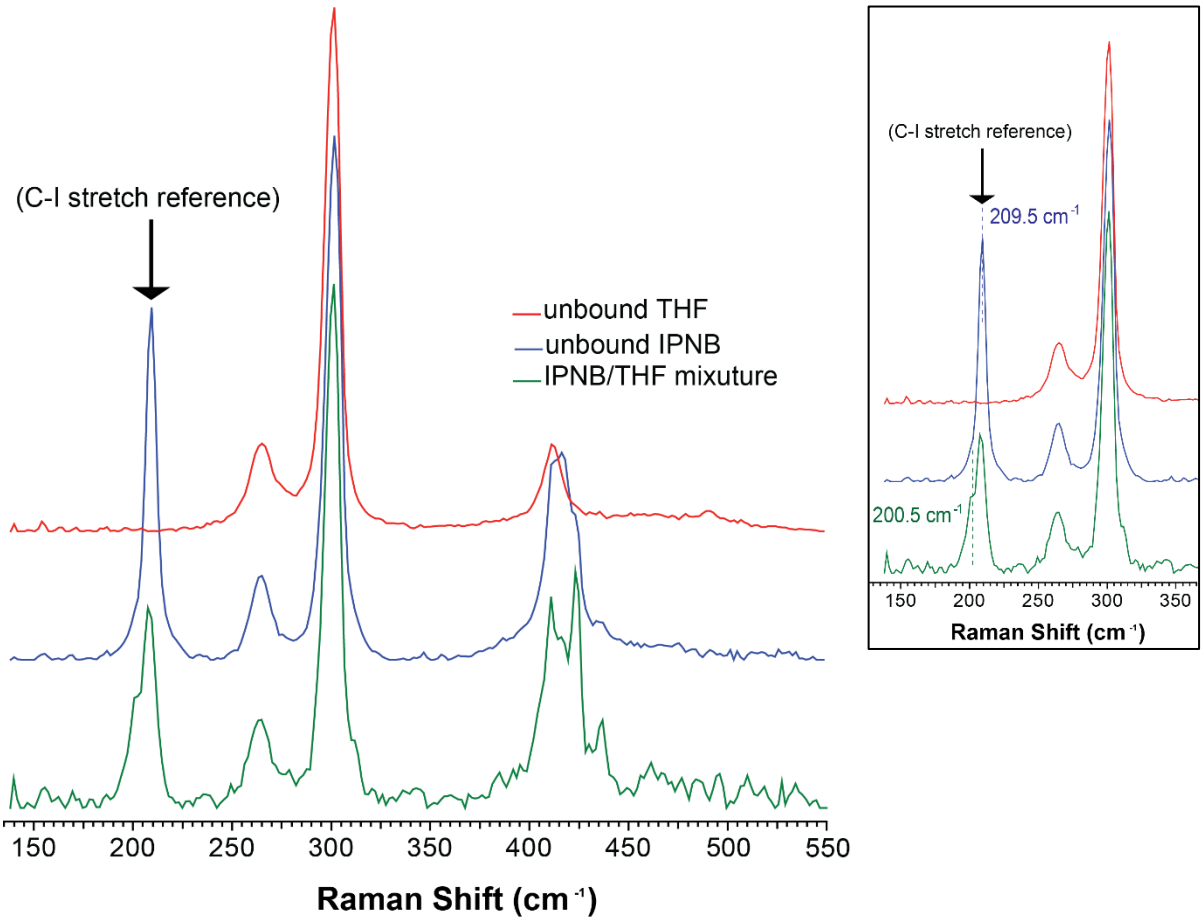


Figure 4.15. Stacked Raman spectra of unbound IPNB (blue), unbound THF (red), and IPNB/THF mixture (green)with zoomed in stacked Raman spectra in DCE.

4.3 Conclusion

The investigation of halogen bonded complexes formed from IPNB, a strong halogen bond donor, provided insight on the limitations of cocrystallization strategies that translate theoretical prediction models to the solid-state and solution phases. These limitations included understanding molecular stability and synthon compatibility under various reaction conditions and how they impact halogen bonding interactions. Moreover, four novel crystal structures were obtained for PNA, HNB, CPNB, and IPNB. Future work will examine the energetic performance properties of PNA, HNB, CPNB, and IPNB and their propensity to form new energetic materials via cocrystallization.

4.4 Methods

Caution! Hydrogen peroxide and fuming sulfuric acid (oleum) are strong oxidizers. Polynitrobenzene derivatives are explosive in nature. Proper safety practices, personal protective equipment, and blast shields were utilized to prevent personnel exposure or explosions. Be advised that health hazards due to exposure that may occur include eyes, nose, throat, and skin irritation (e.g., burns).

4.4.1 Materials and Reagents

3,5-Dinitrobenzene (TCI America, >98%), hexamethylenetetramine (ACS reagent, ≥99%), 4,4'-bipyridine (Combi Blocks, Inc, 98%), 4-picoline-*N*-oxide (Alfa Aesar/Johnson, 98%), 4-dimethylamino pyridine (Aldrich Chemical Co., ReagentPlus, ≥99%), sulfuric acid, extra pure, fuming, 20-30% free SO_3 (Acros Organics), 95-98% sulfuric acid (Thermo Fisher), 68-70% nitric acid, (Thermo Fisher), 36.5-38% hydrochloric acid (Thermo Fisher), 47-79% hydrobromic acid (Thermo Fisher), 47-51% hydroiodic acid (Thermo Fisher), and 98% H_2O_2 w/w in water

(Peroxychem) were used as received. Tetrahydrofuran (THF), methylene chloride (DCM), and 1,2-dichloroethylene (DCE) were obtained from Fisher Scientific and dried over 3Å molecular sieves.

4.4.2 General Methods: Reaction Conditions for IPNB Synthesis

*Synthesis of Pentanitroaniline **(2)** from 3,5-Dinitroaniline*. 3,5-Dinitroaniline (500 mg, (2.73 mmol)) was dissolved in 95-98% sulfuric acid (H_2SO_4, 23 mL) in a 100 mL round bottom flask at room temperature under nitrogen with stirring from a rare earth metal stir bar. The flask was cooled to between 0-10 ºC in an ice/water bath then 68-70% nitric acid (HNO_3, 1.25 mL) was added dropwise over 10 minutes with vigorous stirring. The flask was taken out of the ice/water bath and allowed to warm to room temperature then place in an oil bath for 1.5 hours at 70-74 ºC. After 1.5 hours, the reaction vessel was removed from the oil bath, cooled to room temperature, then place in an ice/water bath for 15 minutes. The dark orange precipitate in the reaction vessel was filtered from reaction vessel and washed with hexane then left to dry for 10 minutes on a glass fritted filter attached to a vacuum filtration apparatus. Crude PNA was recrystallized in boiling dry DCE, cooled to room temperature, then placed in -20 ºC freezer overnight. Yellow platy crystals of PNA were formed and characterized by Fourier transform infrared spectroscopy (FT-IR, **Figure 4.16**) and single crystal x-ray diffraction (SC-XRD, **Table 4.5**) of the **Additional Tables** section**.**

*Synthesis of Hexanitrobenzene (**3**) from Pentanitroaniline* (**2**). Pentanitroaniline (PNA) (59.4 mg, 0.187 mmol) was weighed in a tared 25 mL round bottom flask with a rare earth metal stir bar. 20-30% fuming sulfuric acid (3.0 mL) was added, and the solution was stirred at room temperature until solid had fully dissolved. The reaction vessel was cooled between 0-10 °C then 98% H_2O_2 (0.30 mL) was added slowly dropwise to the solution. The solution was protected from exposure to air by a connected nitrogen line. The reaction was allowed to stir vigorously for 3 days

then cooled between 0-10 °C in an ice/water bath for 15 minutes. Solid neon green crude precipitant was filtered across a glass fritted filter attached to a vacuum filtration apparatus and then collected into a 4 mL vial. Warm, dry chloroform was added dropwise to fully dissolve the solid then decanted away from residual acid layer and placed in a new 4 mL vial. The vial was allowed to cool to room temperature, sealed with parafilm, and placed in the dark for 1-2 days. Orange-yellow irregular shaped crystals (10.0 mg) were characterized by FT-IR (**Figure 4.16**), Raman spectroscopy (**Figure 4.17**), and SC-XRD (**Table 4.6**) of the **Additional Tables** section.

*Synthesis of Chloro-pentanitrobenzene (**4a**) from Hexanitrobenzene* (**3**). Hexanitrobenzene (10.0 mg, 0.0287 mmol) was dissolved in benzene (0.22 mL) at room temperature. 36.5-38% Hydrochloric acid (HCl, 0.44 mL) was added dropwise then reaction was allowed to stir vigorously for 30 minutes. After 30 minutes, additional benzene (0.50 mL) was added. The benzene layer was separated from purple acid layer using a glass pipette then run through an anhydrous $MgSO_4$ pipette column and collected into a 4 mL vial. The benzene layer was dried using a nitrogen stream and the remaining crude chloro-pentanitrobenzene (CPNB) was dissolved in boiling dry DCE then cooled to room temperature. CPNB (5.01 mg, 0.0148 mmol) was collected and characterized by SC-XRD (see **Table 4.7** of the **Additional Tables** section for crystallographic information).

*Synthesis of Iodo-pentanitrobenzene (**4b**) from Hexanitrobenzene* (**3**). Hexanitrobenzene (7.00 mg, 0.0201 mmol) was dissolved in benzene (0.30 mL) at room temperature. 47-51% Hydroiodic acid (HI, 0.60 mL) was added dropwise then reaction was allowed to stir vigorously for 6 minutes. After 6 minutes, additional benzene (0.20 mL) was added. The benzene layer was separated from purple acid layer using a glass pipette then run through a K_2CO_3 pipette column and collected into a 4 mL vial. The benzene layer was dried using a nitrogen stream and the remaining crude iodo-pentanitrobenzene (IPNB) was dissolved in boiling dry DCE then cooled to

room temperature in the dark. IPNB (1.73 mg, 0.0040 mmol) was collected and characterized by Raman spectroscopy (**Figure 4.17**) and SC-XRD (**Table 4.8**) of the **Additional Figures** and **Tables** sections.

4.4.3 General Methods: Cocrystallization Conditions for IPNB Complexes

*Attempted Cocrystallization of Iodo-pentanitrobenzene (**4b**) with Picoline-N-oxide.* IPNB (0.54 mg, 0.0022 mmol) and picoline-*N*-oxide (PICO, 0.25 mg, 0.0023 mmol) were dissolved in ethyl acetate (EtOAc, 150 µL each) in separate glass 4 mL vials with a polypropylene lid and PTFE gasket. IPNB solution was added to the PICO solution using a glass pipette. 4 mL vial was capped and sonicated for 10 minutes then 4 mL vial was uncapped and placed in a 20 mL vial containing 2.0 mL hexane. After 1-3 days crystals were found in the bottom of the 4 mL vial. Crystals were characterized by SC-XRD as a salt of the starting products (**Figure 4.13**).

*Cocrystallization of Iodo-pentanitrobenzene **(4b)** with 4-Dimethylaminopyridine.* IPNB (0.48 mg, 0.0019 mmol) and 4-dimethylaminopyridine (DMAP, 0.20 mg, 0.0016 mmol) were dissolved in ethyl acetate (EtOAc, 150 µL each) in separate glass 4 mL vials with a polypropylene lid and PTFE gasket. IPNB solution was added to the DMAP solution using a glass pipette. 4 mL vial was capped and sonicated for 10 minutes then the solvent was then 4 mL vial was uncapped and placed in a 20 mL vial containing 2.0 mL hexane. After 1-3 days crystals were found in the bottom of the 4 mL vial. Crystals were characterized by SC-XRD as a salt of the starting products (**Figure 4.14**).

4.4.4 Raman Spectroscopy

Raman spectra were collected using a Renishaw inVia Raman spectrophotometer featuring a Leica microscope, a 532 nm laser, 1800 lines/mm grating, a RenCam CCD detector,

and 50 μm slit size. Data collection was conducted with the WiRE 3.4 software package (Renishaw) and a silicon internal standard was used for calibration. Spectra for the XB solution experiments were collected in extended mode with a range of 100-1900 wavenumbers (cm^{-1}). The signal of the dissolved halogen bond donor C-I vibrational frequency shift (at ν =209.5 cm^{-1}) was used as a reference signal.

4.4.5 Fourier Transform Infrared Spectroscopy (FT-IR)

FT-IR spectra were obtained using a Thermo Scientific Nicolet iS50 FT-IR Spectrometer on a diamond ATR. The spectra were recorded from 300-3800 cm^{-1} with 32 scans taken.

4.4.6 Single-Crystal X-ray Diffraction (SC-XRD)

SC-XRD data were collected using a Rigaku XtaLAB Synergy-S X-ray diffractometer in a κ goniometer geometry configuration. The diffractometer was equipped with a low temperature device and a PhotonJet-S microfocus Cu source (λ = 1.54187 Å) operated at 50 kV and 1 mA. The X-ray intensities were measured at 100 K or room temperature with a HyPix-6000HE detector which was held 34.00 mm from the sample. The data were processed with CrysAlisPro v38.46 (Rigaku Oxford Diffraction) and were corrected for absorption. The structures were solved in OLEX2 using SHELXT and refined using SHELXL.

4.4.7 Differential Scanning Calorimetry

Thermograms of each sample were recorded on a TA Instruments Q10 DSC. All experiments were run using T-Zero pans at a heating rate of 10 °C/min which covered the temperature range of 25 °C to 400 °C. Calibration of the instrument was performed using an indium standard. Thermograms were analyzed using TA Universal Analysis 2000, V 4.5A. PNA (0.222 mg) and HNB (0.229 mg) samples were weighed prior to and after heating to ensure that no mass escaped from the pan during experimental analysis.

4.4.8 Experimental Setup

For Raman studies of halogen bonding in solution, a IPNB solution (1.00 mL, 0.0063 mol/kg in dry DCE) was prepared from the reaction of HNB (6.10 mg) in benzene (117.6 µL) with HI (235.2 µL) to yield IPNB (3.20 mg, 0.0075 mmol). 1:1 by volume (10 µL) IPNB solution/THF were added to a glass 2 mL glass screw vial with a 9 mm screw cap then placed on the stage of the Raman microscope and data collected using a 5× objective lens.

4.4.9 Computations

Density functional theory (DFT) and electrostatic potential maps (mapped on 0.002e/au electron density contour) were calculated at the B3LYP level of theory and 6-311G** basis set with Spartan'18 software (Wavefunction Inc., Irvine, CA). Starting geometrics were set to mimic halogen bonding interactions found in the CSD, where all interactions were built to interact at a ~180° bond angle for C-I···Y-R (i.e. Y= O or N and R= C, Ar, or EWG) interactions with energy minimization. The achievement of minimum energy geometry was confirmed by the absence of imaginary frequencies.

4.5 Additional Figures

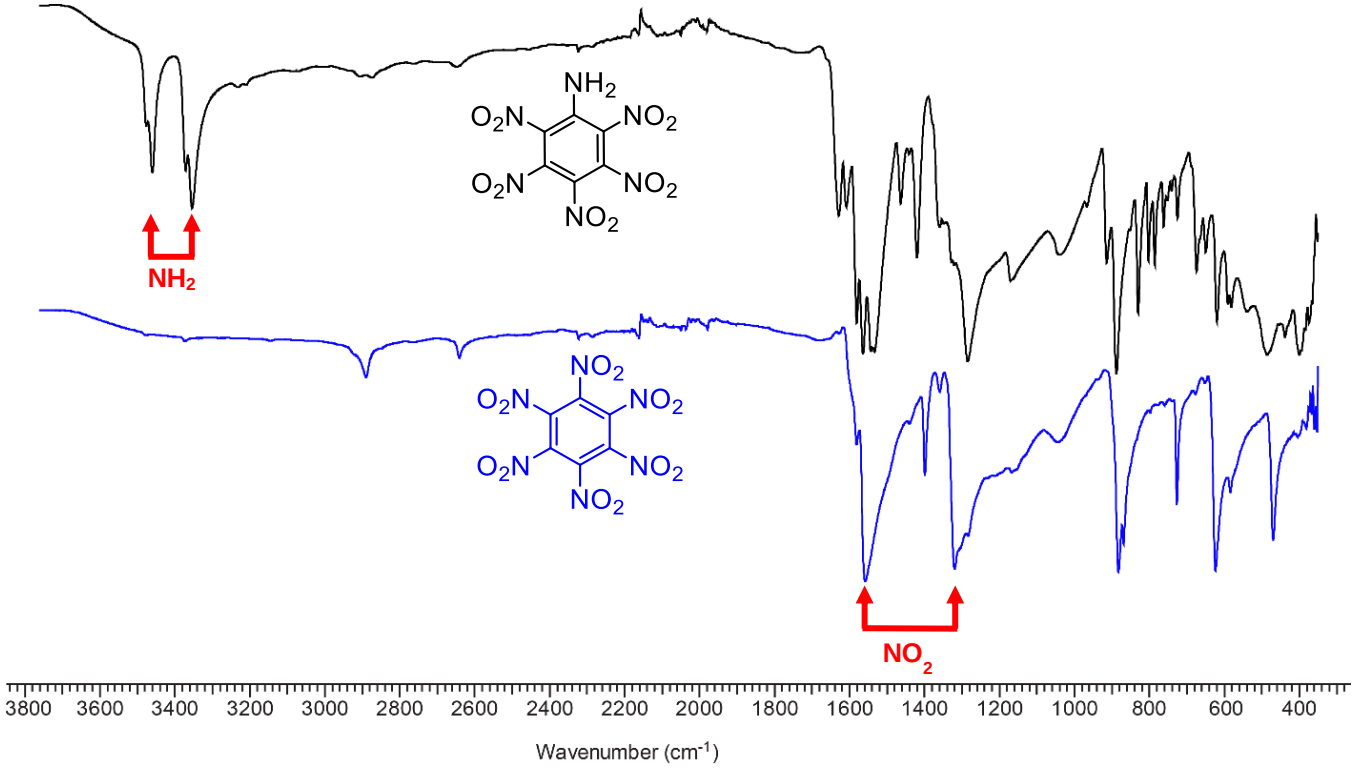


Figure 4.16. Stacked FT-IR spectra of compound **2** (PNA, black) and compound **3** (HNB, blue) with amine and nitro-group peaks highlighted with red arrows.

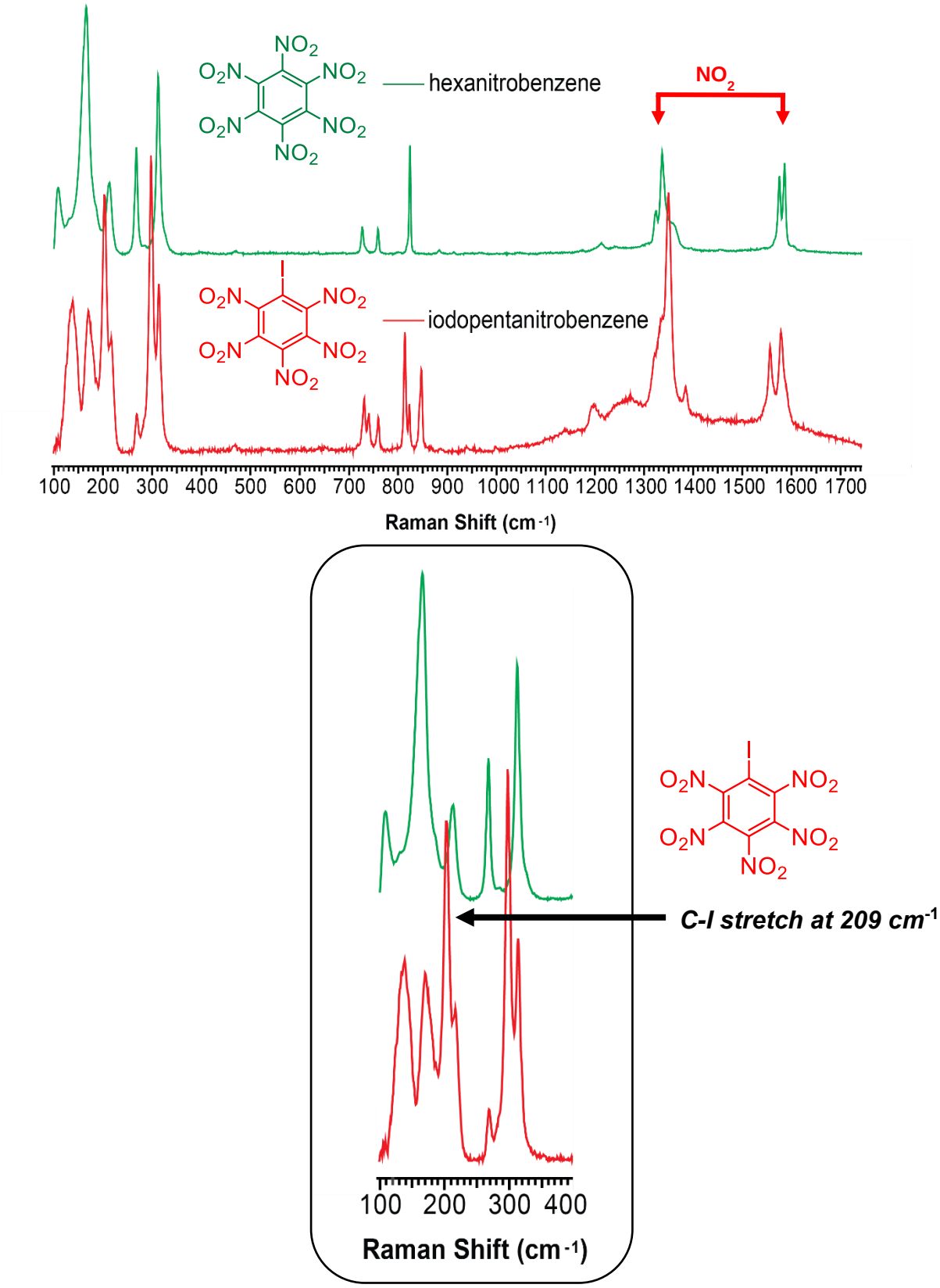


Figure 4.17. Stacked Raman spectra of HNB (green) and IPNB (red) with zoomed range (100-400 cm^{-1}) for observed C-I stretch of IPNB.

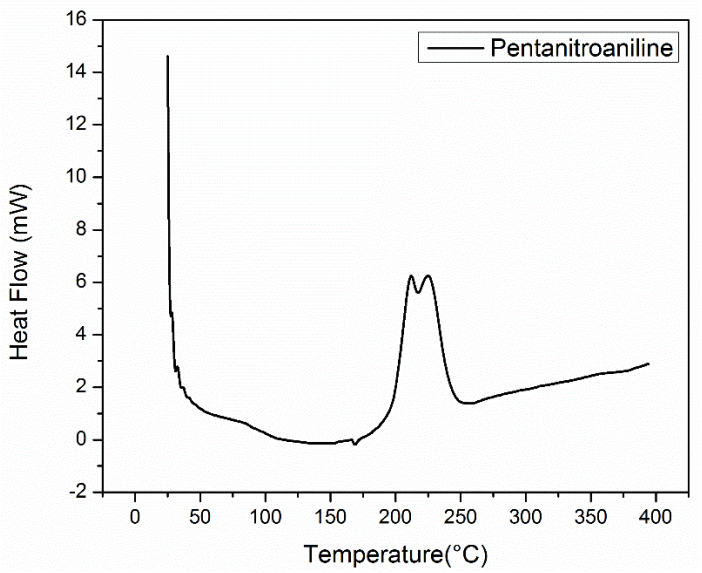


Figure 4.18. DSC trace of pentanitroaniline.

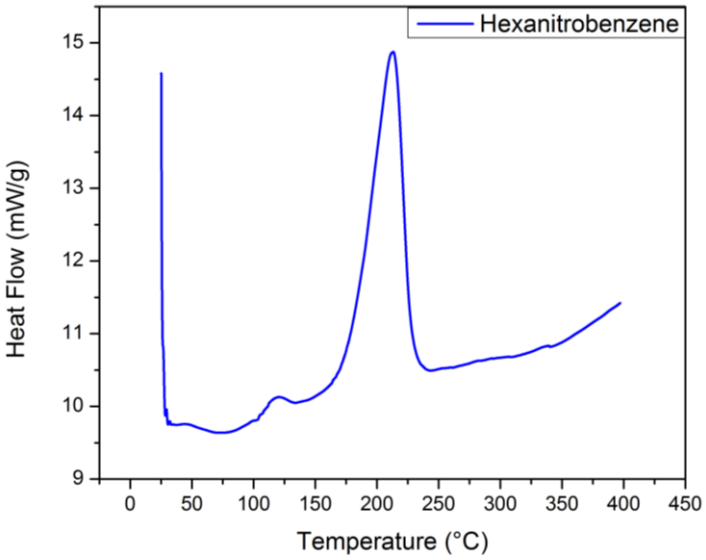


Figure 4.19. DSC trace of hexanitrobenzene.

4.6 Additional Tables

Table 4.5. Crystallographic data for pentanitroaniline (PNA).

Structural Information	**PNA**
Space Group	P 4 2_1 c
a (Å)	8.8543(2)
b (Å)	8.8543(2)
c (Å)	28.7145(14)
α (°)	90
β (°)	90
γ (°)	90
Volume ($Å^3$)	2251.18
Z	8
R-Factor(%)	3.28
Temperature (K)	RT
Density	1.871

Table 4.6. Crystallographic data for previously published and newly characterized hexanitrobenzene (HNB).

Structural Information	**HNOBEN (CSD)**	**HNB**	**HNB**
Space Group	*I*2/*c*	*C*2/*c*	*P3c1*
a (Å)	13.220(30)	15.5924(13)	8.9106(3)
b (Å)	9.130(40)	9.0173(9)	8.9106(3)
c (Å)	9.680(30)	24.524(2)	24.0791(8)
α (°)	90	90	90
β (°)	95.50(50)	89.995(7)	90
γ (°)	90	90	120
Volume ($Å^3$)	1162.984	3448.11	1655.71(8)
Z	4	8	6
R-Factor(%)	19.6	29.54	5.09
Temperature (K)	RT	297(1)	100.01(10)
Density	1.988	1.962	2.095

Table 4.7. Crystallographic data for previously published and newly characterized chloro-pentanitrobenzene (CPNB).

Structural Information	**WANMON (CSD)**	**CPNB**
Space Group	*P*-1	*P*-1
a (Å)	12.137(2)	5.6880(2)
b (Å)	12.181(2)	8.4224(2)
c (Å)	11.694(2)	12.8622(4)
α (°)	100.39(1)	104.980(2)
β (°)	100.10(1)	94.147(3)
γ (°)	78.02(1)	103.666(3)
Volume ($Å^3$)	1646.284	572.523
Z	6	2
R-Factor(%)	2.9	4.23
Temperature (K)	RT	297(1)
Density	1.915	1.958

Table 4.8. Crystallographic data for newly characterized iodo-pentanitrobenzene (IPNB).

Structural Information	**IPNB**
Space Group	*C*2/*c*
a (Å)	9.0052(6)
b (Å)	16.4709(15)
c (Å)	8.3527(7)
α (°)	90
β (°)	99.648(8)
γ (°)	90
Volume ($Å^3$)	1221.39
Z	15.38
R-Factor(%)	15.38 (some disorder)
Temperature (K)	297(5)
Density	2.399

4.7 References

[1] C. B. Aakeröy, C. L. Spartz, in *Halogen Bonding I* (Eds.: P. Metrangolo, G. Resnati), Springer International Publishing, Cham, **2014**, pp. 155–182.

[2] J. Lieffrig, O. Jeannin, A. Frąckowiak, I. Olejniczak, R. Świetlik, S. Dahaoui, E. Aubert, E. Espinosa, P. Auban-Senzier, M. Fourmigué, *Chem. Eur. J.* **2013**, *19*, 14804–14813.

[3] P. Metrangolo, F. Meyer, T. Pilati, G. Resnati, G. Terraneo, *Angew. Chem. Int. Ed.* **2008**, *47*, 6114–6127.

[4] P. Politzer, J. S. Murray, *ChemPhysChem.* **2013**, *14*, 278–294.

[5] P. Politzer, J. S. Murray, T. Clark, *Phys. Chem. Chem. Phys.* **2013**, *15*, 11178–11189.

[6] T. Clark, M. Hennemann, J. S. Murray, P. Politzer, *J. Mol. Model.* **2007**, *13*, 291–296.

[7] A. J. Stone, *J. Am. Chem. Soc.* **2013**, *135*, 7005–7009.

[8] G. Cavallo, P. Metrangolo, R. Milani, T. Pilati, A. Priimagi, G. Resnati, G. Terraneo, *Chem. Rev.* **2016**, *116*, 2478–2601.

[9] A. Mukherjee, S. Tothadi, G. R. Desiraju, *Acc. Chem. Res.* **2014**, *47*, 2514–2524.

[10] K. B. Landenberger, A. J. Matzger, *Cryst. Growth Des.* **2010**, *10*, 5341–5347.

[11] A. B. Đunović, D. Ž. Veljković, *CrystEngComm.* **2021**, *23*, 6915–6922.

[12] J. C. Bennion, L. Vogt, M. E. Tuckerman, A. J. Matzger, *Cryst. Growth Des.* **2016**, *16*, 4688–4693.

[13] N. R. Goud, O. Bolton, E. C. Burgess, A. J. Matzger, *Cryst. Growth Des.* **2016**, *16*, 1765–1771.

[14] C. A. Gunawardana, C. B. Aakeröy, *Chem. Commun.* **2018**, *54*, 14047–14060.

[15] C. B. Aakeröy, T. K. Wijethunga, J. Desper, *J. Mol. Struct.* **2014**, *1072*, 20–27.

[16] K. E. Riley, K.-A. Tran, *Faraday Discuss.* **2017**, *203*, 47–60.

[17] K. B. Landenberger, O. Bolton, A. J. Matzger, *J. Am. Chem. Soc.* **2015**, *137*, 5074–5079.

[18] R. L. Atkins, A. T. Nielsen, C. Bergens, W. S. Wilson, *J. Org. Chem.* **1984**, *49*, 503–507.

[19] A. T. Nielsen, A. P. Chafin, S. L. Christian, *J. Org. Chem.* **1984**, *49*, 4575–4580.

[20] A. T. Nielsen, R. L. Atkins, W. P. Norris, *J. Org. Chem.* **1979**, *44*, 1181–1182.

[21] S. V. Rosokha, J. J. Lu, S. M. Dibrov, J. K. Kochi, *Acta Crystallogr., Sect. C: Cryst. Struct Commun.* **2006**, *62*, o464–o466.

[22] C. R. Groom, I. J. Bruno, M. P. Lightfoot, S. C. Ward, *Acta Crystallogr., Sect. B: Struct. Sci. Cryst. Eng. Mater.* **2016**, *72*, 171–179.

[23] Z. A. Akopyan, Yu. T. Struchkov, V. G. Dashevskii, *J. Struct. Chem* **1967**, *7*, 385–392.

[24] J. Trotter, *Can. J. Chem.* **1961**, *39*, 1638–1644.

[25] F. Gerard, A. Hardy, A. Becuwe, *Acta Crystallogr., Sect. C: Cryst. Struct. Commun.* **1993**, *49*, 1215–1218.

[26] T. A. Bramlett, A. J. Matzger, *Chem. Eur. J.* **2021**, *27*, 15472–15478.

Chapter 5

Conclusion

5.1 Summary of Work

The work detailed in Chapters 2-4 describes the various methodologies utilized not only to understand and distinguish between the nature of hydrogen and halogen bonding interactions, but also predict them in the solid-state and in solution phase. As a collective, these chapters identify caveats in correlating theoretical models to experimental observations and provide counter analyses to critically evaluate the accuracy of the models.

Chapter 2 centers on the application of a database approach to determine suitable N-heterocyclic coformers for hydrogen peroxide, to form peroxosolvates, through examination of their crystalline hydrate forms. Previous studies on the formation of peroxosolvates from cyclic *N*-oxides provided the groundwork for utilizing this approach for pyridine derivatives, which were not well represented as hydrates and even more so peroxosolvates in CSD.[1] It was found that promising pyridyl peroxosolvate formers can be identified through stringent criteria applied to coformer selection using their hydrate equivalents in the CSD. Each hydrate equivalent selected had at least one major hydrogen bond donor (water) to N-pyridyl interaction (O-H···N) within the crystal lattice which was used to facilitate the formation of new peroxosolvates; the strength of hydrogen peroxide as a hydrogen bond donor compared to water is substantially greater and thus their structural similarities afforded direct correlation from hydrate to peroxosolvate formation. Additionally, of the eight new peroxosolvates (pyridyl or *N*-oxide) formed, the structurally

characterized peroxosolvates without disorder have hydrogen bonding interaction distances that are significantly shorter than their corresponding hydrates. The implications of a one-pot N-oxidation of pyridines, in the presence of highly concentrated hydrogen peroxide, could afford routes toward pre and post synthetic modifications of sp^2-hybridized N-heterocycles used in energetic materials and pharmaceutical agents. Kinetics studies on the formation of pyridyl peroxosolvates over *N*-oxide peroxosolvates could provide better understanding of the rates at which each transformation occurs, thus allowing conditions to be optimized to mitigate or encourage either pyridyl or *N*-oxide peroxosolvate formation. The effects of steric hindrance and delocalization of electron density on pyridine oxidation could also be addressed from kinetic studies using pyridyl-containing compounds with various extents of electronic activation (i.e. electron rich/poor and sterically hindered).

Chapter 3 examines the experimental observation of halogen bonding interactions in solution using Raman spectroscopy with interaction propensity predicted by computational modeling. Previous studies on halogen bonding interactions have reported utilizing electrostatic potential calculations to guide predictions of solid-state crystal formation,[2–4] though others have concluded that electrostatic properties alone do not provide a well-rounded view of factors impacting crystal lattice formation.[5] Challenges are presented when attempting to predict these interactions in the solid-state because they are often convoluted by other interactions (e.g. hydrogen bonding or π- π stacking) that contribute to the overall packing in the crystal lattice, thus the pure effect of the halogen bond is obscured. A straightforward way to mitigate the crystal packing forces that complicate the analysis of halogen bonding is by working in solution. From the solution studies in Chapter 3, it was determined that a purely electrostatic model applied to uncomplexed donors does not adequately describe the propensity of interactions in solution. The

quantitative assessment of how electrostatic properties, as measured by electrostatic potentials (ESPs),[6] connect with theoretical binding energies (ΔE_{bind})[7] for halogen bonding interactions, provided a hierarchy for the contributions to interaction energies (i.e. polarization, charge-transfer, dispersion, and electrostatics) that aid in complex formation; thus, a better understanding of how to design halogen bonded complexes was obtained. This work highlights how essential reliable prediction methods are to design strategies that seek to translate theoretical calculations of strongly bound complexes into tangible material.

Chapter 4 pertains to the formation of multicomponent crystals of highly activated halo polynitrobenzene derivatives facilitated by halogen bonding interactions. Literature precedence illustrated that the formation of energetic and non-energetic cocrystals of 1,3,5-trihalo-2,4,6-trinitrobenzene (TXTNB, where X=Cl, Br, or I) derivatives were enabled through major halogen bonding interactions.[8,9] From understanding how halogen bonding played a crucial role in the formation of TXTNB complexes, design strategies toward strongly bound complexes featuring a more strongly polarized halogen bond donor than the TXTNB series were developed. The development of cocrystallization strategies to support the formation of iodo-pentanitrobenzene (IPNB)/XB acceptor complexes emphasized the importance of understanding the impact stability and synthon compatibility have on halogen bonding interactions. Each newly characterized energetic presented in Chapter 4 could be further studied for their energetic performance properties and in the case of strongly polarized IPNB, it could be evaluated as a new biocidal energetic material. These results serve as a fundamental guide for translating computational models into experimental evaluations toward the design of novel halogenated energetic materials formed via cocrystallization.

5.2 References

[1] L. M. Foroughi, A. J. Matzger, *Cryst. Growth Des.* **2021**, *21*, 5873–5879.

[2] D. Musumeci, C. A. Hunter, R. Prohens, S. Scuderi, J. F. McCabe, *Chem. Sci.* **2011**, *2*, 883.

[3] J. S. Murray, P. Politzer, *WIREs Comput Mol Sci.* **2011**, *1*, 153–163.

[4] J. S. Murray, P. Politzer, *J. Mol. Struct: THEOCHEM.* **1998**, *425*, 107–114.

[5] A. Bauzá, D. Quiñonero, A. Frontera, P. M. Deyá, *Phys. Chem. Chem. Phys.* **2011**, *13*, 20371–20379.

[6] R. A. Wiscons, M. K. Bellas, J. C. Bennion, A. J. Matzger, *Cryst. Growth Des*. **2018**, *18*, 7701–7707.

[7] J. Yang, B. Hong, N. Wang, X. Li, X. Huang, Y. Bao, C. Xie, H. Hao, *CrystEngComm.* **2019**, *21*, 6374–6381.

[8] N. R. Goud, A. J. Matzger, *Cryst. Growth Des.* **2017**, *17*, 328–336.

[9] N. R. Goud, O. Bolton, E. C. Burgess, A. J. Matzger, *Cryst. Growth Des.* **2016**, *16*, 1765–1771.